Numerical Investigation of Turbulent Dispersion of Passive Scalars Emitting from Line Sources in Smooth and Rib-roughened Channels

by

Asghar Noormohammadi

A thesis submitted to
The Faculty of Graduate Studies of
The University of Manitoba
in partial fulfillment of the requirements
of the degree of

Doctor of Philosophy

Department of Mechanical Engineering
The University of Manitoba
Winnipeg, Manitoba, Canada
May 2022

Abstract

Turbulent dispersion of passive scalar released from line sources in a fully-developed smooth plane-channel and a rib-roughened open-channel are studied using direct numerical simulations (DNS). In order to investigate the effects of wall anisotropy on the plume development, the line sources are aligned either in the spanwise direction parallel to the wall or in the vertical direction perpendicular to the wall. The investigation into the turbulent transport processes of the momentum and concentration is conducted in both physical and spectral spaces, based on a systematic analysis of the statistical moments of the velocity and concentration fields, probability density functions (PDFs) of the scalar field, and the characteristic wavelengths of energetic eddies that dominate turbulent mixing processes. In the single vertical line source case, it was observed that the meandering ratio is small near the ground and within the turbulent diffusive stage, and PDFs of concentration fluctuations are sensitive to both the wall-normal distance and the downstream distance from the source. In the case of plume dispersion over a rib-roughened surface, it is observed that as the mean plume development enters the long-range dispersion stage, the decay rate of the mean concentration field begins to feature a constant slope of $-3/2$, while the vertical spread of the mean plume exhibits a constant slope of $1/3$. In the case of dual plume mixing, it is observed that a smaller source separation tends to facilitate a more rapid growth in the correlation coefficient of two instantaneous plumes. In the near-source regions, the maximum coherency spectrum is produced at lower frequencies indicating that dual-plume mixing is dominated by the external flapping effects of large-scale eddy motions. However, in the far downstream region of the sources, the coherency spectrum at higher frequencies increases significantly, indicating that the spread of the total plume is larger than all scales of turbulent eddies, such that they all contribute to the in-plume mixing of the dual plumes.

Acknowledgments

I want to express my gratitude to my advisor, Professor Bing-Chen Wang for his invaluable teaching and support. I want to express my appreciation to my committee members, Professor Karen Dow, and Professor Mark Tachie, for their encouragement and feedback.

Last but not the least, I would like to thank my parents, Omid-Ali Noormohammadi and Fatemeh Najafi for their unconditional love and supports.

Contents

List of Figures

Nomenclature

English Symbols:

A	area
c	instantaneous concentration
$Co_{c_1' c_2'}(f)$	co-spectrum of dual plumes
D	dosage of the concentration at an arbitrary wall-normal distance
$E_{\phi'\phi'}$	power spectra of a given quantity ϕ'
$\tilde{E}_{\phi'\phi'}$	temporal spectra of a given quantity ϕ'
f	frequency
f^*	Strouhal number (St): $f\delta/u_\tau$
h	height of a rib element
L_x	streamwise computational domain size
L_y	wall-normal computational domain size
L_z	spanwise computational domain size
k_x	wavenumber in the streamwise direction
k_z	wavenumber in the spanwise direction

P	pitch
p	pressure
p'	pressure correction
P_r	production rate of TKE
Q	mean scalar flux
r	the ration of upwind-side gradient to downwind-side gradient
Re_τ	Reynolds number based on wall friction velocity: $u_\tau \delta/\nu$
Re_c	Reynolds number based on mean centerline velocity: $\langle u_c \rangle \delta/\nu$
$R_{\phi'\phi'}$	spatial two-point correlation coefficients for a given quantity ϕ'
$\tilde{R}_{\phi'\phi'}$	auto correlation coefficients for a given quantity ϕ'
s	concentration strength
Sc	Schmidt number
Sc_T	turbulent Schmidt number
t	time
TV(ϕ)	total variation of a given quantity ϕ
T^+	time scale
u_i	velocity components, for $i = 1$, 2 and 3
u_τ	wall friction velocity
W	width of the rib element
u, v, w	instantaneous velocities in the x-, y-, and z-directions, respectively
x, y, z	streamwise, vertical and spanwise coordinates, respectively
y^+	wall coordinate
x_s, y_s	streamwise and vertical source positions
V	volume
z_c	instantaneous plume centroid dispersion
z_r	instantaneous relative plume dispersion

Greek Symbols:

δ	half channel height
δ_{ij}	Kronecker delta
Δx, Δy, Δz	grid resolutions in the x-, y- and z-directions, respectively
$\Delta_{\max}$	maximum grid size: $\max(\Delta x, \Delta y, \Delta z)$
$\nabla \cdot (\vec{\phi})$	divergence (div) of a given vector $\vec{\phi}$
$\nabla(\phi)$	gradient (grad) of a given quantity ϕ
∇^2	Laplace operator (Laplacian)
η	Kolmogorov length scale
ϵ	dissipation rate of TKE
λ_z	spanwise wavelength
σ_o	source size
σ_y, σ_z, σ_c, and σ_r	vertical and spanwise mean plume widths, plume centroid dispersion, and relative plume dispersion
$M = \sigma_c^2/\sigma_r^2$	meandering plume ratio
ν	kinematic viscosity
μ	dynamic viscosity
α	molecular diffusivity of the passive scalar
Π	mean streamwise pressure gradient
Σ_r	half width of an instantaneous relative plume
Σ_z	half width of the mean plume
ρ	density
ρ_{cc}	cross-correlation coefficient of dual plumes

ρ_{cs}	coherency spectrum of dual plumes
τ_w	wall shear stress
τ_η	Kolmogorov time scale
γ	factor coefficient for mass flux
χ	homogeneous direction
κ	slope of the universal log-law profile for the mean streamwise velocity $\langle u \rangle^+$
λ_B	Batchelor length scale
Ψ	limiter function for TVD
Υ	the temporal term in the momentum interpolation
ζ	similarity lateral coordinate
Ω	molecular diffusivity coefficient in the Reynolds transport theorem

Subscripts and Superscripts:

$(\cdot)_1$, $(\cdot)_2$, $(\cdot)_3$	streamwise, vertical, and spanwise components, respectively
$(\cdot)_c$	value at the centerline of the plane channel
$(\cdot)_s$	value at the source location
$(\cdot)'$	fluctuating component of a turbulence variable
$(\cdot)^+$	a quantity expressed in wall coordinate
$(\cdot)^m$	mode of a distribution
$(\cdot)_{rms}$	RMS values
$\lvert\cdot\rvert$	absolute value of a quantity
$(\cdot)_T$	value of the total plume
$\langle\cdot\rangle$	time- and spanwise-averaging for concentration, and time and plane-averaging for velocity
$\langle\cdot\rangle_{max}$	maximum value of an averaged quantity
$\langle\cdot\rangle_t$	time averaging
$\langle\cdot\rangle_s$	time- and spanwise-averaging
$(\cdot)_\infty$	far field value of a quantity

Abbreviations:

2-D	Two dimensional
3-D	Three dimensional
ADI	Alternating direction implicit method
CDF	Cumulative distribution function
CDS	Central differencing scheme
CFD	Computational fluid dynamics
CFL	Courant-Friedrichs-Lewy
CPU	Central processing unit
DNS	Direct numerical simulation
ES	Elevated source
FD	Finite difference
FE	Finite element
FFT	fast Fourier transformation
FVM	Finite volume method
GGDH	Generalized gradient-diffusion hypothesis
GS	Ground-level source
LES	Large-eddy simulation
LETOT	Large eddies turnover time
LS	Line source
LSOR	Line successive over-relaxation method
MDS	Molecular diffusive stage

MPI	Message passing interface
PDF	Probability density function
PLIF	Planar laser-induced fluorescence
PSOR	Point successive over-relaxation method
RMS	Root-mean-squares
RANS	Reynolds averaged Navier-Stokes
SPIV	Stereoscopic particle image velocimetry
TBL	Turbulent boundary layer
TKE	Turbulence kinetic energy
TSE	Turbulent scalar energy
TCS	Turbulent convective stage
TDS	Turbulent diffusive stage
TKE	Turbulence kinetic energy
TVD	Total variation diminishing
UD	Upwind differencing
ZPG	Zero pressure gradient

Chapter 1

Introduction

1.1 Motivation

The mixing of passive scalars emitting from a single or multiple sources in an anisotropic inhomogeneous turbulent flow is a challenging topic, which has a broad range of applications to such as pollution of hazardous materials in an urban environment and emission of thermal plumes in a turbulent boundary layer. Furthermore, turbulent convection and dispersion of a concentration plume released from a concentrated source over a smooth- or rough-wall surface have important applications to the studies of mass transfer in mechanical and chemical engineering, heat exchangers, and industrial wastewater pollution monitoring in rivers and lakes. Key factors that influence the turbulent mixing process of passive scalars include the source sizes, source configuration (e.g., horizontal, vertical), source separation, source elevation, wall condition (e.g., smooth- and rough- wall), background turbulence level, shear rate, Schmidt number, Reynolds number, the turbulence modes of both the velocity and scalar fields, Strouhal number, and growth of the plume envelope.

Numerical simulation allows in-detail investigation of the dispersive characteristics of passive scalars and the plume development within turbulent flows. With the advancement of parallel computing technology, direct numerical simulation (DNS) has

become an increasingly affordable tool for a detailed numerical study of turbulent mixing and scalar dispersion phenomena. In the following, previous achievements on experimental and numerical investigations into turbulent dispersion of passive concentration plumes are briefly reviewed, with an emphasis on the literature of numerical studies.

1.2 Previous Contributions

The dispersion of pollutants, including the mixing of single and multiple passive scalars in turbulent flows, has been the subject of a significant amount of experimental and computational effort over the past decades. In this regard, a number of researchers have studied the evolution of the single- and two-point sources interference of scalar fields in turbulent flows. Furthermore, research on the turbulent mixing processes of the single line- and two-line sources interference is especially instructive in turbulent boundary layers (TBLs). Significant efforts have led to a proper understating of the line source evolution in a shear flow. The most common geometries of interest are smooth-wall channel, and rib-roughened plane channel flows. In this review, the previous studies of dispersion phenomena are classified into the three main studies of single plume development, dual plumes interference, and the dispersion phenomena in the turbulent boundary layers over rough surfaces.

1.2.1 Single Plume Dispersion

Turbulent dispersion of a passive scalar emitting from a concentrated source is an important subject, which has important applications in environmental sciences and engineering. These applications include the dispersion of polluting materials in the atmospheric boundary layer (ABL), diffusion of thermal plumes under a weak heating condition in a TBL, and mixing of inert and flammable materials in a combustion process. Different from the scenario of thermal plume generation under an intense

heating condition, the buoyant effect is absent in the plume development of a passive scalar [3, 4]. The process of passive scalar dispersion depends primarily on the source configurations, background turbulence level, shear rate, Schmidt number, flow Reynolds number, and boundary conditions.

Turbulent dispersion of a passive scalar is governed by the convection-diffusion equation, and the physical process depends upon an excessive range of scales of turbulence [5, 6]. The continuous movements of scalar pockets reflect the convection mechanism, which is dominated by large-scale energy-containing eddy motions. Turbulent diffusion, however, is dominated by small-scale eddy motions [7, 8]. Taylor [9] derived explicit expressions for describing the diffusion process using a Lagrangian method. This theory was developed based on two characteristic scales of turbulence, i.e., the integral length scale of turbulence and the characteristic length scale of the most energetic eddies inferred from the spatial correlation of the velocity field. The study of the convective and diffusive stages of turbulent dispersion in the context of isotropic turbulence can be traced back to the classical works of Richardson [10], Warhaft [4], and Stapountzis *et al.* [8]. Richardson [10] reported that at a small distance from the origin of the concentrated thermal plume, the standard deviation of the scalar field forms a conical shape, which indicates that the plume spread is proportional to time. However, at a greater distance from the source, it forms a paraboloid shape, which reveals that the standard deviation of the scalar is a function of the square root of time. The regions featuring the conical and paraboloid shapes of the plume development correspond to the turbulent convective stage (TCS) and turbulent diffusive stage (TDS), respectively. Uberoi and Corrsin [11] investigated both turbulent and laminar passive heat diffusion generated by a hot wire. They reported that the streamwise development of the standard deviation of the laminar heat wake is parabolic. Stapountzis *et al.* [8] examined the diffusive process in great details and introduced the concept of the molecular diffusive stage (MDS). They reported that in the vicinity of the source, the plume spread is proportional to the square root

of time that was not matched to the result of Richardson [10]. This paradox was solved later by introducing the concept of MDS. As such, very close to the source, the dispersive characteristics cannot be represented by either a turbulent convective or a turbulent diffusive stage. Reviews on the subject have been systematically carried out by Warhaft [4], Karnik and Tavoularis [12], and Shraiman and Siggia [13].

The dispersion of a passive scalar is affected significantly by the characteristics of the background turbulence, which varies from being homogeneous isotropic to being wall-bounded and anisotropic. With the fast advancement of computer technology, DNS has also been applied to numerical studies of passive concentration dispersion in both wall-bounded flows and isotropic turbulence. The dispersion of scalar in homogeneous isotropic turbulence has been investigated analytically [14], using DNS [15], and based on wind-tunnel experiment [12]. Yeung [16] performed DNS and investigated the Lagrangian statistical properties of velocity and passive scalar fields. He showed that the scalar dissipation becomes de-correlated in time faster than does the turbulence kinetic energy (TKE) dissipation. Recently, Oskouie *et al.* [17] performed DNS to study the characteristics of a passive plume dispersing in isotropic turbulence. They compared the turbulence statistics of plumes released from single- and dual-line sources and showed that the large-scale eddy motions enhance not only the spread of the single plume but also the mixing of dual plumes.

In contrast to the study of turbulent dispersion of passive scalars in homogeneous isotropic turbulence as briefly reviewed above, this research focuses on turbulent line source dispersion in a plane channel, which features wall anisotropy. The phenomenon of turbulent dispersion in anisotropic turbulence is less understood because the plume development involves more degrees of complexity owing to the excessive range of scales of turbulence and the presence of the wall shear layer. According to the generalized gradient-diffusion hypothesis (GGDH) of Daly *et al.* [18], turbulent concentration fluxes are proportional to mean concentration gradients. Vanderwel and Tavoularis [19] conducted a water channel experiment to examine the GGDH theory. They

measured the turbulent dispersion of a passive scalar field emitting from a line source and evaluated all components of the eddy diffusivity tensor for the turbulent scalar fluxes.

In general, there are several distinctive dispersive characteristics associated with the turbulent dispersion of passive scalar in a wall-boundary flow. Firstly, the mean concentration field does not necessarily exhibit a Gaussian profile in the wall-normal direction as a direct result of wall anisotropy. In a wall-shear flow, the peak of the mean scalar field tends to drift towards the wall. Secondly, the symmetrical profile of the concentration variance (which features dual peaks, typical of a Gaussian plume in an isotropic and free-shear flow) is destroyed to reflect the wall condition. Thirdly, in isotropic turbulence, due to a lack of wall bounded flow, the characteristic length scale of the thermal plume may easily exceed that of the velocity field, and the transition from TCS to TDS occurs quickly. By contrast, in a turbulent channel flow, this is not the case because of the wall restriction on the plume development.

In their serial studies of passive heat transfer in a plane channel, Abe *et al.* [20] and Antonia *et al.* [21] conducted DNS for a relatively wide range of Reynolds numbers of $Re_\tau = 180$-1020. They investigated the correlations between the vorticity vector and the scalar derivative vector, the analogy between the turbulent transport processes of the momentum and passive scalar, and the influence of turbulent structures (such as near-wall streaks and vortical structures) on the scalar mixing process at various Reynolds numbers. In their studies, the passive scalar field is generated through a constant wall heat flux condition and the temperature field is statistically periodical in both streamwise and spanwise directions. It should be indicated here that the scenario of passive scalar dispersion released from an area source with streamwise and spanwise periodical boundary conditions [20, 21] is quite different from the scenario of a point or vertical line source release, as streamwise and spanwise homogeneity is absent in the concentration plume emitted from either a point or a vertical line source in a plane channel.

Noormohammadi and Wang [22] conducted a DNS study of a single horizontal (or, spanwise-aligned) line source dispersion in a turbulent smooth-wall plane-channel flow. They observed that the streamwise development of the plume is sensitive to both the source elevation and the downstream distance from the source. Later, Noormohammadi and Wang [23] performed DNS to investigate turbulent mixing of dual plumes emitting simultaneously from two horizontal line sources in a turbulent plane-channel flow. They studied turbulent dispersion and interference of two plumes in both physical and spectral spaces. They observed that a plume emitted from a ground-level horizontal line source transitions from TCS to TDS more rapidly than that released from an elevated horizontal line source. In Noormohammadi and Wang [22, 23], the line sources are aligned in the spanwise direction parallel to the wall in the context of a plane-channel flow. However, this geometrical setup of the line sources only allows for examination a number of fixed source elevations. In order to study turbulent dispersion of passive scalar under continuous variation of wall-anisotropy, Noormohammadi and Wang [24] further performed DNS to investigate into turbulent dispersion of concentration released from a vertical line source in a fully-developed plane-channel flow. To analyze the wall-anisotropic effects on the continuous variation of the plume meandering ratio and the transition of plume development from TCS to TDS, a detailed comparison of the spatial and temporal scales of the turbulent velocity and scalar fields has been made in both physical and spectral spaces. Furthermore, they observed that a self-similarity in the non-dimensionalized mean concentration profile when it was scaled with a lateral coordinate normalized by the half plume width in the context of a smooth-wall plane-channel flow.

1.2.2 Multiple Plume Dispersion and Mixing

The mixing of passive scalars emitting from multiple sources in an anisotropic inhomogeneous turbulent flow is a challenging topic, which has a broad range of applications in such as pollution of hazardous materials in an urban environment and emission of

thermal plumes in a turbulent boundary layer. Key factors that influence the turbulent mixing process of two passive scalars include the source sizes, source separation, source elevation, background turbulence level, shear rate, Schmidt number, Reynolds number, plume spread, and temporal and spatial scales of turbulent eddies.

The physical phenomena involved in scalar dispersion depends on whether the turbulent flow is homogeneous. The mixing of scalar in homogeneous isotropic turbulence has been investigated analytically [14] and experimentally [25, 26, 4]. Eswaran, and Pope [27] conducted DNS to study turbulent dispersion of passive scalars of varying initial integral length scales in homogeneous isotropic turbulence. Juneja and Pope [28] extended the DNS study of Eswaran, and Pope [27] by further investigating turbulent mixing of two passive scalar fields in homogeneous isotropic turbulence. They examined the evolution of the joint probability density function (JPDF) of the two passive scalar fields. Oskouie *et al.* [17] conducted DNS study of single and dual line source dispersion in homogeneous isotropic turbulence. They showed that the scatterplots of the normalized third- and fourth-order concentration moments against the normalized second-order concentration moment collapse onto a single curve, exhibiting a pattern of similarity and indicating that higher-order concentration moments of dual plumes can be determined effectively from their lower-order concentration moments. Furthermore, they showed that the relationships between the various higher-order normalized statistical moments of the concentration field for the total plume (of the dual plumes) can be modeled using a probability distribution function in the context of isotropic turbulence.

In contrast to the dispersion phenomena in homogeneous isotropic turbulence, the plume development in inhomogeneous anisotropic flow involves more degrees of complexity due to the existence of wall shear layers. Vanderwel and Tavoularis [19] studied turbulent diffusion of a passive plume released from a line source in a water tunnel and evaluated all components of the eddy diffusivity tensor for the scalar fluxes. Their measurements were conducted simultaneously using stereoscopic particle image

velocimetry (SPIV) for the flow and planar laser-induced fluorescence (PLIF) for the concentration. They reported that the eddy diffusivity tensor that has a strong effect on the mixing process is often off-diagonal, revealing that the mixing process of a passive scalar is anisotropic in a uniformly sheared flow. Comprehensive experimental studies of passive plume dispersing from line sources in a wall-shear layer have been conducted in a wind tunnel by Lavertu and Mydlarski [29], and in a fully-developed high-aspect-ratio turbulent air channel flow by Costa-Patry and Mydlarski [30]. They observed that there is a drift in the temperature variance of a passive thermal plume towards the centerline of the channel. Vrieling and Nieuwstadt [31] studied the plume dispersion released from a single line source and dual-plume interference released from two nearby line sources in the center of a plane channel using direct numerical simulations (DNS). They showed that the variance of the dual plumes cannot be obtained by directly adding together the variance of each individual plume and the discrepancy depends on the source separation and downstream distance from the two sources at a given Reynolds number. Furthermore, they proposed an analytical model for the mean concentration and concentration variance, which were proven to be in good agreement with their DNS results. Oskouie *et al.* [32, 33] performed DNS study of dual-plume interference emitting from two point sources in a turbulent channel. Their results show that the source separation has a significant impact on the mixing process of two plumes. Boppana *et al.* [34] conducted large-eddy simulation (LES) to study plume dispersion emitted from a horizontal line source in different shear layers of a channel. They observed a drift of the mean concentration peak towards the wall in the plume dispersion from an elevated source.

1.2.3 Turbulent Dispersion in a Rough-wall Boundary Layer

Turbulent convection and dispersion of a concentration plume released from a concentrated source over a smooth- or rough-wall surface have important applications to the studies of mass transfer in mechanical and chemical engineering, atmospheric pol-

lution prediction, and industrial wastewater pollution monitoring in rivers and lakes. The process of turbulent transport of concentration is dependent upon and characterized by the flow Reynolds number, Schmidt number, surface roughness, source size σ_0, source strength s, source position in a TBL, and boundary conditions of the flow and concentration fields. In the following, previous achievements on experimental and numerical investigations into turbulent dispersion of passive concentration plumes are briefly reviewed, with an emphasis on the literature of numerical studies.

Studies of turbulence dispersion of concentration plumes over a surface roughened with regular-shape obstacles (such as ribs, cubes, and pyramids, etc.) are fundamentally important in environmental sciences and engineering. Davidson *et al.* [35] investigated the dispersion of a neutrally buoyant concentration plume released upwind of an array of cubes. They observed that owing to the presence of the wall roughness, the vertical mixing of the concentration is enhanced, resulting in a remarkable increase in the mean vertical spread of the concentration plume. Macdonald *et al.* [36] conducted a water-channel experiment to study the dispersion of pollutant plumes released in regular arrays of cubes of varying plan area density. They reported that surface roughness elements not only influence the vertical dispersion of the plume σ_y, but also cause a change in the horizontal lateral spread of the scalar field σ_z. As such, the mean plume associated with the test case of denser cubes possesses a larger lateral spread σ_z. In addition, they indicated that the profile patterns of the non-dimensionalized mean concentration field were consistent among all cases (based on either a flat terrain or rough-walls of different cube densities) in the sense that they exhibited a similar Gaussian distribution. This fact was further corroborated by Yee, and Biltoft [37], who conducted a field experiment to study the plume dispersing through a regular array of 12×10 large rectangular-shape building obstacles on the U.S. Army Dugway Proving Ground, Utah.

Besides the laboratory and field experimental studies of environmental dispersion of concentration over smooth- and rough-wall surfaces briefly reviewed above, signif-

icant progresses have been made towards numerical studies based on the Reynolds-averaged Navier-Stokes (RANS) method, LES, and DNS.

Johnson and Hunter [38] performed a RANS simulation of pollutant dispersion in urban canyons using the k-ϵ model of Paterson and Apelt [39, 40]. They showed that the dispersion of pollutant is enhanced by flow circulations near the ground. To understand the effects of street canyons on the vertical dispersion of pollutants, Sini *et al.* [41] conducted a RANS study based on the standard k-ϵ model. Kim, and Baik [42] investigated thermal effects on the flow and pollutant dispersion in urban street canyons based a RANS approach. They suggested that the vertical dispersion of the concentration is dependent on the pitch to height ratio P/h of the canyons. Wang *et al.* [43] performed RANS to investigate the dispersion of a passive scalar released from an instantaneous point source in a mock urban environment. They performed their simulations using the explicit algebraic nonlinear model of Speziale [44] for evaluating the Reynolds stresses, and proposed a length-scale model for assessing the dissipation rate of the concentration variance. Besides the RANS approaches, LES studies have become more and more frequently seen in the literature. Walton *et al.* [45] and Walton, and Cheng [46] conducted LES to investigate turbulent pollution dispersion within an urban canopy. They compared their LES predictions against the field data, and examined their LES results in the context of an idealized urban canyon. Saeedi, and Wang [47] conducted LES to study the dispersion of a passive scalar released from a ground-level point source in a modelled urban atmospheric boundary layer. They studied turbulent flow over a matrix of wall-mounted cubic obstacles along with continuous release of a passive scalar from a ground-level point source, and compared their LES results against a set of comprehensive water-channel measurement data of Yee *et al.* [48].

1.3 Research Goals

Thus far, the number of detailed DNS studies of turbulent plume dispersion emitting from a line source in a wall-bounded flow is still quite limited in the literature. Specifically, the wall-anisotropic effect on the transition of the plume development from the turbulent convective stage to the turbulent diffusive stage is still not clear. In view of this, here I aim at conducting a systematic DNS study of a passive plume dispersing from a line source of different elevations, and propose a practical method to identify the transition of the plume development from the turbulent convective to the turbulent diffusive stages.

In general, the number of detailed DNS studies of dual-plume interference released from two line sources in a turbulent boundary layer is very limited in the literature. Furthermore, all existing DNS studies reviewed above have almost exclusively focused on plume interference released from two symmetrical point or line sources of the same elevation. In contrast to the previous studies, here I aim at conducting a systematic DNS study of the interference of two plumes emitting simultaneously from a ground-level line source (GS) and an elevated line source (ES). The non-symmetrical source elevation effect on the dual plume mixing and dispersion in a wall shear layer will be explored systematically.

Previous studies of the passive scalar dispersion in a wall-bounded flow focused either on point source emission or 2-D line sources aligned in the homogeneous spanwise (wall-parallel) direction. Thus far, the scenario of 3-D line source dispersion vertically going through a wall shear layer has not been studied in the literature. In view of this, in this research, we aim at exploring the 3-D passive scalar dispersion in a plane-channel flow emitting from a line source positioned in the wall-normal direction, which constitutes our first research objective. Although the geometrical setup of the test case is relatively simple, the underlying physics of turbulent dispersion of a vertical line source is complex. This is because the plume development and

statistics of the concentration field to be studied here are inhomogeneous and vary significantly in all three directions, a scenario that is qualitatively different from the previous 2-D case of turbulent dispersion emitting homogeneously from a horizontal line source in a plane channel [34; 23]. In the present test case, the plume dispersion is dominated by the wall shear in the near-wall region, but exhibits features similar to those in an isotropic turbulence environment in the channel center. Furthermore, the transition of plume development from TCS to TDS is not only influenced by the relative spanwise length scales of the flow and plume but also complicated by the wall-normal distance. As my second objective for this subtopic, I also aim at filling in the gap of the literature by studying the wall-anisotropic effect on the plume transition from TCS to TDS. The physics underlying the vertical line source dispersion in a wall-bounded flow studied here is indeed rich and complex, which is determined by turbulence eddies of different sizes of different wall shear layers. In order to understand the influence of the turbulent eddies on the dispersive characteristics of the scalar, it is important to calculate and compare the length scales of the turbulent velocity and concentration fields. To this purpose, the analyses will be conducted in both physical and spectral spaces.

The number of detailed DNS studies of turbulent dispersion of concentration plume released from a concentrated source in smooth wall bounded flows is still limited in the literature in general. Furthermore, a high-fidelity DNS study of line source dispersion in the context of a rough-wall flow is still lacking in the current literature. In view of this, in this research, I aim at performing a detailed DNS study of turbulent dispersion of a concentration plume emitting from a line source over a rib-roughened surface, which constitutes my first research objective for this subtopic. In the present study, the statistical moments of the concentration field are influenced by the rib elements mounted on the wall, a scenario that is conceptually different from the previous smooth-wall cases [22; 23]. The mechanism of plume development in a rib-roughened turbulent boundary layer flow is still unknown. As my second objec-

tive for this subtopic, I also aim at filling in the gap of the literature by studying the combined wall shear and rib element effects on the concentration plume development and its transition from TCS to TDS.

1.4 Outline

The remainder of this thesis is organized as follows:

In chapter 2, the governing equations, solution algorithm, and the discretization scheme are presented.

In chapter 3, turbulent dispersion of a passive plume emitting from a single elevated line source of different elevations in a plane channel flow has been studied using DNS. The content has been published in Noormohammadi and Wang [22].

In chapter 4, turbulent mixing of dual plumes emitting simultaneously from line sources in a turbulent channel flow has been studied using DNS. The content has been published in Noormohammadi and Wang [23].

In chapter 5, Turbulent dispersion of passive concentration released from a vertical line source in a fully-developed channel flow is studied DNS. The content has been published in Noormohammadi and Wang [24].

In chapter 6, turbulent dispersion of concentration plume emitting from a horizontal line source over a rib-roughened surface has been studied using DNS. The content has been submitted for publication in Noormohammadi and Wang [49].

In chapter 7, major conclusions of this thesis and the possible future work are summarized.

Finally, the numerical algorithm based on a finite volume method is presented in appendix A.

Chapter 2

Numerical Method

2.1 Governing Equations

In DNS, the transport processes of the momentum and concentration are governed by the following equations in the context of an incompressible flow:

$$\frac{\partial u_i}{\partial x_i} = 0 \quad , \tag{2.1}$$

$$\frac{\partial u_i}{\partial t} + u_j \frac{\partial u_i}{\partial x_j} = -\frac{1}{\rho}\frac{\partial p}{\partial x_i} + \nu \frac{\partial^2 u_i}{\partial x_j \partial x_j} - \frac{\Pi \delta_{1i}}{\rho} \quad , \tag{2.2}$$

$$\frac{\partial c}{\partial t} + u_j \frac{\partial c}{\partial x_j} = \alpha \frac{\partial^2 c}{\partial x_j \partial x_j} + s \quad , \tag{2.3}$$

where u_i represents the velocity, p is the pressure, ρ is the density of the fluid, Π is the mean streamwise pressure gradient that drives the flow, c denotes the concentration, s is the concentration source strength, and α represents the molecular diffusivity of the scalar. In the above equations, x_i represents the coordinate of the i-th direction, with $i = 1$, 2 and 3. These three directions are also referred to as the streamwise (x), vertical (y), and spanwise (z) directions, respectively. Correspondingly, the three velocity components, u_1, u_2 and u_3 are also denoted as u, v and w, respectively.

2.2 General Description of the Solution Algorithm

The DNS was conducted with an in-house computer code developed using the FORTRAN 90/95 programming language and parallelized following the message passing interface (MPI) standard. The numerical algorithm is based on a finite-volume method, and a second-order accuracy is achieved with respect to both spatial and temporal discretizations. For the momentum equation, a second-order central differencing scheme was used for the spatial discretization of both the convection and viscous terms. The second-order Runge-Kutta scheme was utilized for time integration. The pressure correction equation at each time step was solved using a multigrid method. The advection-diffusion equation that governs the transport of the passive scalar was implemented after the solution of the momentum equations at each time step. For the concentration field, due to a sharp gradient at the plume edge, the use of a central differencing scheme may result in spurious oscillations, which can further lead to unphysical negative concentration values. On the other hand, although a low-order up-winding scheme is effective in eliminating spurious oscillations, it may result in unacceptable false diffusion. This challenge involved in capturing the passive scalar interface is analogous to that in capturing a shock wave in a numerical simulation. In order to simulate regions with sharp concentration gradients, a second-order accurate total variation diminishing (TVD) scheme of Van Albada [50] was used for discretizing the convention term of the scalar transport equation.

The computer code used for conducting this research was developed collectively by the research group over the past several years, and have been successfully used for conducting LES of V-shaped ribbedd duct flow Fang *et al.*[51], and DNS of turbulent heat and fluid flows in smooth and rib-roughend duct of different rib alignments (transverse, V-shaped or inclined) Mahmoodi and Wang [52; 53; 54]. My contribution is to further develop the computer code for solving passive scalar dispersion problems. Major modifications of the computer code include proper setting up the boundary

conditions for the flow and concentration fields, and implementing a TVD scheme for discretizing the convection term.

All the simulations were conducted using a local 252-core server. The simulations were executed until statistically stationary conditions were attained for both velocity and concentration fields, after which various concentration statistics were collected over an extended time period of $50\delta/u_\tau$. For each simulated case, approximately 216,000 CPU hours were spent on solving the velocity and concentration fields, and for collecting turbulence statistics. A detailed description of the numerical algorithm is presented in appendix A.

Chapter 3

DNS Study of Plume Emission from an Elevated Line Source in a Wall-Bounded Flow

3.1 Abstract

Turbulent dispersion of a passive plume emitting from a single elevated line source of different elevations in a plane channel flow has been studied using direct numerical simulation (DNS).

The investigation was conducted in both physical and spectral spaces, which includes an analysis of statistical moments and pre-multiplied spectra of the velocity and concentration fields. It is observed that due to the presence of wall shear, the mean plume drifts towards the wall for the near-wall source release case. It is also observed that streamwise development of the plume is sensitive to both the source elevation and the downstream distance from the source.

The pre-multiplied power spectra of the velocity and concentration fields are compared in order to identify the transition of the plume development from the turbulent convective stage to the turbulent diffusive stage. For the line source placed near the

center of the channel, the plume development is dominated by the bulk meandering effects. However, for the plume emitting from the near-wall line source, it hits the ground soon after its release and becomes dominated by the wall shear. As the downstream distance from the line source increases, the streamwise development of the plume released from the near-wall line source transitions from a turbulent convective stage to a turbulent diffusive stage.

3.2 Problem Description

We study turbulent dispersion of a plume released from a line source positioned at the inlet of a plane channel. Figure 3.1 shows a schematic of the computational domain, line source, and coordinate system. The computational domain extends $4\pi\delta \times 2\delta \times 4\pi\delta/3$, in the streamwise ($x$), vertical ($y$) and spanwise ($z$) directions, respectively, where δ is the half channel height. The focus of this research is on the turbulent dispersion of a passive scalar, and the Reynolds number for the flow is kept at $Re_\tau = u_\tau \delta/\nu = 180$, where u_τ is the friction velocity, and ν is the kinematic viscosity of the fluid. In this study, the Schmidt number is kept at $Sc = 0.7$, a value that is typical for passive thermal energy diffusion in air and many gas flows. Two test cases of different source elevations are compared. In test case 1, the line source (LS1) is positioned at a relatively low elevation close to the wall with $y_s^+ = y_s u_\tau/\nu = 24$, while in test case 2, the line source (LS2) is positioned at a relatively high elevation near the channel center with $y_s^+ = 168$.

For the velocity field, periodical boundary conditions were applied to both streamwise and spanwise directions. No-slip and no-penetration conditions were enforced at the walls. For the concentration field, the zero-Neumann boundary condition was imposed on the wall and over the outlet plane. At the source position, the boundary condition for the concentration field was $c(x, y, z, t) \equiv c_s$ if $y = y_s$, where c_s is the constant concentration value of the line source. In DNS of turbulent mixing, very

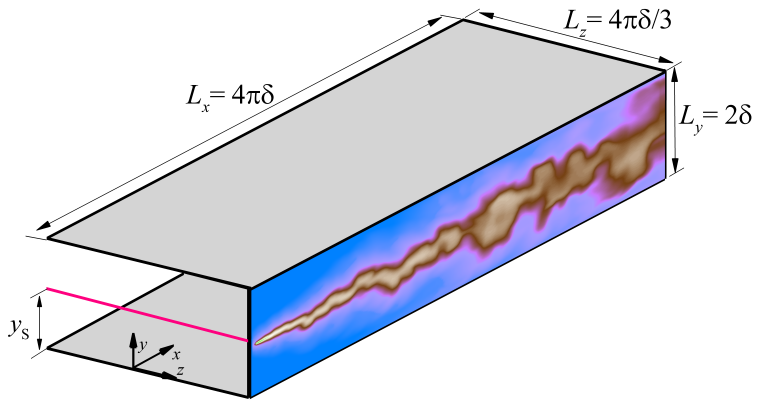

Figure 3.1: Schematic of the computational domain and an elevated line source, positioned in the inlet plane (at $x/\delta = 0$). Two test cases of different source elevations are compared. The line source (LS1) of case 1 is positioned at a relatively low elevation of $y_s^+ = 24$, while the line source (LS2) of case 2 is positioned at a relatively high elevation of $y_s^+ = 168$.

fine grid resolutions are required to resolve the Kolmogorov microscale, the smallest length scale of turbulent motions. To ensure the grid resolution required by DNS, $256 \times 192 \times 256$ grid points were used in x-, y- and z- directions, respectively. The grid resolution was uniform in the streamwise and spanwise direction with $\Delta x^+ = 8.84$ and $\Delta z^+ = 2.95$, respectively. The mesh was refined close to the wall. The wall-normal grid resolution varied from $\Delta y^+ = 0.2$ in the vicinity of the wall to $\Delta y^+ = 2.51$ at the channel center.

3.3 Result Analysis

In this section, the DNS data of the two test cases are analyzed in both physical and spectral spaces. This includes a study of the first- and second-order statistical moments of the velocity and concentration fields, pre-multiplied spectra of the concentration fluctuations, and budget balance of the transport equation of the mean concentration.

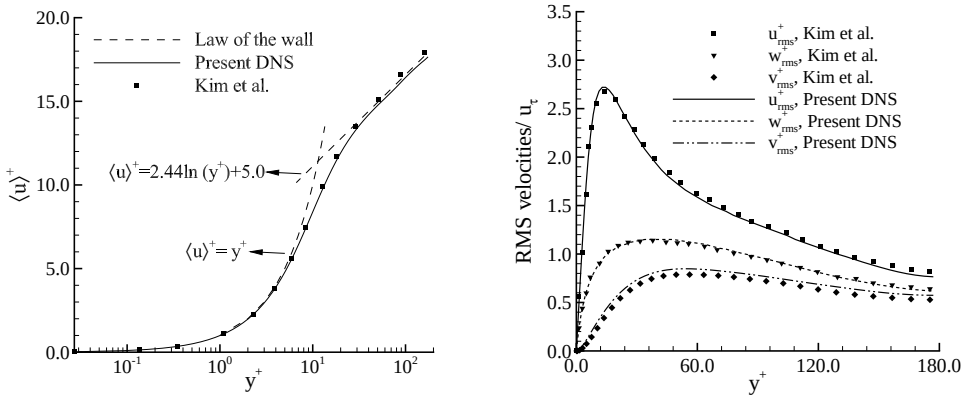

(a) Mean Streamwise velocity (b) RMS velocities

Figure 3.2: Mean and RMS velocities in comparison with the conventional law-of-the-wall and DNS data of Kim *et al.* [1].

3.3.1 Velocity Field

The focus of this research is on passive plume. However, because the dispersion of a passive plume is significantly influenced by the flow advection, it is necessary to briefly examine the velocity field prior to any detailed analysis of the concentration field. Figure 3.2(a) compares the obtained mean streamwise velocity profile against the conventional law-of-the-wall for a zero-pressure-gradient boundary-layer based on the two-layer model of von Kármán. As shown in the figure, a good agreement is obtained, and the mean streamwise velocity profile is typical for a wall shear flow. Figure 3.2(b) compares the three components of the non-dimensionalized root-mean-square (RMS) velocities (i.e., u^+_{rms}, v^+_{rms} and w^+_{rms}) against the DNS data of Kim *et al.* [1]. Clearly, the agreement between the current and previously reported DNS data sets is excellent, and the effects of wall anisotropy on the three RMS velocities is evident. All velocity statistics shown in Fig. 3.2 have been non-dimensionalized using the wall friction velocity u_τ, and all quantities shown with respect to the wall coordinate are denoted using superscript "+".

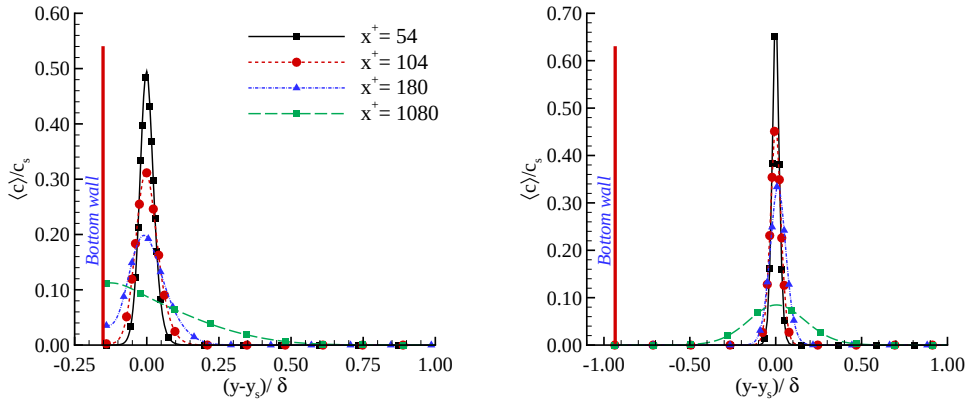

(a) LS1 (b) LS2

Figure 3.3: Vertical profiles of the mean concentration released from LS1 and LS2 at four locations downstream of the line source.

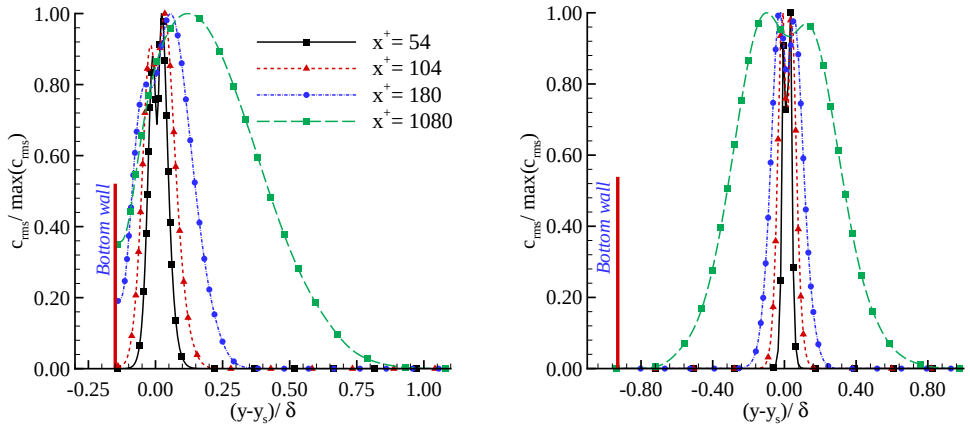

(a) LS1 (b) LS2

Figure 3.4: Vertical profiles of RMS concentration for plumes released from LS1 and LS2.

3.3.2 Concentration Statistics

Figure 3.3 compares the vertical profiles of the mean concentration released from two line sources (LS1 and LS2) at different streamwise locations. As shown in Fig. 3.3(a), the mean concentration profile associated with LS1 shows a quasi-Gaussian shape in the near-source region at $x^+ = 54$, and then gradually drifts towards the wall as the downstream distance from the line source increases. Eventually, at the far

downstream location $x^+ = 1080$, the profile shows a half-Gaussian shape typical of a ground-level plume. This drift of the mean concentration peak towards the wall is also seen in a plume emitting from a line source in a fully-turbulent channel flow in the LES study of Boppana *et al.* [34]. The wall-normal position of LS1 is very close to the wall with $y_s^+ = 24$. As such, the plume hits the ground soon after it is released from the line source, and then behaves as if it is emitted from a ground-level source. In contrast to LS1, LS2 is positioned at much higher elevation (for $y_s^+ = 168$) very close to the channel center ($y^+ = 180$). Therefore, the plume released from LS2 is expected to be insensitive to wall anisotropy. As shown in Fig. 3.3(b), the mean concentration field dispersing from LS2 exhibits a full Gaussian profile, which peaks at the source elevation at all four downstream locations as x^+ varies from 54 to 1080.

Figure 3.4 compares the RMS concentration profiles of the plumes emitting from LS1 and LS2. The value of the RMS concentration c_{rms} has been normalized by its local maximum value $\max(c_{rms})$ of the wall-normal direction. As shown in Fig. 3.4(b), for the plume released from LS2, a dual-peak pattern is evident at all four downstream locations both close to and far away from the source (with x^+ varying from 54 to 1080). Because the plume width expands in the vertical direction as it develops streamwise, the vertical spread of c_{rms} increases as the downstream distance from LS2 increases from $x^+ = 54$ to 1080. As is well understood, an ideal Gaussian mean concentration profile in a free-shear flow induces two infection points, which result in the maximum production rate for the concentration variance and lead to a dual-peak pattern in RMS concentration profile. Because LS2 is positioned very close to the channel center, the dual-peak pattern in the RMS concentration profile is almost symmetrical, a pattern that is evident at all four streamwise locations in Fig. 3.4(b). However, as shown in Fig. 3.4(a), for the plume released from the near-wall source LS1, the profile of c_{rms} shows a dual-peak pattern characteristic of a Gaussian plume distribution only at the near-source locations of $x^+ = 54$ and 104. Because line source LS1 is positioned very close to the wall, the wall shear has a strong effect on the profile

of c_{rms}, and its dual peaks are not symmetrical in the vertical direction (with respect to $(y - y_s)/\delta$) in regions far downstream of the line source. From Fig. 3.4(a), it is clear that as the streamwise distance x^+ from LS1 further increases to 180, the dual-peak pattern almost disappears under an increasingly stronger wall effect. From our previous analysis of Fig. 3.3, it is understood that in the far downstream region of LS1 at $x^+ = 1080$, the mean concentration exhibits only one half the Gaussian profile characteristic of a ground-level plume. Correspondingly, as shown in Fig. 3.4(a), the vertical spread of c_{rms} has transitioned to a single-peak pattern at $x^+ = 1080$.

3.3.3 Spectral Analysis

Although the grid resolution of DNS is the highest in all computational fluid dynamics (CFD) methods, it is still impossible to study the molecular diffusion process occurring at a scale that is smaller than Kolmogorov scale using DNS. In the current DNS study of the streamwise development of an instantaneous plume released from a line source, there are two distinct scalar dispersion stages, i.e., the turbulent convective and diffusive stages [14; 32]. In the turbulent convective stage, the scale of the instantaneous plume is typically larger than the Kolmogorov microscale but smaller than that of the most energetic eddies. The large-scale energetic eddies may carry concentration patches around through "flapping" motions, contributing to the so-called external mixing of the concentration and bulk meandering of the plume. In the turbulent diffusive stage, however, the scale of the instantaneous plume becomes larger than that of the most energetic eddies. As such, the energetic eddies contribute to the inner mixing of the concentration field associated with the in-plume mixing processes.

In the literature, there have been discussions related to the transition of the plume development from a turbulent convective to a turbulent diffusive stage [14; 32; 33; 17]. However, thus far, the discussions have been restricted to the streamwise development of the lateral plume spread in the homogeneous direction of the flow. In our current

study of turbulent plume dispersion in a wall-bounded flow, the situation becomes very complicated. Very close to the wall, concentration fluctuations are primarily contributed by inner mixing. This is because the flow is dominated by viscous forces, and the length scales of eddies are relatively small in the near-wall region. As such, the plume size is typically larger than the local eddy sizes, and local eddy motions contribute to in-plume mixing and fluctuations. However, in the center of the channel (especially in regions immediately downstream of the source where the plume spread is much smaller than the scale of energetic eddies), the flow is dominated by large-scale eddy motions. The large-eddy turbulent eddies create external flapping effects and facilitate the meandering and external mixing of the plume. Furthermore, in the present investigation of a plume development released from a line source, there is a new challenge to study this transition phenomenon. This is because the plume emitting from a line source is homogeneous in the spanwise direction, and therefore, the plume development is two-dimensional (2-D) statistically. In theory, the mean plume width is infinite in the spanwise direction, as indicated by the spanwise periodical boundary condition of the concentration field. In view of this, it is clear that a new approach is needed in order to define a characteristic length scale associated with the spanwise plume development emitting from a line source. To this purpose, we perform spectral analysis. Given the spanwise homogeneity in the velocity and concentration fields, the energy spectra of the fluctuating velocity and scalar fields are defined as:

$$E_{w'w'}(k_z) = \frac{1}{\pi}\int_{-\infty}^{+\infty} e^{-ik_z r} R_{w'w'}(r)dr \quad , \tag{3.1}$$

and

$$E_{c'c'}(k_z) = \frac{1}{\pi}\int_{-\infty}^{+\infty} e^{-ik_z r} R_{c'c'}(r)dr \quad . \tag{3.2}$$

Here, $R_{w'w'}(r) = \langle w'(z)w'(z+r)\rangle / w_{rms}^2$ and $R_{c'c'}(r) = \langle c'(z)c'(z+r)\rangle / c_{rms}^2$ are spanwise correlation functions of the velocity and concentration fluctuations, respectively. For the pre-multiplied spectra ($k_z E_{w'w'}$ and $k_z E_{c'c'}$) of the fluctuating velocity and concentration fields, their modes ($\lambda_{z,w'}^m$ and $\lambda_{z,c'}^m$) correspond to the characteristic

length scales of the most energetic eddy motions responsible for turbulent mixing of the momentum and concentration, respectively. Here, $\lambda_z \equiv 2\pi/k_z$ is the spanwise wavelength, k_z represents the spanwise wavenumber, and superscript 'm' is used to indicate 'mode'. Because the velocity field is homogeneous over a x-z plane, the characteristic length scale of large energetic eddy motions as indicated by the mode of $k_z E_{w'w'}$ has a fixed value at a given wall-normal position. In other words, it is a function of y^+ only, i.e. $\lambda^{m+}_{z,w'} = \lambda^{m+}_{z,w'}(y^+)$. In contrast, for the plume development, it is homogeneous in the spanwise direction and but is spatially developing in the streamwise direction. As a result, the characteristic length scale of the fluctuating plume varies with not only y^+ but also the downstream distance x^+ from the line source, i.e. $\lambda^{m+}_{z,c'} = \lambda^{m+}_{z,c'}(x^+, y^+)$. For a 2-D plume released from a line source, the transition from the turbulent convective stage to the turbulent diffusive stage can be determined by comparing the modes of the pre-multiplied spectra of the velocity and concentration fields. Specifically, at a given wall-normal position y^+, the dispersion is considered to be at a turbulent convective stage if $\lambda^{m+}_{z,w'} > \lambda^{m+}_{z,c'}$, but at a turbulent diffusive state if $\lambda^{m+}_{z,w'} < \lambda^{m+}_{z,c'}$. In other words, for a plume dispersing from a line source, in the turbulent convective stage, the characteristic length scale of energetic eddy motions ($\lambda^{m+}_{z,w'}$) is larger than that of the plume ($\lambda^{m+}_{z,c'}$), and in consequence, the plume development is dominated by the meandering effect. However, in the turbulent diffusive stage, the characteristic length scale of energetic eddy motions ($\lambda^{m+}_{z,w'}$) is smaller than that of the plume ($\lambda^{m+}_{z,c'}$), and in consequence, the in-plume mixing mechanism dominates the turbulent dispersion process of the scalar.

Figures 3.5 and 3.6 compare the pre-multiplied spectra of the velocity and concentration fields for instantaneous plumes released from LS1 and LS2. The pre-multiplied spectra of both the velocity and concentration are calculated at an elevation corresponding to the peak of the mean concentration at each downstream location of the instantaneous plume. As shown in Fig. 3.5(a)-(b), for the plume released from LS1, the characteristic length scale inferred from the mode of the pre-multiplied spectrum

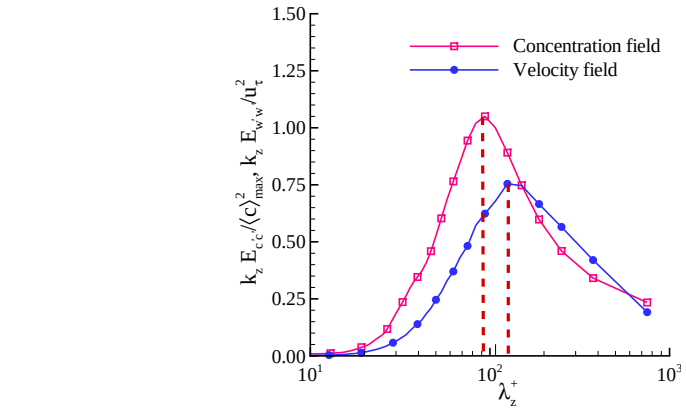

(a) $x/\delta = 2$, $y^+ = 21$

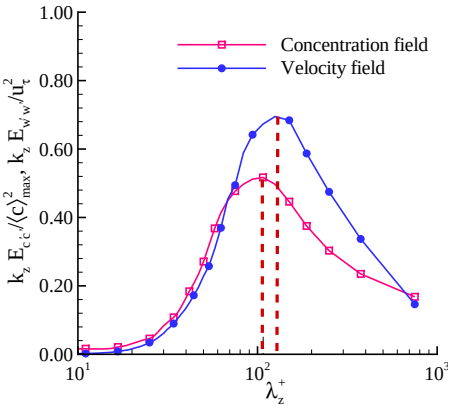

(b) $x/\delta = 3$, $y^+ = 15$

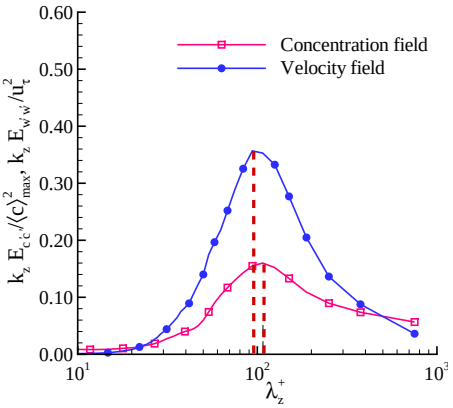

(c) $x/\delta = 3.5$, $y^+ = 4.5$

Figure 3.5: Comparison of the pre-multiplied spectra of velocity and concentration fluctuations at the elevation corresponding to the peak of the mean concentration at each downstream location for the plume released from LS1.

of the concentration is smaller than that of the velocity at $x/\delta = 2$ and 3, revealing that the plume development is in the turbulent convective stage, and the bulk meandering dominates the plume dispersion process in the form of external mixing. However, at $x/\delta = 3.5$, the characteristic length scale inferred from the mode of the pre-multiplied spectrum of the concentration becomes larger than that of the velocity, indicating that a transition in the plume development from the turbulent convective stage to the turbulent diffusive stage has occurred (shortly before this streamwise

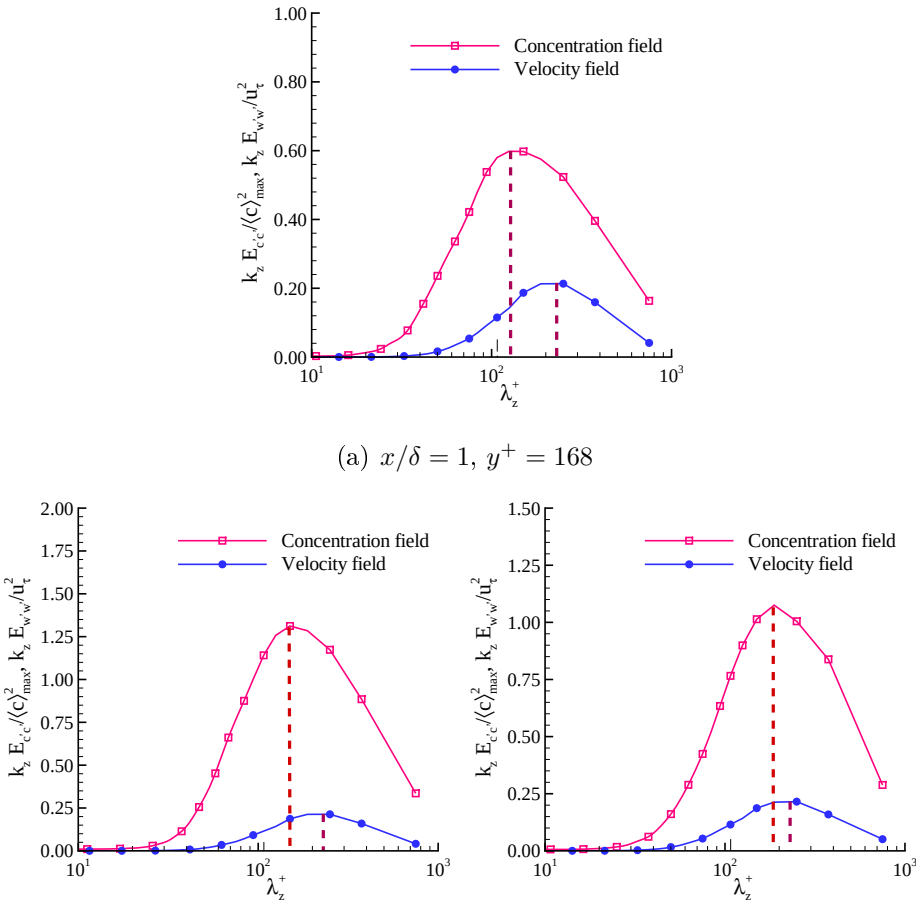

(a) $x/\delta = 1$, $y^+ = 168$

(b) $x/\delta = 6$, $y^+ = 168$

(c) $x/\delta = 12$, $y^+ = 168$

Figure 3.6: Comparison of the pre-multiplied spectra of velocity and concentration fluctuations at the elevation corresponding to the peak of the mean concentration at each downstream location for the plume released from LS2. For LS2, the wall-normal position corresponding to the peak of the mean concentration remains approximately unchanged at different streamwise locations, which is the source elevation $y^+ = y_s^+ = 168$.

location). By contrast, as shown in Fig. 3.6, for the elevated source LS2, a similar transition is not observed over the entire computational domain, clearly indicating that the plume emitting from LS2 remains exclusively in the turbulent convective stage. This physical characteristic of the plume development based on a spectral space analysis is also reflected in the instantaneous plume observed in the physical

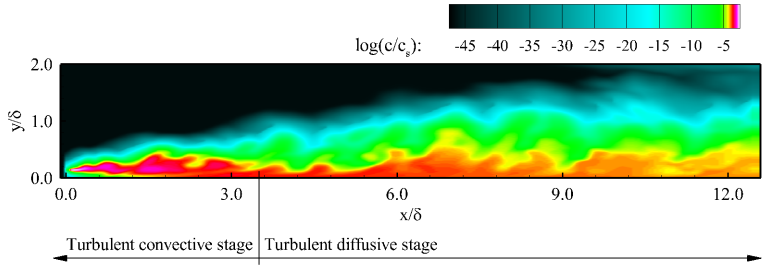

(a) Instantaneous plume released from LS1

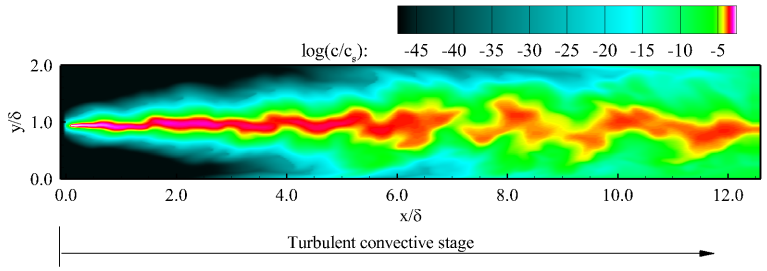

(b) Instantaneous plume released from LS2

Figure 3.7: Contours of instantaneous plumes dispersing from LS1 and LS2.

space. Figure 3.7 compares the instantaneous concentration fields associated with line source emissions from LS1 and LS2. Because the elevations of these two line sources are different, there is an apparent difference in their streamwise plume development patterns. From Fig. 3.7(b), it is seen that the bulk meandering of the plume is indeed evident in the snapshot of the instantaneous plume released from LS2. In contrast, as shown in Fig. 3.7(a), the streamwise development of the plume emitted from LS1 exhibits a more complex pattern. Immediately downstream of the source, the plume size is small and its behavior is typical for an elevated release, and therefore, the plume development is dominated by the meandering effect. However, the plume from LS1 hits the ground soon after its release, and its streamwise development becomes dominated by the wall shear effect. In the near-wall region, the plume spread is larger than the fine length scales of flow structures, and therefore, the plume development becomes dominated by the turbulent diffusion mechanism. According to our previous

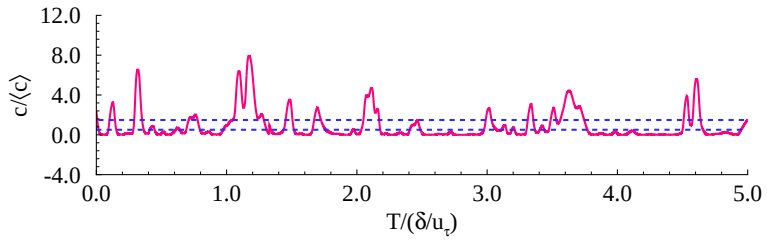

(a) $x/\delta = 1$, $y^+ = 33$

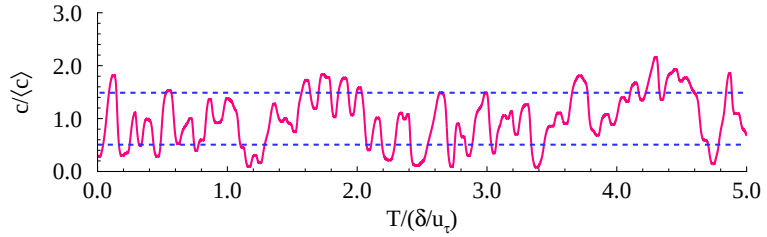

(b) $x/\delta = 12$, $y^+ = 64$

Figure 3.8: The temporal signal at the elevation corresponding to the peak of the concentration fluctuations at two downstream locations of line source LS1.

analysis of Fig. 3.5, the transition from turbulent convective to the turbulent diffusive stage occurs at approximately $x/\delta = 3.5$ for LS1.

To show vividly the inner and external mixing processes associated with the instantaneous plume released from LS1, the temporal signal is further plotted in Fig. 3.8 at two streamwise locations (close to and far away from the source), at the elevation where the local maximum concentration fluctuations occur. As is evident from the figure, near the source at $x/\delta = 1$, the instantaneous concentration level of the plume released from LS1 is not restricted within $0.5 \leq c/\langle c \rangle \leq 1.5$. Occasionally, large peaks (for $c/\langle c \rangle > 1.5$) appear. This indicates that the instantaneous plume released from LS1 is in the turbulent convective stage, where the bulk meandering effects dominate the mixing process, facilitating external concentration fluctuations. However, because the plume from LS1 transitions to the turbulent diffusive stage at $x/\delta = 3.5$, as shown here in Fig. 3.8(b), the temporal signal of the plume released from LS1 at the far downstream location $x/\delta = 12$ is mainly confined within the range of

$0.5 < c/\langle c \rangle < 1.5$, which is an indication of the inner mixing in the turbulent diffusive stage.

3.3.4 Budget of the Mean Concentration Transport Equation

From Eq. (2.3), the following transport equation for the mean concentration can be derived

$$\underbrace{\langle u_j \rangle \frac{\partial \langle c \rangle}{\partial x_j}}_{\text{Convection}} - \underbrace{\alpha \frac{\partial^2 \langle c \rangle}{\partial x_j \partial x_j}}_{\text{Molecular diffusion}} + \underbrace{\frac{\partial}{\partial x_j} \langle c' u_j' \rangle}_{\text{Turbulent diffusion}} = 0 \quad . \tag{3.3}$$

which shows a balance between the molecular diffusion, convection and turbulent diffusion terms. Figures 3.9(a-b) and 3.9(c-d) show the budget balance of these three terms in regions close to and far downstream of the line source (at $x^+ = 30$ and $x^+ = 1080$), respectively. From Figs. 3.9(a) and 3.9(b), it is clear that close to the source, the plume is at the turbulent convective stage, and the budget balance is dominated by the convection and the molecular diffusion terms. In contrast, in the far downstream region, as shown in Figs. 3.9(c) and 3.9(d), the convection term is primarily balanced by the turbulent diffusion term. Furthermore, by comparing Figs. 3.9(a) and 3.9(b), it is clear that in the region immediately downstream of the source, the profiles of these three budget terms are symmetrical about the source location, reflecting the fact of both LS1 and LS2 are elevated sources. However, as is evident from the Figs. 3.9(c) and 3.9(d), in the region far downstream of the source, this symmetry feature is preserved only in the profiles of the budget terms for the plume released from the central-domain source LS2; while the profiles of the budget terms for the plume released from LS1, on the other hand, become non-symmetrical in the wall-normal direction. This reflects the fact that the source location (y_s^+) of LS1 is very close to the wall, the plume hits the ground wall shortly downstream of the source and starts to behave as if it is released from a ground-level source in the

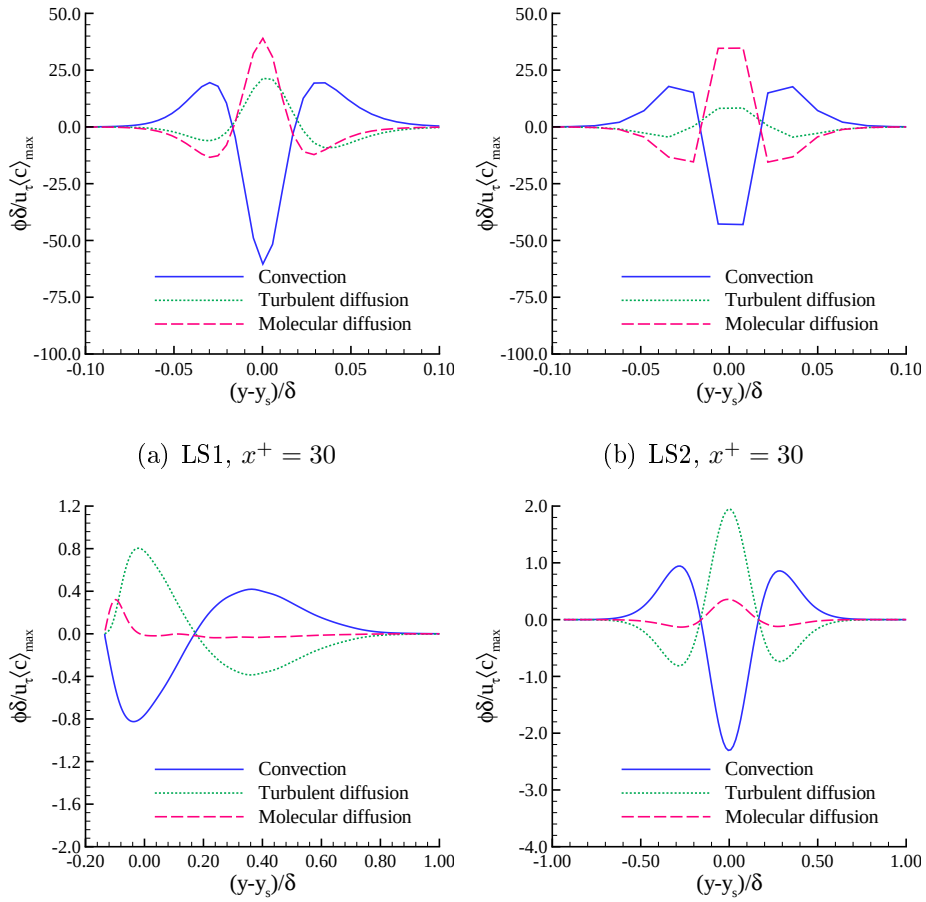

(a) LS1, $x^+ = 30$

(b) LS2, $x^+ = 30$

(c) LS1, $x^+ = 1080$

(d) LS2, $x^+ = 1080$

Figure 3.9: Budget balance of the time-average advection-diffusion equation for two fluctuating plumes released from two line sources LS1 and LS2 at $x^+ = 30$ and $x^+ = 1080$.

far downstream region.

Chapter 4

DNS Study of Passive Plume Interference Emitting from Two Parallel Line Sources in a Turbulent Channel Flow

4.1 Abstract

Turbulent mixing of dual plumes emitting simultaneously from line sources in a turbulent channel flow has been studied using direct numerical simulation (DNS). Three test cases have been compared to investigate the effects of the source separation on turbulent mixing of the two instantaneous plumes.

The dispersion and interference of dual plumes are investigated in both physical and spectral spaces, which include an analysis of statistical moments of the concentration field, the cross-correlation between the two instantaneous plumes, pre-multiplied spectra of the velocity and concentration fields, and co-spectrum and coherency spectrum of the dual plumes. As the downstream distance from the line source increases,

the plume development associated with a single source emission transitions from a turbulent convective stage to a turbulent diffusive stage. It is observed that a plume released from a ground-level source reaches the turbulent diffusive stage faster than that released from an elevated source.

It is also observed that a smaller separation between the two line sources tends to facilitate a more rapid growth in the cross-correlation coefficient of two instantaneous plumes. In the near-source region, the maximum coherency spectrum is produced at lower frequencies indicating that dual-plume mixing is dominated by the external flapping effects of large-scale eddy motions. However, in the far downstream region of the sources, the coherency spectrum in the higher frequency range increases significantly, indicating that the spread of the total plume is larger than all scales of turbulent eddies, such that they all contribute to the in-plume mixing of the dual plumes.

4.2 Problem Description

Figure 4.1 shows the computational domain and coordinate system of the test case. The size of the computational domain is set to $5\pi\delta \times 2\delta \times 2\pi\delta$, where δ is the half channel height. Two parallel line sources of equal strength are positioned at different elevations in the inlet plane of the channel. The flow is fully developed, such that periodical boundary conditions can be applied to both streamwise and spanwise directions for the velocity field. No-slip and no-penetration conditions are enforced at the walls. For the concentration field, a Dirichlet boundary condition is specified in the inlet plane where the two line sources are located, a periodical boundary condition is applied in the spanwise direction, and the zero-Neumann boundary condition is imposed on the wall and over the outlet plane. The purpose of this research is on the turbulent interference and dispersion of passive scalars, and the Reynolds number is fixed at $Re_\tau = u_\tau \delta/\nu = 180$, where u_τ is the wall friction velocity, and ν is the

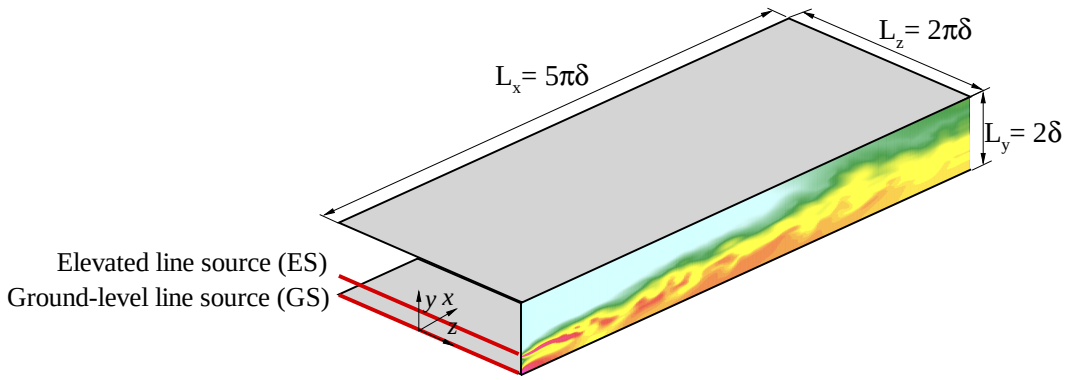

Figure 4.1: Schematic of the computational domain with a ground-level line source and an elevated line source placed in the inlet plane (at $x/\delta = 0$). For the three test cases, there is always a GS fixed at the wall; however, the ES is positioned at $y_s^+ = 2$, 6 and 9 for cases A, B and C, respectively. The two line sources are equal in strength.

kinematic viscosity of the fluid. Three test cases (A, B and C) of different source separation distances are compared. In these three cases, there is one ground-level line source (GS) always fixed at the wall, and one elevated source (ES) positioned at $y_s^+ = 2$, 6 and 9 for cases A, B and C, respectively. Here, the source position is defined as $y_s^+ = y_s u_\tau/\nu$. As such, case A has the smallest source separation, and case C has the largest source separation. In presenting the results, quantities displayed with respect to the wall coordinate are indicated using superscript "+".

To ensure a fine grid resolution demanded by DNS, $320 \times 256 \times 300$ grid points were used in x-, y- and z- directions, respectively. The grid resolution is uniform in the spanwise direction with $\Delta z^+ = 3.7$. The mesh is refined close to the wall and near the line sources. The streamwise grid resolution varies from $\Delta x^+ = 0.5$ near the line sources to $\Delta x^+ = 8.0$ in the far downstream region. The wall-normal grid resolution varies from $\Delta y^+ = 0.2$ in the vicinity of the wall to $\Delta y^+ = 2.51$ at the channel center. Figure 4.2 shows the ratio of the maximum grid size (i.e., $\Delta_{\max} = \max(\Delta x, \Delta y, \Delta z)$) to the Kolmogorov length scale (defined as $\eta = (\nu^3/\epsilon)^{1/4}$) in the wall-normal direction. Here, $\epsilon = \nu\langle \frac{\partial u_i'}{\partial x_k} \frac{\partial u_i'}{\partial x_k} \rangle$ is the local dissipation rate of turbulence kinetic energy (TKE). Clearly, with respect to the Kolmogorov length scale, the grid resolution is sufficiently

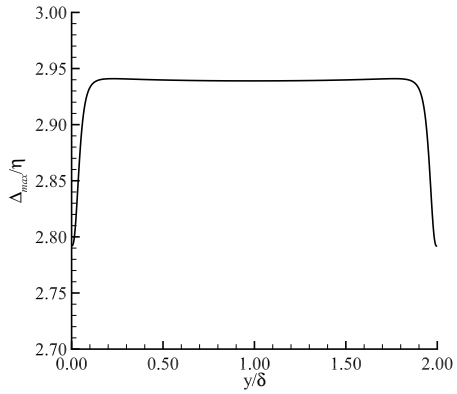

Figure 4.2: Ratio of the maximum grid size (Δ_{max}) to the Kolmogorov scale (η) in the wall-normal direction. The size of the computational domain is $5\pi\delta \times 2\delta \times 2\pi\delta$ with a grid resolution of $320 \times 256 \times 300$ points in the x-, y- and z- directions, respectively.

fine such that $2.79 \leq \Delta_{\max}/\eta \leq 2.93$. As for the time step, the Courant-Friedrichs-Lewy (CFL) number was approximately 0.2.

4.3 Results

4.3.1 Velocity Field

Turbulent dispersion of a passive scalar in a wall-bounded flow is dominated by both convection and molecular diffusion mechanisms. As such, in order to obtain accurate statistical moments of passive scalars, it is required to establish an accurate velocity field first. To this purpose, the quality of the velocity field obtained from the current simulations needs to be examined prior to our analysis of the concentration field. Figure 4.3(a) compares the obtained mean streamwise velocity profile against the DNS data of Kim *et al.* [1] and the conventional law-of-the-wall of von Kármán. Figure 4.3(b) shows the three components of the non-dimensionalized root-mean-square (RMS) velocities (i.e., u^+_{rms}, v^+_{rms} and w^+_{rms}). Both the mean and RMS velocities are in an excellent agreement with the DNS data of Kim *et al.* [1]. The near-wall anisotropic effects are apparent from Fig. 4.3(b). Owing to the presence

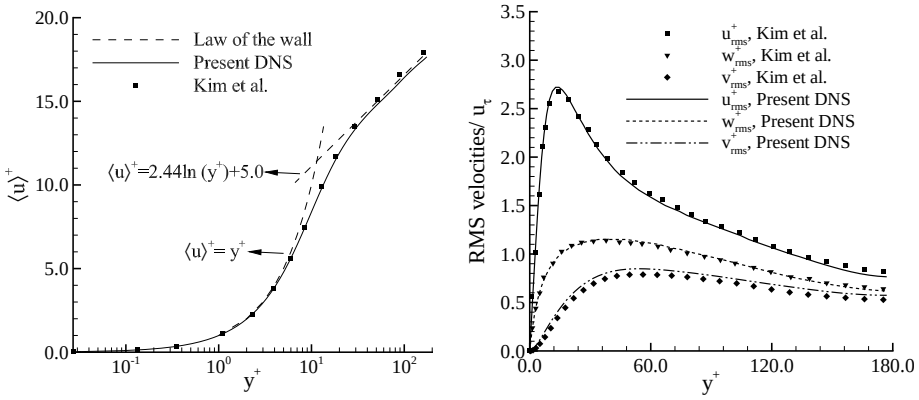

(a) Mean Streamwise velocity

(b) RMS velocities

Figure 4.3: Mean and RMS velocities in comparison with the DNS data of Kim *et al.* [1].

of the strong wall shear, the production rate of TKE is the highest in the near-wall region, which further leads to the peak values in the RMS velocity profiles (especially, for the streamwise component u^+_{rms}). Near the channel center, the discrepancies between the three RMS velocities reduce, leading to a more isotropic condition. These near-wall anisotropic features of the velocity field have a significant impact on the interference and dispersion of two passive plumes to be addressed with great details in the following subsections.

4.3.2 Mean Concentration

The vertical profiles of the mean concentration released from two line sources (GS and ES) are compared in Fig. 4.4 for test cases A, B and C at streamwise location $x^+ = 50$. In the figure, the mean concentration value $\langle c \rangle$ has been normalized by the local maximum mean concentration value $\langle c \rangle_{\max}$. As shown in Fig. 4.4 (a), the normalized mean concentration profile $\langle c \rangle / \langle c \rangle_{\max}$ from ES overlaps that from GS. This is because in case A, the source separation is very small, and the scalar emitting from ES soon hits the wall and behaves like a ground plume. In cases B and C, however,

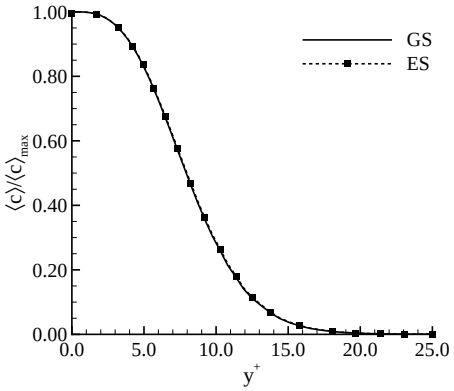

(a) Case A

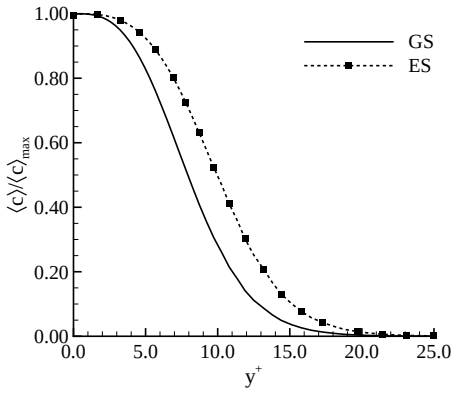

(b) Case B

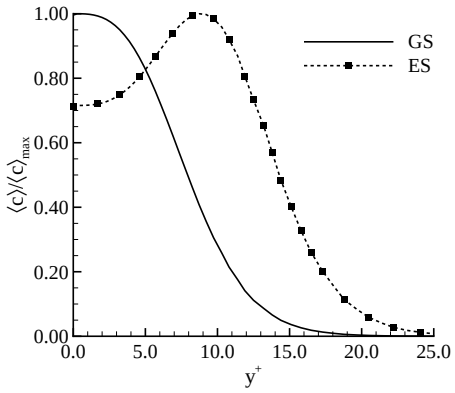

(c) Case C

Figure 4.4: Vertical profiles of the mean concentration released from GS and ES at $x^+ = 50$. The mean concentration value has been normalized by the local maximum mean concentration value $\langle c \rangle_{\max}$.

the separation between GS and ES is relatively large such that the profiles of the mean plumes from these two line sources are distinctively different. Furthermore, owing to the large source separation of case C, the dual plumes emitting from GS and ES peak separately around the source elevations (i.e., at $y_s^+ = 0$ and 9, respectively) at streamwise location $x^+ = 50$ (or, at $x/\delta = 0.278$) in Fig. 4.4(c).

In order to study the streamwise evolution of the vertical profile of the mean concentration, we consider case C which has the largest source separation. Figure 4.5 compares the vertical profiles of $\langle c \rangle / \langle c \rangle_{\max}$ at three locations far downstream of the

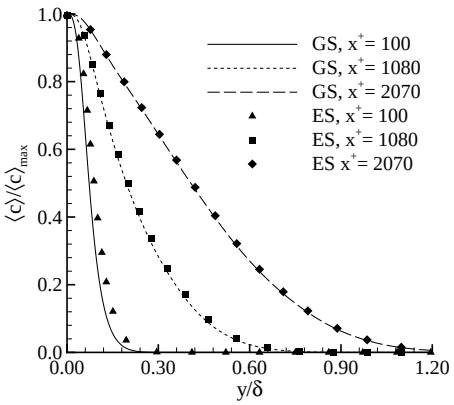

Figure 4.5: Streamwise evolution of the vertical profile of the normalized mean concentration released from GS and ES of case C in the far downstream region of the sources.

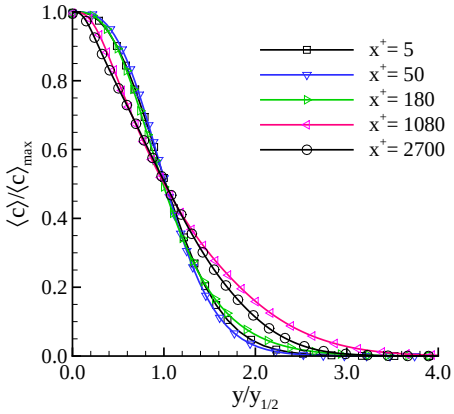

Figure 4.6: Collection of vertical profiles of the mean concentration of the plume released from the ground-level source GS at different streamwise locations.

two line sources (for $x^+ \geq 100$). From Fig. 4.4(c), it is clear that the discrepancy between the vertical profiles of the mean concentration released from GS and ES is very large at $x^+ = 50$. However, as shown in Fig. 4.5, although the discrepancy is still visible, it is much reduced at $x^+ = 100$ (or, at $x/\delta = 0.556$). Further downstream of this position, the two profiles from GS and ES become fully overlapped at $x^+ = 1080$ and 2700. In other words, in case C, in terms of the vertical mean concentration profiles, the difference between the two plumes released from the two line sources starts to vanish as the downstream distance from the two sources goes beyond $x^+ = 100$.

Figure 4.6 compares the vertical profiles of the non-dimensional mean concentration released from the ground-level source GS at different streamwise locations. Given the nature of passive scalar, the behavior of the ground-level plume from GS is identical in cases A, B and C. The mean concentration value has been normalized by the local maximum mean concentration value $\langle c \rangle_{\max}$ and the vertical coordinate has been non-dimensionalized by the half concentration spread $y_{1/2}$ (defined as the vertical distance from the wall at which the mean concentration value drops to one

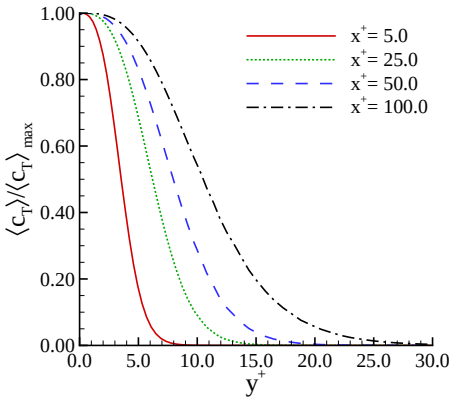

(a) Case A

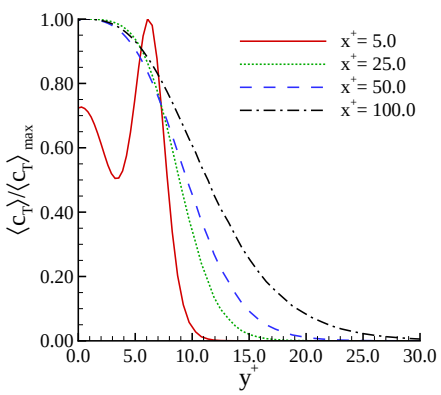

(b) Case B

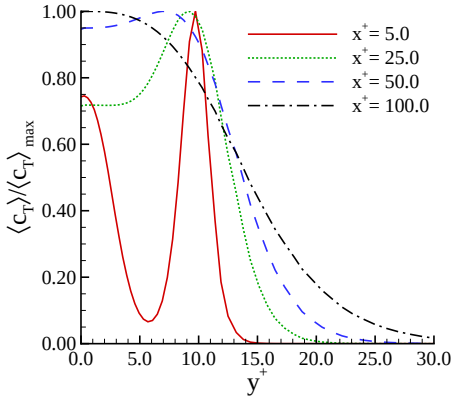

(c) Case C

Figure 4.7: Vertical profiles of the total mean concentration of the dual plumes close to the sources.

half of its maximum local value $\langle c \rangle_{\max}$). This method for plotting Fig.4.6 is analogous to that used for studying the self-similarity of the mean velocity profile of a wall jet [55; 26]. From Fig.4.6, it is very interesting to observe that the vertical profiles of the normalized mean concentration of the plume released from the ground-level source at different streamwise locations do not severely deviate from each other (as x^+ varying from 5 to 2700), and collectively, exhibit a consistent quasi-self-similar pattern.

Figure 4.7 shows the total mean concentration profile of the dual plumes in the

downstream region near the two line sources. As is evident in Fig. 4.7(a), a half Gaussian profile is observed in the total mean concentration field in case A. This is not surprising, because the source separation is the smallest in case A, and the total plume behaves as if it is emitted from one single ground-level line source. However, as shown in Fig. 4.7(b), in case B, the influence of the two line sources on the total mean concentration is direct and apparent immediately downstream of the sources at $x^+ = 5$ because $\langle c_T \rangle / \langle c_T \rangle_{max}$ peaks around the two source elevations (at $y^+ = 0$ and 6 for GS and ES, respectively). From Fig. 4.7(b), it is clear that this distinction between the two line sources soon vanishes as the streamwise distance goes beyond $x^+ = 25$. In the far downstream region from the two sources, the elevation difference between GS and ES has no effect on the shape of the total plume. This is because the plume from the ES hits the ground soon after it is released, and as such, the total plume only sees an equivalent ground-level source in the far downstream region for $x^+ \geq 25$. In case C, the source separation is the largest among the three test cases. As is clear in Fig. 4.7(c), the influence of the two line sources on the total plume is apparent in the profile of the total mean concentration at $x^+ = 5$, 25 and 50. However, the total plume exhibits a half Gaussian profile as x^+ reaches 100, indicating that the total plume is no longer influenced by the elevation of ES and shows a typical ground-source emission feature at this far downstream location.

4.3.3 Concentration Variance

Figure 4.8 compares the RMS concentration profiles of the individual plumes released from the ground-level and elevated sources at downstream location $x^+ = 50$ for cases A, B and C. The RMS concentration value c_{rms} has been normalized by its local maximum value $\max(c_{rms})$. Apparently, at this downstream location of $x^+ = 50$, the discrepancy between the two RMS concentration profiles of GS and ES is larger in cases B and C than in case A. Furthermore, it is observed that in all three test cases, the profile of c_{rms} mostly exhibits a single-peak pattern associated with GS and ES,

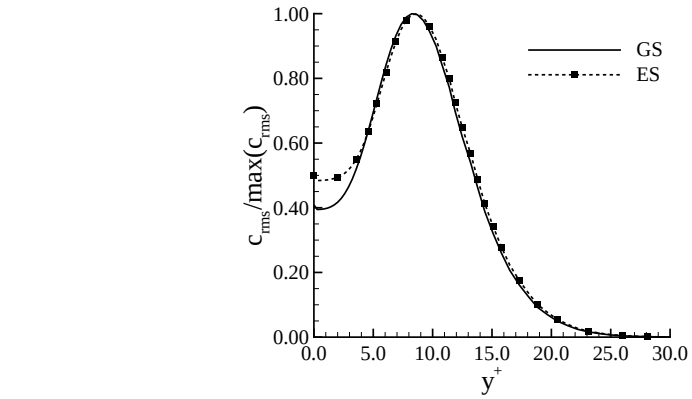

(a) Case A

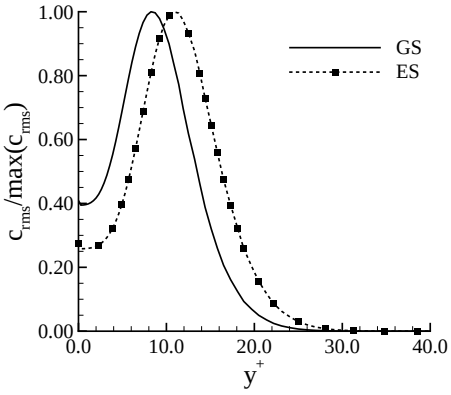

(b) Case B

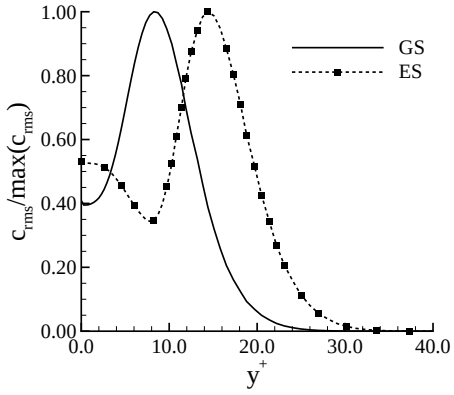

(c) Case C

Figure 4.8: Vertical profiles of the RMS concentration at $x^+ = 50$ for individual plumes released from GS and ES in cases A, B and C. The RMS concentration value c_{rms} has been normalized using its local maximum value $\max(c_{rms})$.

except for the profile associated with the elevated source ES in case C. The physical explanation for this difference is given as follows. Typical for a single plume in a free shear flow away from solid walls, the mean concentration field exhibits a full Gaussian profile. On each side of the Gaussian profile, there is an inflection point where the mean concentration gradient $|\partial\langle c\rangle/\partial x_2|$ is the largest. The position where the turbulent production rate $(-2\langle c'u_i'\rangle \cdot \partial\langle c\rangle/\partial x_i)$ for the concentration variance reaches the maximum often coincides with the inflection point. This leads to a dual-peak pattern in the RMS concentration profile. As shown in Fig. 4.8(c), for the

single plume released from the elevated source ES of case C, the presence of a dual-peak pattern in c_{rms} is evident at $x^+ = 50$. Apparently, this dual-peak pattern is non-symmetrical due to the presence of the wall. In contrast, for the single plume released from the ground-level source GS of case C, the profile of c_{rms} exhibits a single peak pattern, which is similar to that shown in Figs. 4.8(a) and 4.8(b). This feature is expected. From Fig. 4.4, it is clear that the mean plume shows only one half of the Gaussian profile at $x^+ = 50$ for GS and ES in cases A and B, and for GS in case C. This behavior of the mean plume is typical for a ground-level source release. Although line source ES is elevated in cases A and B, its position is relatively close to the wall in these two test cases. As such, the plume released from ES soon hits the ground and behaves as a ground-source release at downstream location $x^+ = 50$ in cases A and B. As a result of the one-half Gaussian mean concentration profile (shown in Fig. 4.4), there is only one inflection point corresponding to one single peak in the RMS concentration profile for GS and ES in cases A and B shown in Figs. 4.8(a) and 4.8(b), and for GS in case C shown in Fig. 4.8(c).

Figure 4.9 further shows the streamwise evolution of the RMS concentration profiles of case C in the region relatively far from sources at $x/\delta = 0.5$–15 (or, $x^+ = 90$–2700). The plume released from the elevated source ES eventually hits the ground and then behaves as if it is released from a ground-level source in the far downstream region. Therefore, the plume released from either GS or ES is expected to exhibit a single-peak pattern in the profile of the RMS concentration in the downstream region far from the source (for $x^+ \geq 90$), a feature that is evident in Fig. 4.9. Furthermore, as shown in Fig. 4.9(a) and 4.9(b), at $x/\delta = 0.5$ and 1 (or, $x^+ = 90$ and 180, respectively), the discrepancy between the two RMS concentration profiles of GS and ES is apparent. However, as shown in Figs. 4.9(c) and 4.9(d), these two RMS concentration profiles eventually collapse at $x/\delta = 6$ and 15, indicating that in the far downstream region of the two sources, the differences between the two sources vanish, and the two plumes behave as if they were released from the same ground-level source GS. In other

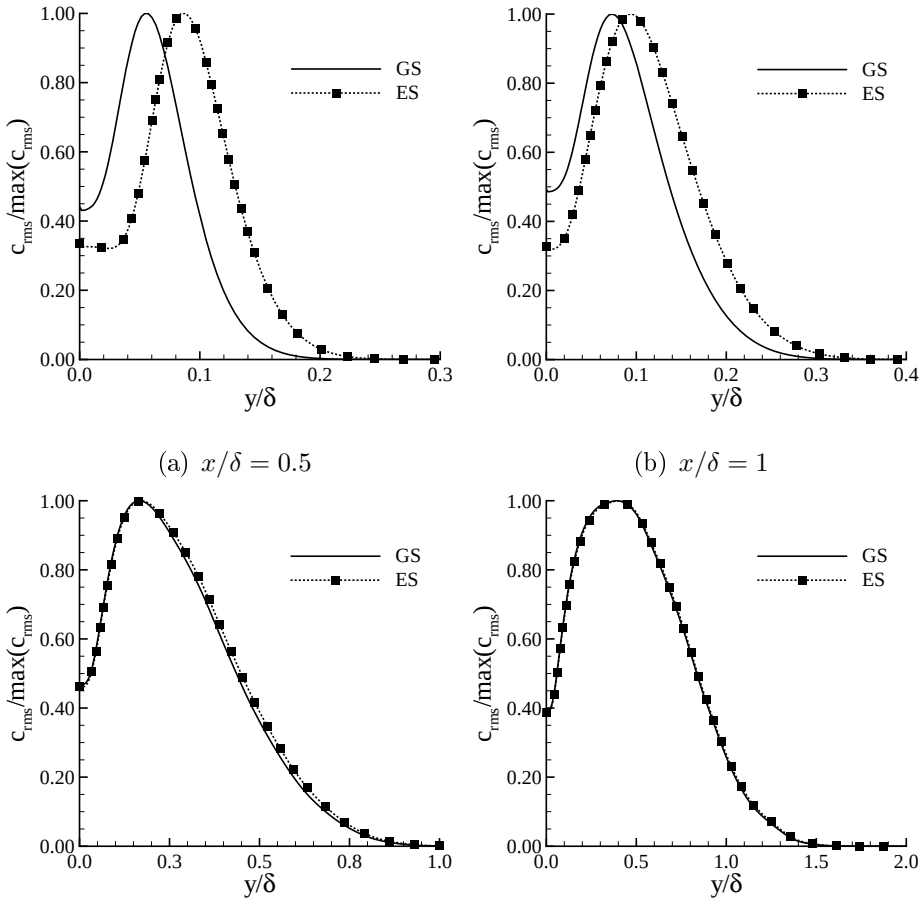

(a) $x/\delta = 0.5$ (b) $x/\delta = 1$

(c) $x/\delta = 6$ (d) $x/\delta = 15$

Figure 4.9: Profiles of the RMS concentration of individual plumes released from GS and ES of case C at four different streamwise locations. The RMS concentration value c_{rms} has been normalized using its local maximum value $\max(c_{rms})$.

words, in the far downstream region for $x/\delta \geq 6$, the concentration fluctuations of the plume released from ES are no longer sensitive to the source elevation (at $y_s^+ = 9$ in the inlet plane located at $x^+ = 0$) in case C, such that the RMS concentration profile of the plume released from the elevated source ES is identical to that from the ground-level source GS.

In accordance with the convection-diffusion equation that governs the transport of the passive scalar, the mean concentration fields from the two line sources are

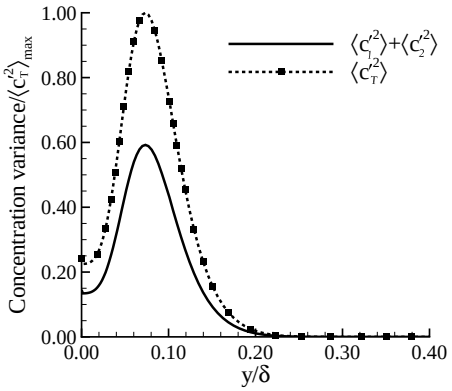

(a) Case A

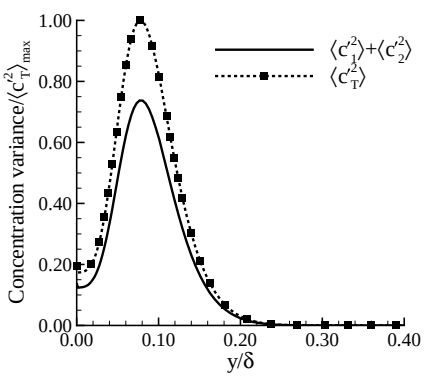

(b) Case B

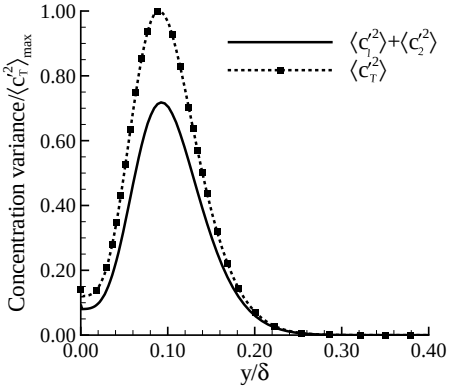

(c) Case C

Figure 4.10: Vertical profiles of the concentration variance of the total plume $\langle c_T'^2 \rangle$, and the summation of the concentration variances of two individual plumes $\langle c_1'^2 \rangle + \langle c_2'^2 \rangle$ at $x^+ = 180$ (or, $x/\delta = 1$).

superposable. However, the second-order statistical moments of the concentration cannot be superimposed due to their nonlinear relationship, i.e. $\langle c_T'^2 \rangle \neq \langle c_1'^2 \rangle + \langle c_2'^2 \rangle$. Specifically, the difference between the variance of the total plume and the summation of variances of two individual plumes lies in the so-called co-variance ($\langle c_1' c_2' \rangle$) of the two plumes, i.e. $\langle c_T'^2 \rangle = \langle (c_1' + c_2')^2 \rangle = \langle c_1'^2 \rangle + \langle c_2'^2 \rangle + 2\langle c_1' c_2' \rangle$. The better mixing of two instantaneous plumes, the higher the value of the co-variance between the two. As such, it is expected that the discrepancy between $\langle c_T'^2 \rangle$ and $(\langle c_1'^2 \rangle + \langle c_2'^2 \rangle)$ reaches

the maximum, where the mixing and interaction of the two plumes are the most intense. Figure 4.10 compares the total RMS concentration with the summation of variances of the two plumes at $x^+ = 180$ for different cases. As is clear from the figure, the variance of the total plume $\langle c_T'^2 \rangle$ is much larger than the resultant value of the simple summation of concentration variances of two individual plumes ($\langle c_1'^2 \rangle + \langle c_2'^2 \rangle$) at downstream location $x/\delta = 1$ in all three cases. Furthermore, the value of this discrepancy (or, twice the co-variance), i.e. $2\langle c_1' c_2' \rangle \equiv \langle c_T'^2 \rangle - (\langle c_1'^2 \rangle + \langle c_2'^2 \rangle)$ is apparently the largest in case A, which has the smallest source separation among all three test cases.

4.3.4 Spectral Analysis of the Concentration Field

There are three different stages in the streamwise development of a single instantaneous plume, which are the molecular diffusive, turbulent convective, and turbulent diffusive stages [14; 32]. In the molecular diffusive stage, the spread of an instantaneous plume is smaller than the Kolmogorov scale, the smallest length scale of turbulent motions. In the turbulent convective stage, the spread of the instantaneous plume becomes larger than the Kolmogorov scale but smaller than the characteristic scale of the most energetic turbulent eddies. If the eddy scales are smaller than the instantaneous plume spread, they contribute to internal fluctuations and relative dispersion. However, if the eddy scales are larger than the instantaneous plume spread, they contribute to the external fluctuations and bulk meandering of the plume. In the turbulent diffusive stage, the spread of the instantaneous plume becomes comparable to or larger than the scale of the most energetic turbulent eddies, and scalar fluctuations are dominated by internal fluctuations associated with the in-plume mixing processes. In order to determine whether a plume is in the turbulent convective or diffusive stage, the dispersion of the centroid of the instantaneous plume and the mean plume dispersion need to be calculated to define the meandering ratio for a three-dimensional (3-D) plume released from a point source [32].

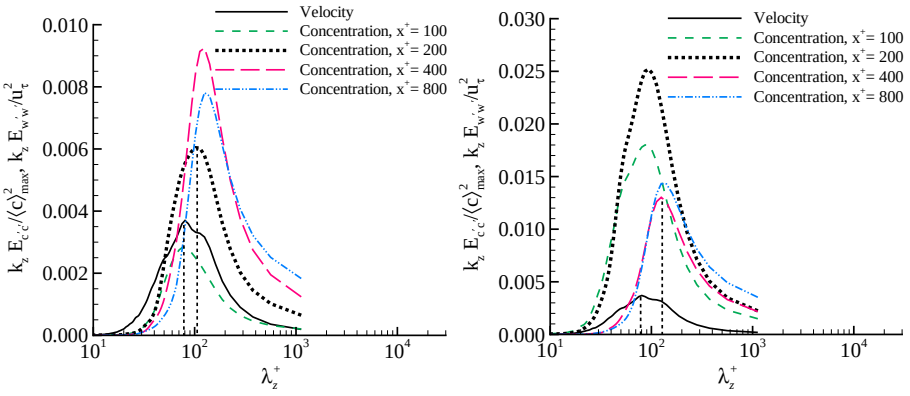

(a) Ground-level source GS of case A (b) Elevated source ES of case C

Figure 4.11: Comparison of pre-multiplied spectra of the spanwise velocity and concentration fields at different streamwise locations. The spectra for all cases are extracted at a fixed elevation $y^+ = 0.2$.

In contrast to the previous studies [14; 32; 33; 17], which have focused exclusively on the lateral plume development in the homogeneous direction of the flow, two new challenges are involved in the present study which investigates the two-dimensional (2-D) plume development under the influence of wall anisotropy. Firstly, due to the lack of a full Gaussian distribution in the concentration field in the wall-normal direction of a boundary layer, it is not possible to directly calculate the meandering ratio under wall anisotropy. Secondly, in the spanwise direction, because the plume is released from a line source, the plume development is 2-D, and in theory, the mean plume width is infinite (as implied in the spanwise periodical boundary condition of the concentration field). As such, a meaningful characteristic length scale needs to be properly defined in order to quantify the plume development in the spanwise direction.

In view of the above challenges, in order to effectively differentiate the convective and turbulent diffusive stages, a new alternative approach based on a spectral analysis can be considered. The idea behind the proposed alternative approach arises from the presence of homogeneity in the velocity and concentration fields in the span-

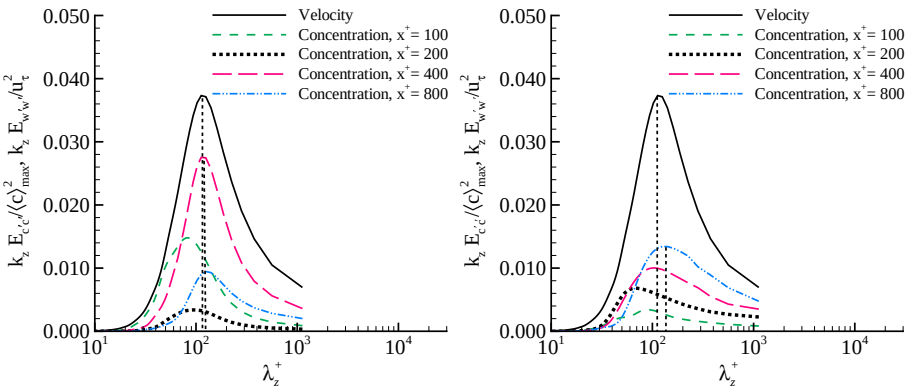

(a) Ground-level source GS of case A (b) Elevated source ES of case C

Figure 4.12: Comparison of pre-multiplied spectra of the spanwise velocity and concentration fields at different streamwise locations. The spectra for all cases are extracted at a fixed elevation $y^+ = 5$. The order of the magnitude is different for the pre-multiplied spectra of the velocity and concentration fields. In order to compare these two quantities (especially, the modes), the pre-multiplied spectrum of the velocity has been reduced by a factor of 10.

wise direction. The mixing and dispersion of a passive scalar depend on the scales of energetic eddies, which can be studied by analyzing the spanwise spectra of the velocity and scalar fields, i.e. $E_{w'w'}(k_z) = \frac{1}{\pi}\int_{-\infty}^{+\infty} e^{-ik_z r} R_{w'w'}(r)dr$ and $E_{c'c'}(k_z) = \frac{1}{\pi}\int_{-\infty}^{+\infty} e^{-ik_z r} R_{c'c'}(r)dr$, respectively. Here, $R_{w'w'}(r) = \langle w'(z)w'(z+r)\rangle / w_{rms}^2$ and $R_{c'c'}(r) = \langle c'(z)c'(z+r)\rangle / c_{rms}^2$ are the spanwise correlation functions of the velocity and concentration fields, respectively. The modes ($\lambda_{z,w'}^m$ and $\lambda_{z,c'}^m$) of the pre-multiplied spectra ($k_z E_{w'w'}$ and $k_z E_{c'c'}$) of the velocity and concentration fields correspond to the characteristic length scales of the most energetic eddy motions responsible for turbulent velocity and concentration fluctuations, respectively. Here, superscript 'm' denotes 'mode', $\lambda_z^+ = \lambda_z u_\tau/\nu$, $\lambda_z \equiv 2\pi/k_z$ is the spanwise wavelength, and k_z denotes the spanwise wavenumber. Given the spanwise homogeneity of the velocity and concentration fields, the following identities strictly hold for the mean and fluctuating values of the velocity and concentration fields: $\langle w\rangle_s \equiv 0$, $\langle w'\rangle_s \equiv 0$, $\langle c\rangle_s \equiv$ constant, and $\langle c'\rangle_s \equiv 0$. Here, $\langle\cdot\rangle_s$ denotes time- and spanwise-averaging. As such, the spectral

analysis conducted in the spanwise direction based on the fluctuating components w' and c' is equivalent to that based on the instantaneous values of w and c. Therefore, the mode $\lambda^m_{z,c'}$ of pre-multiplied spectrum $k_z E_{c'c'}$ also indicates the spanwise characteristic length scale of an instantaneous plume released from a line source. Furthermore, it should be indicated that the velocity field is homogeneous over an arbitrary x-z plane, and in consequence, the characteristic length scale of large energetic eddy motions as indicated by the mode of $k_z E_{w'w'}$ varies with the wall-normal distance y^+ only, i.e., $\lambda^{m+}_{z,w'} = \lambda^{m+}_{z,w'}(y^+)$. However, because the 2-D plume is homogeneous in the spanwise direction and developing in the streamwise direction, the mode of $k_z E_{c'c'}$ varies with not only the wall-normal distance y^+ but also the streamwise distance x^+ from the line source, i.e. $\lambda^{m+}_{z,c'} = \lambda^{m+}_{z,c'}(x^+, y^+)$. Thus, the transition from the turbulent convective stage (where the meandering effect dominates) to the turbulent diffusive stage (where the in-plume mixing effect dominates) of plume dispersion can be alternatively determined by comparing the modes of the pre-multiplied spectra of the velocity and concentration fields (associated with a 2-D line source emission in a wall-bounded flow). At a given wall-normal position y^+, if $\lambda^{m+}_{z,w'} > \lambda^{m+}_{z,c'}$, then the characteristic length scale of energetic eddy motions is larger than that of the plume, and consequently, the dispersion is considered to be at a turbulent convective stage; however, if $\lambda^{m+}_{z,w'} < \lambda^{m+}_{z,c'}$, then the characteristic length scale of energetic eddy motions is smaller than that of the plume, and as a result, the dispersion is considered to be at a turbulent diffusive stage.

Figure 4.11 compares the pre-multiplied spectra of the velocity and concentration fields for cases A and C (which feature the smallest and largest source separations in the three test cases). The pre-multiplied spectra of both the velocity and concentration are calculated at a fixed elevation of $y^+ = 0.2$ (the wall-normal distance of the first node off the wall), where the mean concentration value of either GS or ES is close to its local maximum in the far downstream region of the sources (see Fig. 4.9). As shown in Fig. 4.11 (a), for GS of case A, the characteristic length scale

inferred from the mode of the pre-multiplied concentration spectrum exceeds that of the pre-multiplied velocity at $x^+ = 200$, indicating the transition in plume dispersion from the turbulent convective stage to the turbulent diffusive stage occurs around this downstream location. However, as shown in Fig. 4.11(b), this transition for the elevated source of case C is postponed to $x^+ = 400$, clearly indicating that the plume emitting from a ground-level source transitions to the turbulent diffusive stage more rapidly than that from an elevated source. For the plume development of a single line source in a boundary layer, the mixing process also depends on the wall-normal position. In order to further demonstrate the wall effect, the pre-multiplied power spectra of the velocity and concentration field are extracted also at $y^+ = 5$ for cases A and C, and displayed in Fig. 4.12. As shown in Fig. 4.12, for GS of case A, the characteristic length scale inferred from the mode of the pre-multiplied concentration spectrum exceeds that of the pre-multiplied velocity spectrum at $x^+ = 400$, indicating the transition in plume dispersion from the turbulent convective stage to the turbulent diffusive stage occurs around this downstream location. By comparing Fig. 4.11(a) with Fig. 4.12(a), it is clear that as the wall-normal distance increases from $y^+ = 0.2$ to 5, the transition from the turbulent convective stage to the turbulent diffusive stage is postponed from $x^+ = 200$ to 400. Similarly, by comparing Fig. 4.11(b) with Fig. 4.12(b), it is clear that as the wall-normal distance increases from $y^+ = 0.2$ to 5, the streamwise location where the transition occurs is delayed significantly from $x^+ = 400$ to 800.

Figure 4.13 compares the contours of pre-multiplied spectrum $k_z E_{c'c'}$ of the ground-level line source GS of case A at three downstream locations. From Fig. 4.13, it is clear that as the downstream distance from the source increases from $x^+ = 5$ to 960, the turbulent scalar energy (TSE) becomes more spread. Furthermore, the center of the contours of TSE for the ground-source release case elevates slightly along the streamwise direction, and as a result, the spanwise scale of the concentration fluctuations increases slightly from $\lambda_z^+ = 100$ to 140. Figure 4.14 shows the contours of $k_z E_{c'c'}$ of

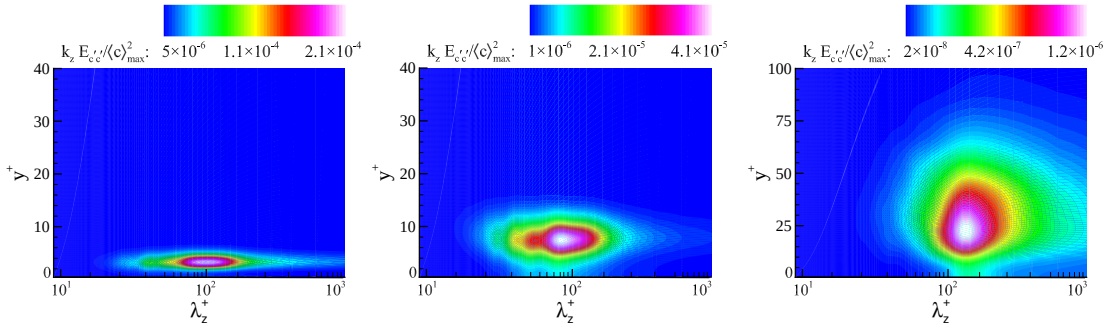

(a) $x^+ = 5$ (b) $x^+ = 50$ (c) $x^+ = 960$

Figure 4.13: Contours of pre-multiplied power spectrum $k_z E_{c'c'}$ of the concentration field emitting from the ground-level line source GS at three streamwise locations in case A.

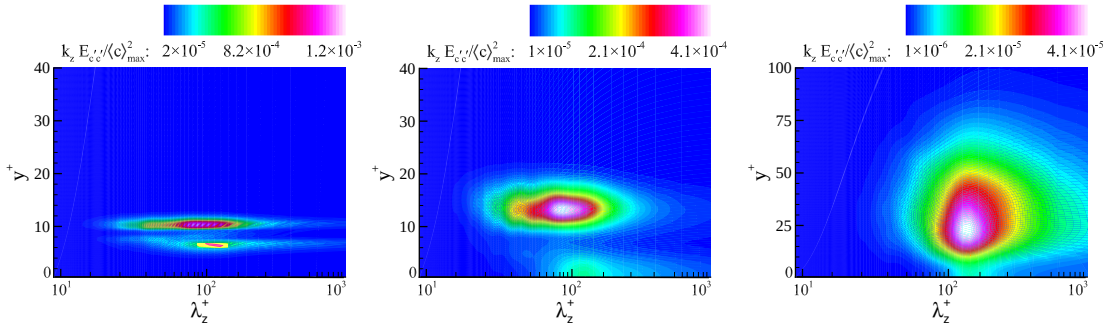

(a) $x^+ = 5$ (b) $x^+ = 50$ (c) $x^+ = 960$

Figure 4.14: Contours of pre-multiplied power spectrum $k_z E_{c'c'}$ of the concentration field emitting from the elevated line source ES at three streamwise locations in case C.

the elevated line source ES of case C at three downstream locations. As is evident in Fig. 4.14(a), there are two peaks in the contours of the pre-multiplied power spectra of the concentration field, with the stronger peak positioned at a higher elevation, and the weaker one positioned a lower elevation. This is because there are two inflection points in the mean concentration profile associated with the elevated source of case C (see also Fig. 4.4(c)) where the maximum production rates for TSE occur. Further downstream of the line source as shown in Fig. 4.14 (b-c), the contours of

the pre-multiplied spectra transition from a dual-peak to a single-peak pattern. This is because the plume has hit the ground at a certain downstream location near the line source, and starts to behave in a manner as if it was emitted from a ground-level source in far downstream regions, a physical feature that is fully consistent with that of the RMS concentration profile shown previously in Fig. 4.9.

4.3.5 Cross-correlation, Co-Spectra and Coherency Spectra

The pre-multiplied spectrum analysis conducted above does not give any precise information about the quality of mixing of two fluctuating plumes. To find out, the cross-correlation coefficient, pre-multiplied co-spectra and coherency spectra of the two fluctuating plumes can be further examined. The cross-correlation coefficient is defined as:

$$\rho_{cc} \equiv \frac{\langle c_1' c_2' \rangle}{\left(\langle {c_1'}^2 \rangle\right)^{\frac{1}{2}} \left(\langle {c_2'}^2 \rangle\right)^{\frac{1}{2}}} = \frac{\langle c_1 c_2 \rangle - \langle c_1 \rangle \langle c_2 \rangle}{\left(\langle {c_1'}^2 \rangle\right)^{\frac{1}{2}} \left(\langle {c_2'}^2 \rangle\right)^{\frac{1}{2}}} \quad . \tag{4.1}$$

There are four regimes in the development of dual plumes mixing [32], so-called (1) zero interference (corresponding to $\rho_{cc} = 0$), (2) destructive interference (corresponding to $\rho_{cc} < 0$), (3) constructive interference (corresponding to $0 < \rho_{cc} < 1$), and (4) complete mixing (corresponding to $\rho_{cc} = 1$). Figure 4.15 shows the minimum cross-correlation coefficient between the two instantaneous plumes. In the first regime (zero interference), the receptor is immediately downstream of the sources. As such, there is no interaction between the two plumes, and the covariance of two plumes is zero (i.e., $\langle c_1' c_2' \rangle = \langle c_1 c_2 \rangle - \langle c_1 \rangle \langle c_2 \rangle = 0$). The physical feature of zero interference ($\rho_{cc} = 0$) in the near-source region is evident in Fig. 4.15 for all three test cases. The presence of the second regime of destructive interference ($\rho_{cc} < 0$) is also evident in Fig. 4.15, where the mean spread of a single plume becomes larger than the source separation. As such, $\langle c_1 c_2 \rangle < \langle c_1 \rangle \langle c_2 \rangle$. A relatively large eddy motion can transport concentration from one plume to the other, resulting in a negative correlation between the two plumes in the sense that the concentration decreases in one plume

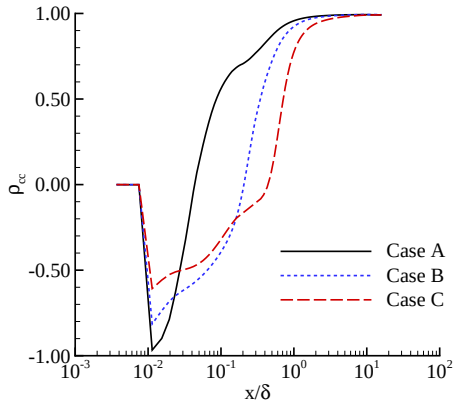

Figure 4.15: Minimum cross-correlation coefficient between two instantaneous plumes.

while simultaneously increases in the other plume. In the third regime (featuring constructive interference and $0 < \rho_{cc} < 1$), besides the meandering effect, the internal mixing of the two plumes is significantly enhanced due to turbulent motions of relatively small-scale eddies, which lead to an increasing correlation between the two plumes, such that $\langle c_1 c_2 \rangle > \langle c_1 \rangle \langle c_2 \rangle$. From Fig. 4.15, it is evident that the smaller the source separation, the faster the growth in the value of ρ_{cc}. Finally, in the fourth regime (complete mixing), the source separation becomes negligible compared to the far downstream distance from the sources, and the total plume reaches a full mixing state and behaves as if it is emitted from the same source. As is evident from the figure, in this complete mixing regime, $\rho_{cc} \to 1$. Also, because all regimes have been well captured in all three test cases, it is apparent that the streamwise computational domain size $L_1 = 5\pi\delta$ ($L_1^+ = 2827.4$) is adequate for the current DNS study of dual-plume interference. It should be indicated here that in order to study the dual-plume interference between an ES and a fixed GS (with $y_s^+ \equiv 0$), three elevations of the ES have been tested, limited to $y_s^+ \leq 9$. If a much larger source separation (for $\Delta y_s^+ > 9$) is tested, then a longer streamwise domain may be needed in DNS in order to fully capture the four regimes of the dual-plume mixing.

Figure 4.16 compares the vertical profiles of the cross-correlation coefficient at five

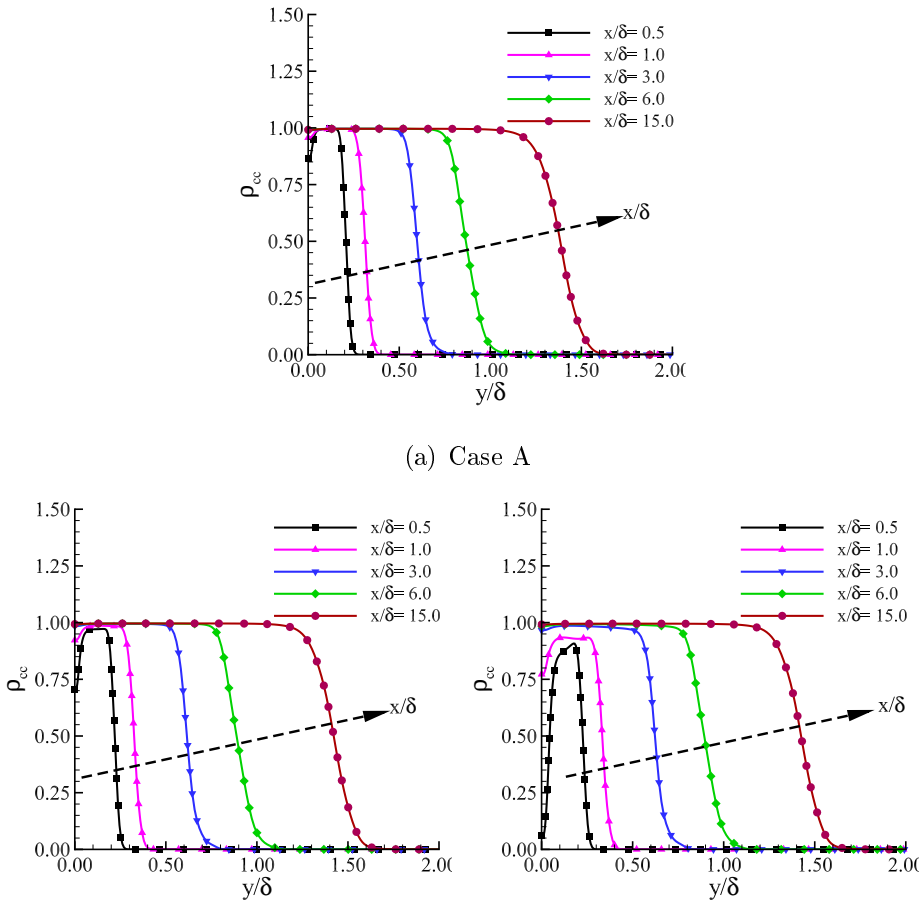

(a) Case A

(b) Case B

(c) Case C

Figure 4.16: Streamwise evolution of the vertical profile of the cross-correlation coefficient ρ_{cc}.

locations downstream of the two line sources (with x/δ varying from 0.5 to 15). As is clear from Fig. 4.16, in cases A and B, a complete mixing state is reached once the downstream distance from the sources goes beyond $x/\delta = 1$ (or, $x^+ = 180$). In contrast, in case C, two plumes apparently deviate from the complete mixing state at $x/\delta = 0.5$ and $x/\delta = 1$, reflecting the fact that the source separation is larger in case C than in cases A and B. From Fig. 4.15, it is clear that the streamwise computational domain size is large enough for the two plumes to reach a complete mixing stage ($\rho_{cc} \to 1$) at approximately $x/\delta = 3$ in all cases.

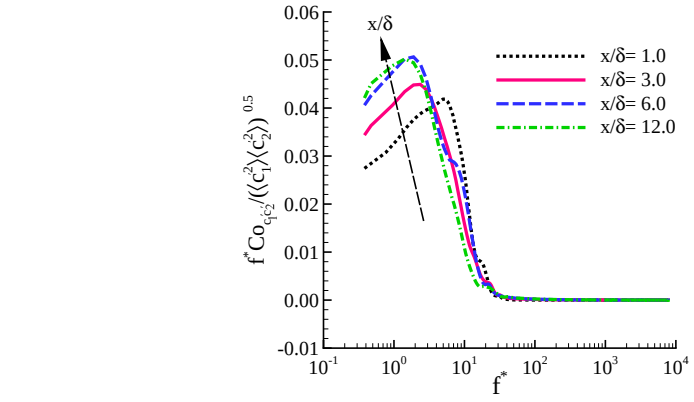

(a) Case A

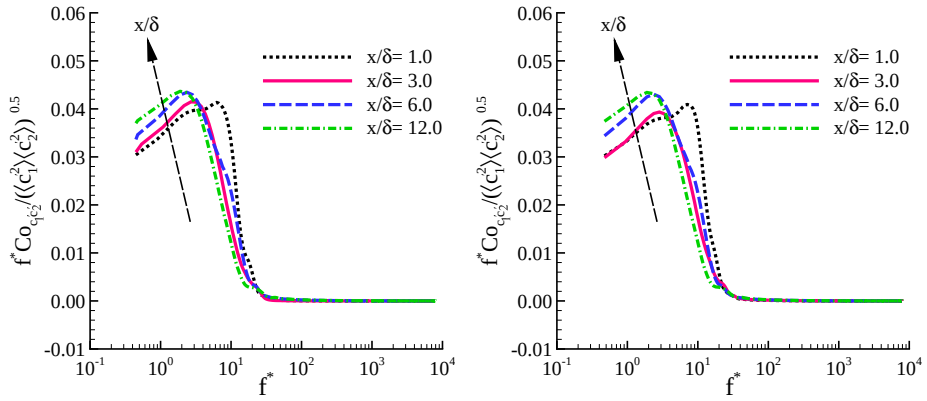

(b) Case B

(c) Case C

Figure 4.17: Non-dimensionalized pre-multiplied co-spectrum of two plumes at four locations downstream of the two line sources.

Because the mixing of two plumes is a multi-scale phenomenon, in order to refine our study of the quality of mixing of two plumes, the pre-multiplied co-spectrum $Co_{c_1'c_2'}(f)$ and coherency spectrum $\rho_{cs}(f)$ can be further studied, which are defined as:

$$Co_{c_1'c_2'}(f) = (E_{c_T'c_T'}(f) - E_{c_1'c_1'}(f) - E_{c_2'c_2'}(f))/2 \quad , \tag{4.2}$$

and

$$\rho_{cs}(f) = Co_{c_1'c_2'}(f)/(E_{c_1'c_1'}(f)E_{c_2'c_2'}(f))^{0.5} \quad , \tag{4.3}$$

respectively. Here, f represents the temporal frequency. Figure 4.17 shows the

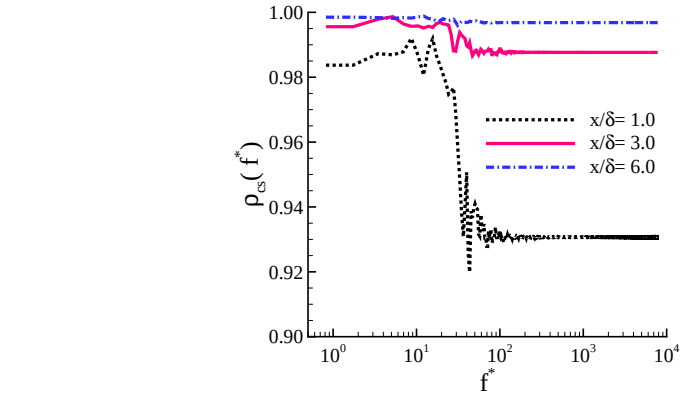

(a) Case A

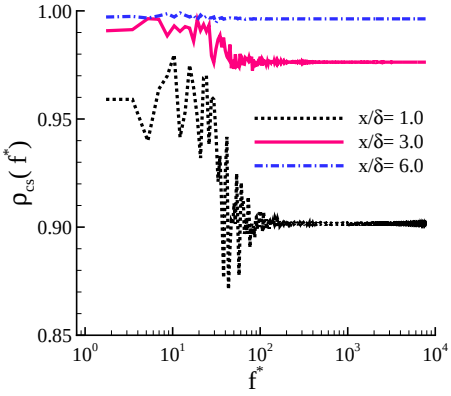

(b) Case B

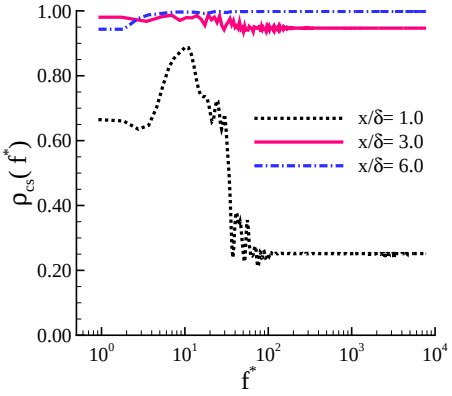

(c) Case C

Figure 4.18: Coherency spectrum of dual plumes at three locations downstream of two line sources.

streamwise evolution of the non-dimensionalized pre-multiplied co-spectrum $f^*Co_{c_1'c_2'}$ of the three test cases studied. Here, the non-dimensional frequency is defined as the Strouhal number, i.e. $f^* = f\delta/u_\tau$. Clearly, the mode of the pre-multiplied co-spectrum decreases as x/δ increases from 1 to 6, indicating an increasing characteristic length scale of the dual-plume mixing. However, as the downstream distance, further increases from $x/\delta = 6$ to 12, the mode of the pre-multiplied co-spectrum is stabilized at approximately $f^* = 2$. A stable value of f^* in the far downstream region indicates that the mixing has reached a turbulent diffusive state, where the characteristic size

of the total plume is much larger than that of energetic eddies. In order to make this point clearer in physics, the coherency spectrum of the two plumes is calculated and shown in Fig. 4.18. As is evident from the figure, in all three test cases, at the two near-source locations $x/\delta = 1$ and $x/\delta = 3$, the maximum coherency spectrum is produced at lower frequencies (corresponding to the large-eddy turn-over period of approximately $2\delta/u_\tau$). This indicates that dual-plume mixing is dominated by the external flapping effects of large-scale eddy motions in the downstream regions near the two sources where the size of the plume is much smaller than that of turbulent eddies. In contrast, as the downstream distance reaches $x/\delta = 6$, the coherency spectrum in the higher frequency range increases significantly. The value of the coherency spectrum ρ_{cs} is close to its asymptotic value of unity across the entire frequency space, indicating that the plume is already in the complete mixing state. At this stage, the plume size is larger than all scales of turbulent eddies (of all frequencies), such that they all contribute to the in-plume mixing, revealing that the internal mixing is dominant in the dispersion process in regions far downstream of the dual sources.

Chapter 5

Study of Vertical Line Source Dispersion in a Turbulent Channel Flow

5.1 Abstract

Turbulent dispersion of passive concentration released from a vertical line source in a fully-developed channel flow is studied using direct numerical simulation (DNS). The investigation into the turbulent transport processes of the momentum and concentration is conducted in both physical and spectral spaces, based on a systematic analysis of the statistical moments of the velocity and concentration fields, probability density functions (PDFs) of the concentration fluctuations, and the characteristic wavelengths of energetic eddies that dominate turbulent mixing processes. It is observed that the plume development experiences turbulent convective- and diffusive-stages through a comparative study of the spatial and temporal scales of the velocity and concentration fields. It is also observed that the meandering ratio is small near the ground and within the turbulent diffusive stage, and PDFs of concentration fluctuations are sensitive to both the wall-normal distance and the downstream distance from the

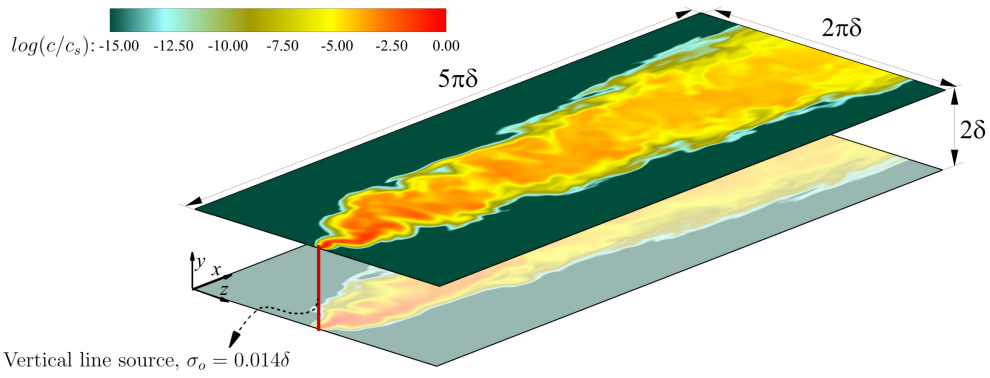

Figure 5.1: Schematic of the computational domain with the vertical line source. The source size is set to be constant in different wall normal location by the amount of $S_z = 0.014\delta$, where δ is the half of the channel height.

concentrated source.

5.2 Problem Description

This research focuses on the study of turbulent dispersion of the concentration, and the flow Reynolds number is fixed to $Re_\tau = 180$. Figure 5.1 shows a schematic diagram of the computational domain and line source position. The velocity field is assumed to fully developed such that periodical boundary conditions are applied in both streamwise and spanwise directions. No-slip and no-penetration conditions are enforced at the walls. The size of the computational domain is set to $5\pi\delta \times 2\delta \times 2\pi\delta$, where δ is the half channel height. It should be indicated that the streamwise domain size ($L_x = 5\pi\delta$) considered here is slightly longer than that ($4\pi\delta$) used in Kim *et al.* [1], who conducted DNS of a plane-channel flow at the same Reynolds number. The line source is positioned vertically in the middle of the inlet plane (at $z_s/\delta = \pi$). For the concentration field, the line source strength is kept constant, and the zero-Neumann boundary condition is imposed on the wall and over the outlet plane. As an alternative approach, a convective boundary condition can also be applied to the outlet plane. However, use a Neumann boundary condition at the outlet warrants

an instantaneous solution of positively-valued concentration ($c \geq 0$), an additional physical restriction that needs to be enforced.

The simulations were executed until statistically stationary conditions were attained for both velocity and concentration fields, after which various statistical moments were computed over a time duration of 50 large eddy turn over times (LETOT). Here, one LETOT is defined as δ/u_τ. The flow Reynolds number based on the mean centreline velocity $\langle u_c \rangle$ is $Re_c \approx 3300$. As such, the time duration of 50 LETOTs is also equivalent to $917\delta/\langle u_c \rangle$. In the well-known DNS study of a plane-channel flow conducted by Kim *et al.* [1], only 10 LETOTs were needed for calculating statistics of the velocity field. Although the Reynolds number of the background flow for driving the turbulent dispersion is the same as in Kim *et al.* [1], a much longer time duration is needed here due to the absence of streamwise and spanwise homogeneity in the concentration field.

To ensure the fine grid resolution required for performing DNS accurately, $320 \times 256 \times 300$ grid points were used in x-, y- and z- directions, respectively. The mesh is refined close to the wall and near the line source. The grid resolution in the spanwise direction changes from $\Delta z^+ = 1.15$ in the vicinity of the source to $\Delta z^+ = 4.15$ far away from the line source. The streamwise grid resolution varies from $\Delta x^+ = 0.5$ near the line source to $\Delta x^+ = 8.0$ in the far downstream region. The wall-normal grid resolution varies from $\Delta y^+ = 0.2$ in the vicinity of the wall to $\Delta y^+ = 2.51$ at the channel center. The line source size is kept constant with a diameter of $\sigma_o = 0.014\delta$. All the simulations were conducted using a 252-core server, and approximately 216,000 CPU hours were spent on solving the velocity and concentration fields and for collecting turbulence statistics.

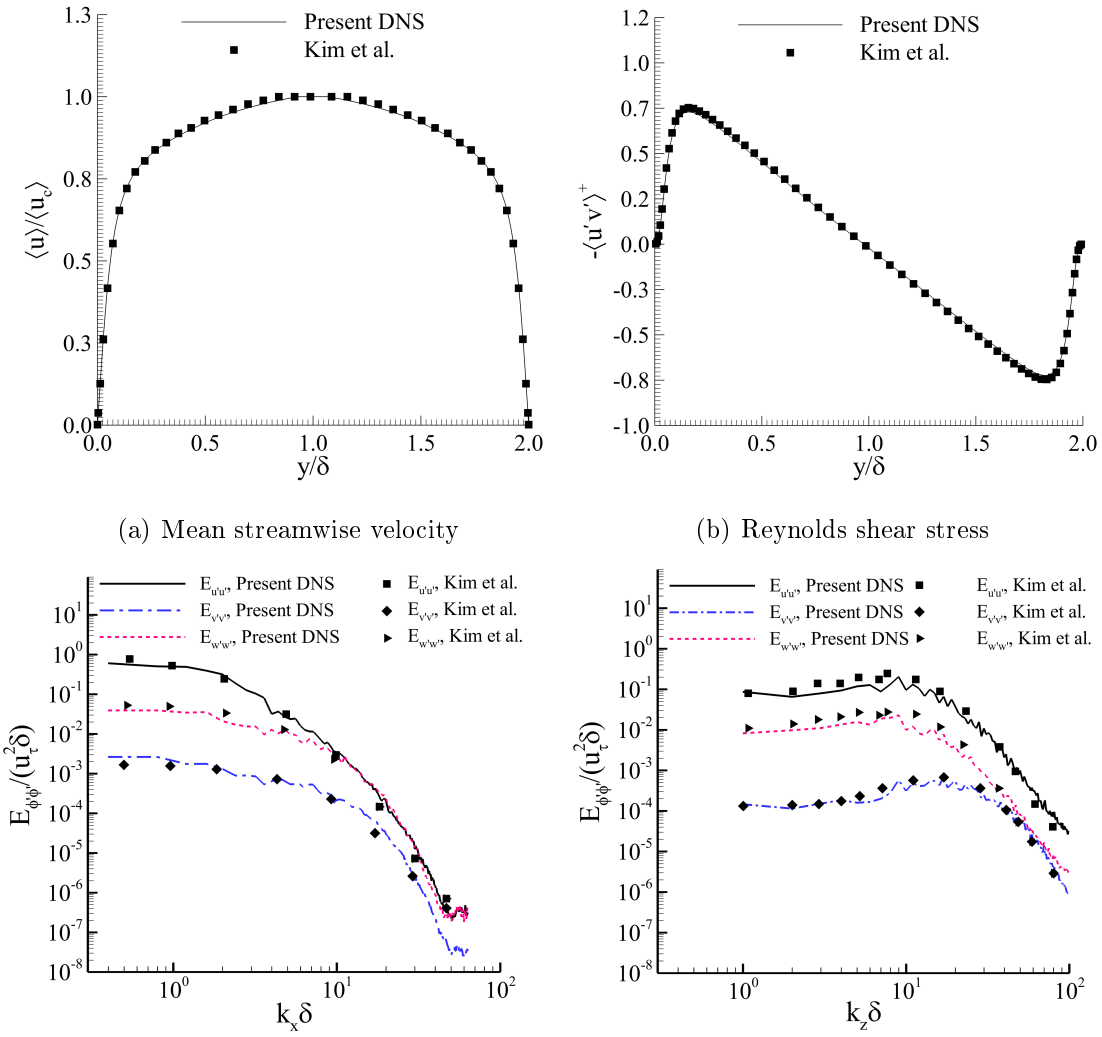

(a) Mean streamwise velocity

(b) Reynolds shear stress

(c) Spectrum of streamwise velocity fluctuations at $y^+ = 5.39$

(d) Spectrum of spanwise velocity fluctuations at $y^+ = 5.39$

Figure 5.2: Comparison of the obtained velocity statistics with the DNS data of Kim *et al.* [1].

5.3 Results

5.3.1 Velocity Field

Turbulent dispersion of a passive scalar is influenced by both small- and large-scale eddy motions. In DNS, the interest varies widely from establishing an accurate ve-

locity field that transports the scalar to the understanding of the effects of different turbulence scales on the mixing process of the scalar. Thus, it is required to briefly inspect the predictive accuracy of the velocity field prior to any thorough investigation of the statistics of the concentration field. Figures 5.2(a) and (b) compare the obtained wall-normal profiles of the mean stream velocity $\langle u \rangle / \langle u_c \rangle$ and Reynolds shear stress $-\langle u'v' \rangle^+$ against the DNS data of Kim *et al.* [1]. Here, u_c represents the streamwise velocity at the channel center. Superscript "+" indicates a variable expressed with respect to the wall coordinate, non-dimensionalized using the wall friction velocity u_τ and kinematic viscosity ν. A pair of angular brackets $\langle \cdot \rangle$ denote plane- and time-averaging for the velocity field. As is evident in Figs. 5.2(a) and (b), the agreement between the current and reported DNS data sets is excellent. To refine the examination of the velocity field, Figs. 5.2(c) and (d) further compare the obtained streamwise and spanwise energy spectra of the velocity field ($E_{u'u'}$, $E_{v'v'}$, and $E_{w'w'}$) at the wall-normal location $y^+ = 5.39$, against the available DNS data of Kim *et al.* [1], which also show a good agreement. In Figs. 5.2(c) and (d), all components of energy spectra and the wavenumbers (k_x and k_z) are non-dimensionalized using u_τ and half channel height δ. The magnitudes of $E_{u'u'}$, $E_{v'v'}$ and $E_{w'w'}$ are close to each other at high wavernumbers, which indicates a near-isotropic state of these three fluctuating components of the turbulent velocity field. However, at low wavenumbers, the differences between the three energy spectra become increasingly apparent, indicating that the turbulence field becomes increasingly anisotropic with respect to large-scale eddy motions in the near-wall region.

5.3.2 Two Stages of Concentration Plume Development: TCS and TDS

The pillar of passive plume dispersion in a TBL is the convection-diffusion mechanism [56]. This mechanism constructs two main stages of the fluctuating plume devel-

opment, namely, TCS and TDS [4; 57]. To study the transition from the TCS stage to the TDS stage of a passive plume released from a point source in a TBL, Sawford and Stapountzis [3] and Oskouie *et al.* [32] suggested comparing the characteristic length scales of the velocity and scalar fields. The current scenario of a line source vertically positioned in a TBL is different from that of a point source. Furthermore, the definitions of the TCS to TDS stages for passive plume dispersion released from a vertically positioned line source are not available in the current literature, and consequently, the transition from the TCS to the TDS stages (under a varying wall-shear strength condition) remains unclear. As one of the research objectives, we aim at proposing a method for precisely identifying the TCS and TDS stages of a passive plume emitting from a vertically positioned line source in the following context.

The study of TCS and TDS of plume development resulting from a continuous release of concentration from either a point or a line source relies on the difference between the spanwise instantaneous plume scale and the spanwise characteristic length scale of the most energetic eddies of the flow. Thus, prior to the discussion, it is beneficial to clarify several basic concepts related to plume scales such as the mean plume dispersion (σ_z), instantaneous plume centroid (σ_c), and relative plume dispersion (σ_r). We begin the discussion by examining the characteristics of the mean and instantaneous concentration fields. Figs. 5.3(a)-(d) show the contour plots and cross-stream profiles of the mean and instantaneous concentration fields, $\langle c \rangle_t$ and c, non-dimensionalized using $\langle c \rangle_{t,max}$, and c_{max}, respectively. Here, $\langle \cdot \rangle_t$ denotes time-averaging. Clearly, the mean concentration plume exhibits a Gaussian shape, a pattern that is evident in both Figs. 5.3(a) and (b). The mean plume dispersion, σ_z, is defined as [43]:

$$\sigma_z^2(x,y) = \frac{\int_0^{L_z} (z - z_s)^2 \langle c \rangle_t(x,y,z) dz}{\int_0^{L_z} \langle c \rangle_t(x,y,z) dz} \quad , \tag{5.1}$$

which represents a characteristic length scale of the mean plume width, shown schematically in Fig. 5.3(a) and (b). Given that the mean plume is Gaussian, its value peaks

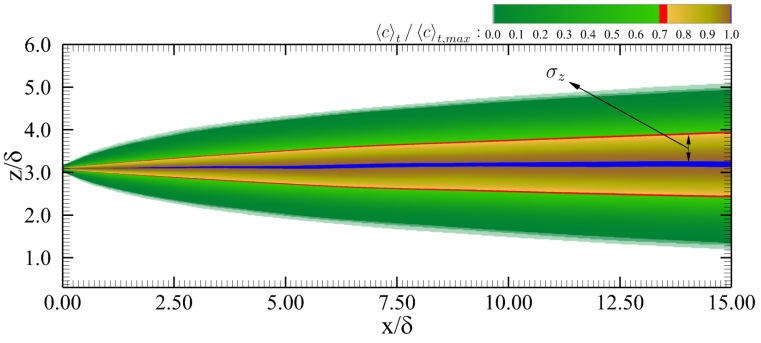

(a) Contour plot of mean concentration field $\langle c\rangle_t / \langle c\rangle_{t,max}$ at $y^+ = 180$, and illustration of σ_z

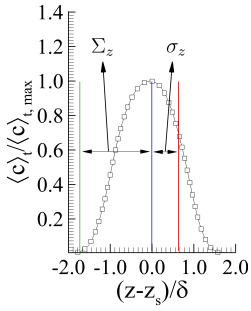

(b) Profile of the mean concentration at $x^+ = 2300$ and $y^+ = 180$

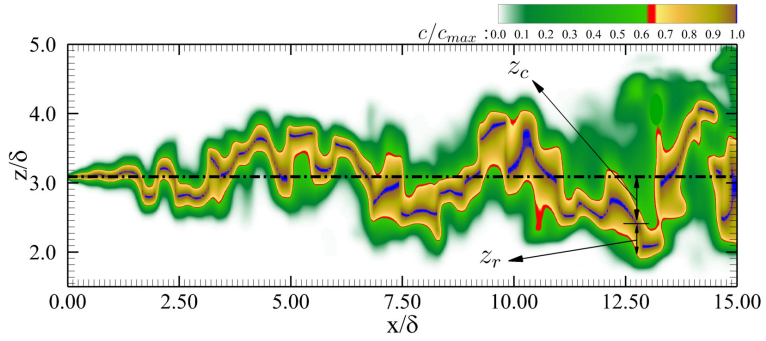

(c) Contour plot of instantaneous concentration field c/c_{max} at $y^+ = 180$, and illustration of z_c and z_r

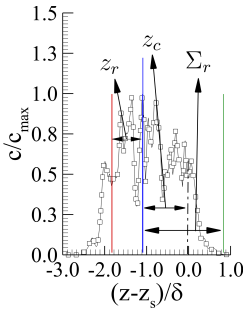

(d) Profile of the instantaneous concentration at $x^+ = 2300$ and $y^+ = 180$

Figure 5.3: Contour plots and cross-stream profiles of the mean and instantaneous concentration fields at $y^+ = 180$, and schematic of plumes scales: mean plume dispersion $\sigma_z(x, y)$, instantaneous plume centroid $z_c(x, y, t)$, instantaneous relative plume dispersion $z_r(x, y, t)$, half width of the mean plume $\Sigma_z(x, y)$, and half width of the instantaneous relative plume $\Sigma_r(x, y, t)$. The blue lines in panels (b) and (d) demarcate the centroid of the mean and instantaneous plumes, respectively.

at the central line located at $(z - z_s)/\delta = 0$. Furthermore, because the 3-D plume develops in both streamwise and wall-normal directions, $\sigma_z = f(x, y)$.

Figures 5.3(c) and (d) show the contour plot and profile of the instantaneous concentration field at the same position as in Figs. 5.3(a) and (b), respectively. From Fig. 5.3(c), it is clear that the instantaneous centroid z_c of the plume fluctuates and can deviate from the spanwise source position z_s, which can be calculated as

$$z_c(x,y,t) = \frac{\int_0^{L_z} zc(x,y,z,t)dz}{\int_0^{L_z} c(x,y,z,t)dz} - z_s \quad . \tag{5.2}$$

The concept of the instantaneous centroid z_c is demonstrated in Figs. 5.3(c) and (d), measured with a reference to the spanwise source position (i.e., $(z - z_s)/\delta = 0$). Once the time series of z_c become available, the dispersion of the centroid of the instantaneous plume can be determined, which is $\sigma_c(x,y) = \langle |z_c(x,y,t)| \rangle_t$.

There are two underlying physical mechanisms that contribute to the growth of a mean plume: the dispersion of the centroid of the instantaneous plume ($\sigma_c(x,y)$) related to the bulk meandering of the plume, and the relative dispersion ($\sigma_r(x,y)$) with respect to the centroid of the instantaneous plume related to internal fluctuations within the plume. These two different mechanisms of (external mixing due to flow convection and internal in-plume mixing due to relative dispersion) can be effectively quantified by the so-called meandering ratio, defined as $M = \sigma_c^2/\sigma_r^2$. The instantaneous relative plume dispersion $z_r(x,y,t)$ with respect to the instantaneous plume centroid $z_c(x,y,t)$ is shown schematically in Fig. 5.3(d). Calculation of the value of the relative plume dispersion σ_r can be a complicated task simply because the instantaneous plume is typically non-Gaussian [31]. This is evident in Fig. 5.3(d), which shows the instantaneous concentration field at $x^+ = 2300$ and $y^+ = 180$. The value of σ_r is related to the values of σ_z and σ_c as [3; 32]:

$$\sigma_z^2 = \sigma_c^2 + \sigma_r^2 \quad . \tag{5.3}$$

As such, once the values of σ_z and σ_c are known, that of σ_r can be determined. The half widths of the mean plume and instantaneous relative plumes are denoted as Σ_z and Σ_r, respectively, in Fig. 5.3. If the mean and instantaneous plumes exhibit a Gaussian distribution, the following identities hold: $\Sigma_z = 3\sigma_z$ and $\Sigma_r = 3\sigma_r$.

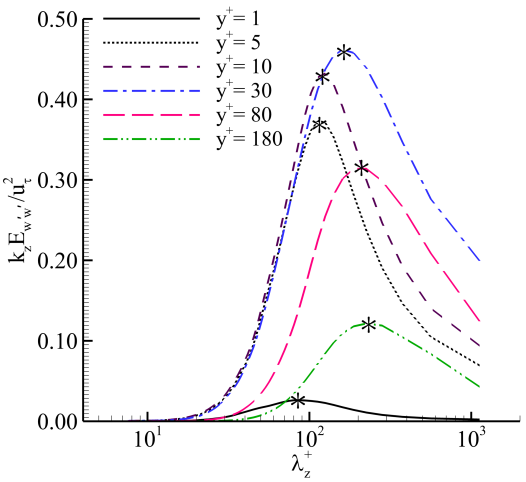

Figure 5.4: Pre-multiplied energy spectra of spanwise velocity fluctuations at six different elevations. The asterisk symbol labels the mode of a pre-multiplied spectrum.

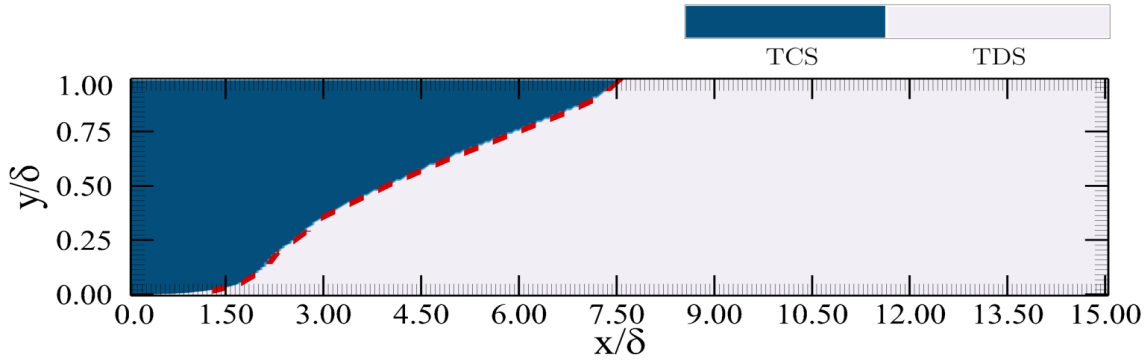

Figure 5.5: Continuous transition from TCS to TDS in the streamwise and wall-normal directions.

In a turbulent channel flow, the flow is bounded by the upper and lower walls. The spanwise turbulence length scale of the velocity field is characterized by the separation of streamwise-elongated streaks, which represent the energetic flow structures in near-wall turbulence [58]. The spanwise characteristic length scale of the dominant streaky flow structures ($\lambda_{z,m}(y)$) can be determined from the premultiplied spectrum ($k_z E_{w'w'}(k_z, y)$) of velocity fluctuations. Here, λ_z represents the spanwise wavelength, additional subscript 'm' denotes mode (corresponding to the peak of the premulti-

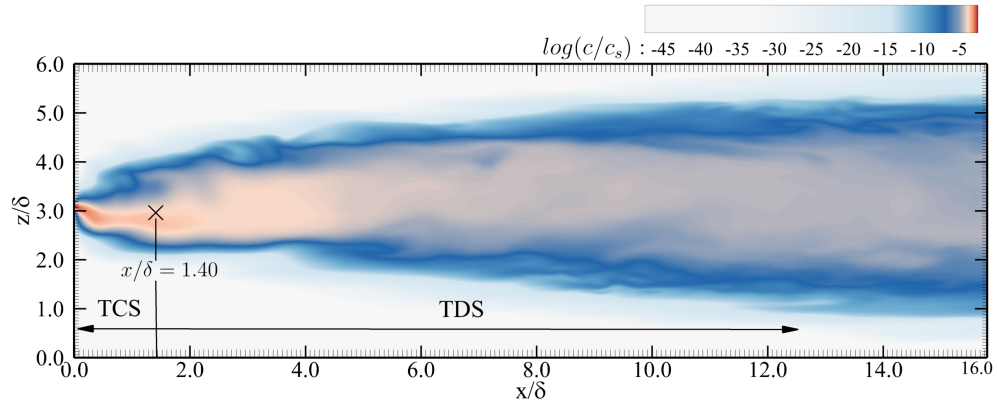

(a) $y^+ = 5$

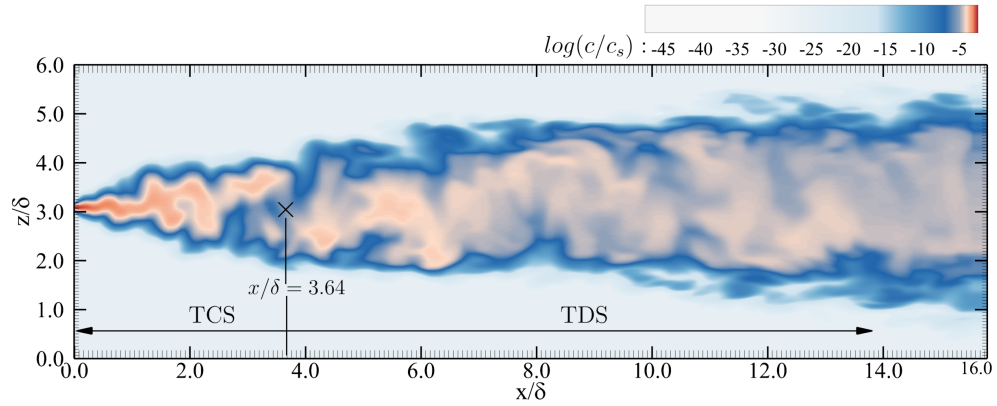

(b) $y^+ = 120$

Figure 5.6: Comparison of the instantaneous concentration field c extracted at two wall-normal locations for $y^+ = 5$ and 120. The cross symbol '$\times$' demarcates the streamwise position where the transition from TCS to TDS occurs.

plied spectrum), and k_z represents the spanwise wavenumber (with $\lambda_z = 2\pi/k_z$). The spanwise energy spectrum is calculated as $E_{w'w'}(k_z) = \frac{1}{\pi}\int_{-\infty}^{+\infty} e^{-ik_z r} R_{w'w'}(r)dr$, where $R_{w'w'}(r) = \langle w'(z)w'(z+r)\rangle / w_{rms}^2$ is the autocorrelation function of the spanwise velocity fluctuations. Near the line source, the plume size is smaller than that of the energetic eddies (i.e., $2\Sigma_r < \lambda_{z,m}$), and so, the plume meanders with the large-eddy motions. As such, the concentration plume features an external mixing process dominated by turbulent flow convection mechanism, and this phase of plume

development is referred to as TCS. Further downstream of the source, the plume size grows. Once the instantaneous plume size exceeds that of the most energetic eddies (i.e., $2\Sigma_r \geq \lambda_{z,m}$), the mixing process transitions from TCS to TDS. In TDS, the characteristic length scale of the energetic eddy motions ($\lambda_{z,m}$) is smaller than the plume size such that they contribute to in-plume mixing, featuring turbulent diffusion. Consider Eq. (5.3), the critical condition for transition from TCS to TDS can be further expressed as

$$6\sigma_r(x,y) = (6\sigma_z/\sqrt{1+M}) \geq \lambda_{z,m}(y) \quad . \tag{5.4}$$

Figure 5.4 shows the premultiplied energy spectra of spanwise velocity fluctuations at six different wall-normal positions. In the figure, an asterisk is used to demarcate the mode of a premultiplied spectrum. The spanwise characteristic length scale of energetic turbulence eddies is $\lambda^+_{z,m}|_{y^+=1} \approx 86$, $\lambda^+_{z,m}|_{y^+=5} \approx 116$, $\lambda^+_{z,m}|_{y^+=10} \approx 124$, $\lambda^+_{z,m}|_{y^+=30} \approx 163$, $\lambda^+_{z,m}|_{y^+=80} \approx 195$, and $\lambda^+_{z,m}|_{y^+=180} \approx 219$. Clearly, as the wall-normal distance (or, the y^+ value) increases, the characteristic length scale of energetic eddy motions (as indicated by the value of $\lambda^+_{z,m}$) increases monotonically. Previous studies [3; 32; 33; 23] of the transition from TCS to TDS have focused on either point or horizontal line source dispersion at a fixed wall-normal distance or simply in homogeneous isotropic turbulence [28, 17]. In contrast to the previous approaches, here, we refine the research by investigating how the transition from TCS to TDS occurs continuously along the line source in the wall-normal direction. More specifically, we are interested in finding out the wall-anisotropic effect on this transition, as the characteristic length scale of turbulent eddy motions increases monotonically and continuously as the wall coordinate y^+ increases.

Based on the criterion given by Eq. (5.4), the two regimes (TCS and TDS) associated with the plume development are shown in Fig. 5.5. From the figure, it is apparent that the transition from TCS to TDS is continuous with respect to the wall-normal distance y^+. Furthermore, the transition process becomes more rapid as

the wall is approached. This physical phenomenon can be explained from the varying trends of the characteristic length scale of energetic eddies $\lambda^+_{z,m}$ and mean plume width σ_z with respect to the wall-normal distance y^+. From the previous analysis of Fig. 5.4, it is understood that the value of $\lambda^+_{z,m}$ decreases monotonically as the wall is approached. Furthermore, the mean plume width σ_z becomes greater as the wall is approached. Both factors contribute to the fast transition from TCS to TDS in the near-wall region, a conclusion that is straightforward from Eq. (5.4). To demonstrate the effect of wall-normal distance on the instantaneous plume dispersion pattern and the transition from TCS to TDS, the contour plots of the instantaneous concentration fields at $y^+ = 5$ and 120 are compared in Fig. 5.6. From Fig. 5.6(a), it is seen that at $y^+ = 5$, the plume transitions from TCS to TDS soon after its release, and clearly, its streamwise development is dominated by the diffusion mechanism (see also Fig. 5.5). In TDS, the characteristic length scale of the energetic eddies is smaller than that of the instantaneous plume width, and the turbulent eddy motions contribute to the in-plume mixing of the concentration. As the wall-normal distance increases from $y^+ = 5$ to 120, the transition point from TCS to TDS extends from $x/\delta \approx 1.4$ to 3.64. At the higher elevation of $y^+ = 120$, the meandering pattern of the plume within the TCS (i.e., $0 \leqslant x/\delta < 3.64$) is apparent. The concentration patches are carried around by large-scale energetic eddies, contributing to the external mixing process of the concentration.

To refine the analysis, the growth rates of the mean plume width σ_z along the streamwise and vertical directions are demonstrated in Figs. 5.7(a) and (b), respectively. Clearly, the mean plume width σ_z increases monotonically along the streamwise direction at all elevations, and furthermore, the value of σ_z increases monotonically as the wall is approached. From Fig. 5.7(b), it is also seen that the wall-normal variation of σ_z becomes less sensitive as the distance downstream of the line source (x/δ) increases. The pattern of transition from TCS to TDS and the monotonic trends of $\lambda^+_{z,m}$ and σ_z with respect to y^+ all relate to the fact that as the wall is ap-

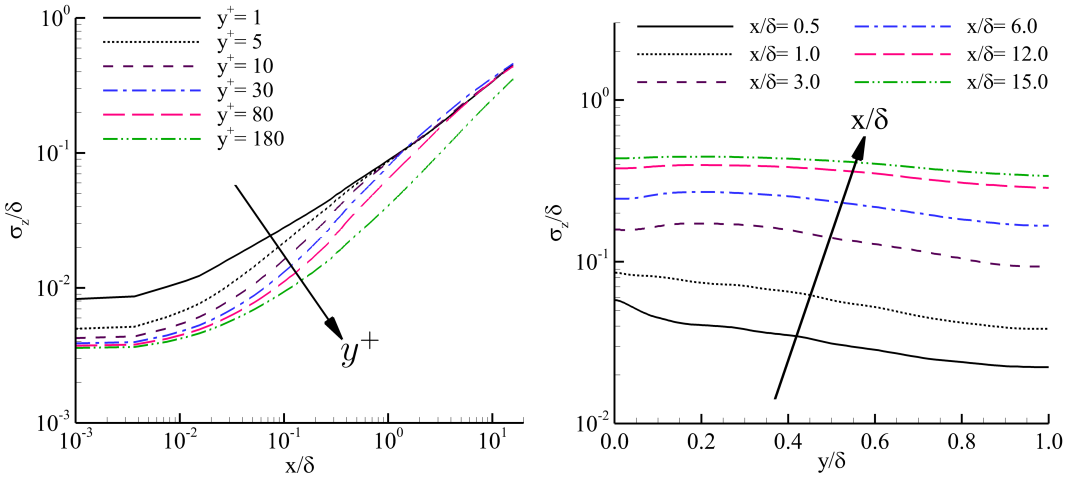

(a) Streamwise development (b) Vertical development

Figure 5.7: Streamwise and vertical development of the mean plume widthσ_z.

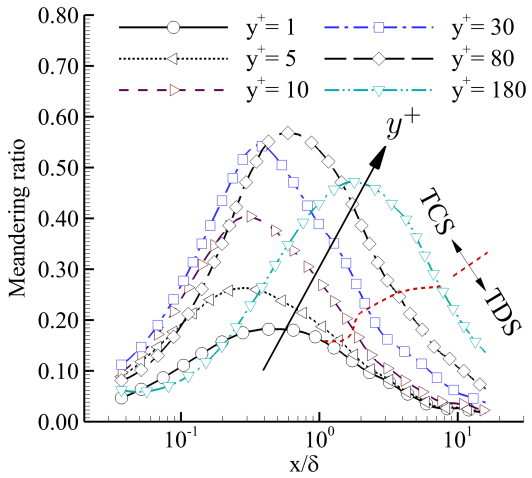

Figure 5.8: Streamwise development of the meandering ratio M at six different wall-normal positions. The red dashed curve separates TCS and TDS regions.

proached, the transport processes of both momentum and scalar become increasingly dominated by the diffusion mechanism and less dominated by the convection mechanism. Figure 5.8 compares the streamwise profiles of the meandering ratio M at six

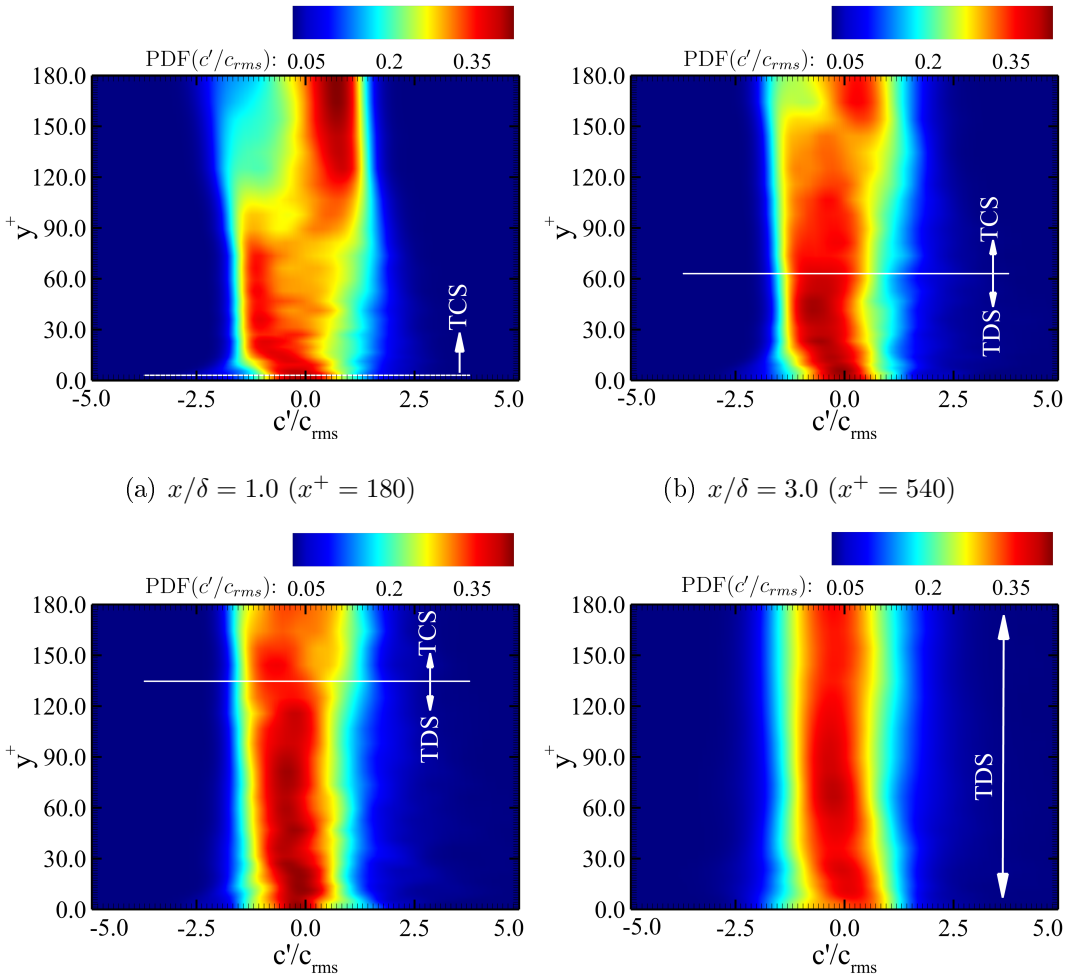

(a) $x/\delta = 1.0$ ($x^+ = 180$)

(b) $x/\delta = 3.0$ ($x^+ = 540$)

(c) $x/\delta = 6.0$ ($x^+ = 1080$)

(d) $x/\delta = 12.0$ ($x^+ = 2160$)

Figure 5.9: Streamwise evolution of the vertical distribution of the PDFs of concentration fluctuations c' (non-dimensionalized by c_{rms}). The transition from TCS to TDS occurs at $y/\delta = 0.1$, 0.35 and 0.75 (correspondingly, at $y^+ = 1.8$, 63.0 and 135.0) at $x/\delta = 1.0$, 3.0 and 6.0, in panels (a), (b) and (c), respectively. In panel (d), the plume development is dominated exclusively by TDS.

different wall-normal positions for $y^+ = 1$, 5, 10, 30, 80, and 180 as in Fig. 5.7(a). From Fig. 5.8, it is clear that in the region near the source (where the value of x/δ is relatively small), the pattern of plume dispersion is predominantly TCS. This is because the plume size is much smaller than that of the energetic eddies in the re-

gion immediately downstream of the source, and consequently, the mixing process of the concentration is dominated by the large flapping eddy motions of the fluid flow. In other words, the relatively small-sized concentration patches are carried around by large-scale energetic eddy motions in the region immediately downstream of the source. However, as the downstream distance from the source increases (or, as the value of x/δ increases), the plume size grows and eventually exceeds that of large energetic eddies. Consequently, the motion of energetic eddies acts as in-plume mixing, enhancing turbulent diffusion of the concentration and the pattern of plume dispersion transitions from TCS to TDS at all six elevations. Furthermore, as the downstream distance from the line source continues to increase in the far downstream region (in the TDS region), the value of M continues to decrease, indicating an enhanced turbulent diffusion and in-plume mixing mechanism by large energetic eddies. Consistent with Fig. 5.5, it is seen that the streamwise position (x/δ) for the transition to occur from TCS to TDS becomes increasingly delayed as the wall-normal distance increases (as the value of y^+ increases). Also, the value of the meandering ratio M at the transition point also increases monotonically as the value of y^+ increases. This is because as the wall-normal distance increases, the strength of turbulent convection enhances, and consequently, the dispersion of the plume centroid increases monotonically.

Figure 5.9 shows the contour plots of probability density function (PDF) of concentration fluctuations at four different streamwise locations ($x/\delta = 1, 3, 6$, and 12). The transition from TCS to TDS is labeled using a white line in Figs. 5.9(a)-(c). However, in the far downstream region at $x/\delta = 12$ as shown in Fig. 5.9(d), the plume development is entirely dominated by TDS. From Fig. 5.5, it is known that the transition from TCS to TDS occurs at $(x/\delta, y/\delta) = (1.0, 0.01)$, $(3.0, 0.35)$, and $(6.0, 0.75)$. Correspondingly, the transition occurs at $(x^+, y^+) = (180, 1.8)$, (540, 63), and (1080, 135) with respect to wall units in Figs. 5.9(a), (b) and (c), respectively. The PDF contour pattern is different between TCS and TDS. This can be understood by comparing Fig. 5.9(a) with 5.9(d). The PDF contour pattern in the TCS zone

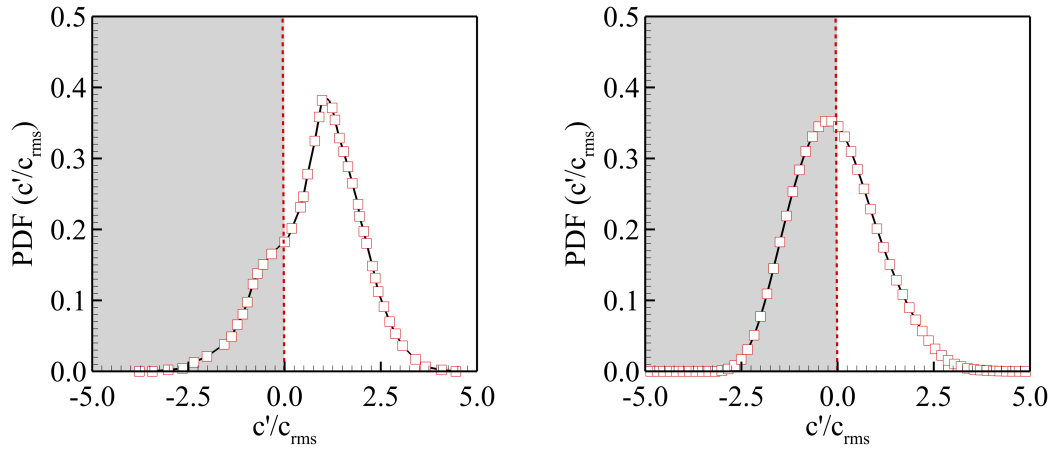

(a) $x/\delta = 1.0$ ($x^+ = 180$) and $y^+ = 170$ (b) $x/\delta = 12.0$ ($x^+ = 2160$) and $y^+ = 170$

Figure 5.10: PDFs of concentration fluctuations c' (non-dimensionalized by c_{rms}) within a (a) TCS zone, and a (b) TDS zone.

shown in Fig. 5.9(a) is apparently asymmetrical, while that in the TDS zone shown in Fig. 5.9 is symmetrical in general. To refine the study, two typical PDF profiles of TCS and TDS are compared in Fig. 5.10. Clearly, the PDF profile is asymmetrical, deviating significantly from a Gaussian distribution in the TCS of plume development. By contrast, the PDF profile exhibits a quasi symmetrical Gaussian distribution in the TDS of plume development. The reason for the PDF to be nearly Gaussian in a TDS zone is that the length scale of large eddies is smaller than that of the plume, and therefore, the flapping motion of large eddies contribute to the in-plume mixing of concentration. The flapping motions of eddies around the plume centroid result in equal chances of positive and negative concentration fluctuations in a TDS zone, leading to a Gaussian distribution of c'.

5.3.3 Concentration Statistics

Figure 5.11 compares the spanwise profiles of the mean concentration $\langle c \rangle_t$ (non-dimensionalized by the source strength c_s) at four streamwise positions (for $x/\delta = 1.0$,

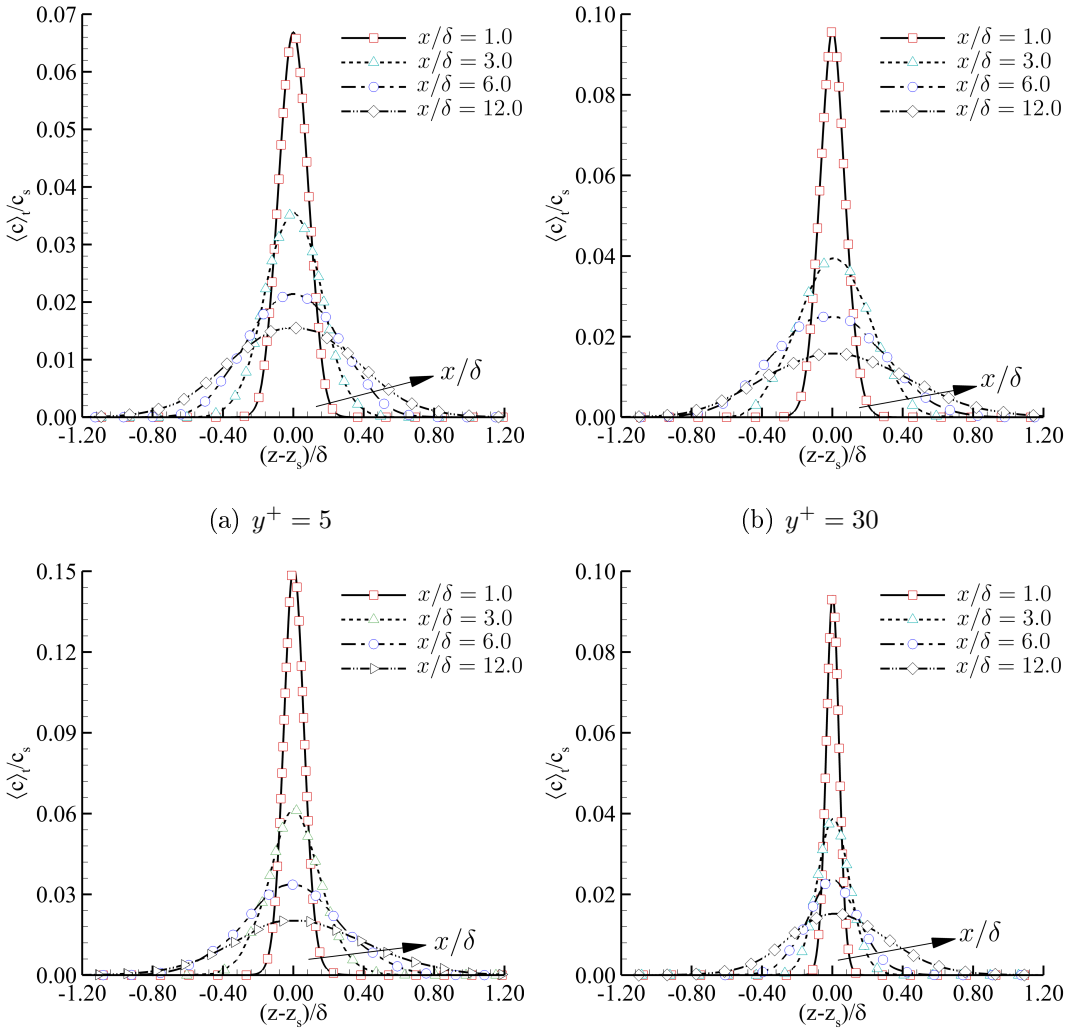

(a) $y^+ = 5$ (b) $y^+ = 30$

(c) $y^+ = 80$ (d) $y^+ = 180$

Figure 5.11: Streamwise development of the mean concentration at various wall-normal positions. Arrow in panels (a-d) points to the direction of an increasing x/δ value.

3.0, 6.0 and 12.0) at four different elevations (for $y^+ = 5$, 30, 80 and 180). Clearly, the mean concentration profiles exhibit a Gaussian distribution at all positions. As the streamwise distance from the source increases from $x/\delta = 1.0$ to 12.0, the mean plume spread becomes increasingly wider and the peak value of $\langle c \rangle_t / c_s$ decreases

monotonically. Furthermore, by comparing Figs. 5.11(a)-(d), it is seen that the mean plume spread becomes increasingly narrower as the wall-normal distance increases from $y^+ = 5$ to 180. The physical mechanism underlying this trend is that as the distance from the wall increases, the streamwise mean flow velocity becomes higher, and so, the concentration emitted from the source can be carried downstream more rapidly. This inevitably makes the spanwise spread of the mean plume narrower. It is interesting to note that the area underneath each curve of the non-dimensionalized mean concentration shown in Fig. 5.11 is the non-dimenensionalized source size, i.e. $\sigma_o/\delta = 0.014$. In fact, for a steady-state line source emission problem, the dosage of the concentration at an arbitrary wall-normal distance is

$$D = \int_0^{L_z} \langle c \rangle_t(x, y, z) dz = \sigma_o c_s \quad , \tag{5.5}$$

from which it is straightforward that $\int_0^{L_z} \langle c \rangle_t / c_s \; dz = \sigma_o$.

Figure 5.12 compares four spanwise profiles of the mean concentration (non-dimensionalized by the local maximum mean concentration value, $\langle c \rangle_{t,max}$) at three elevations (for $y^+ = 5$, 30 and 180). The profiles are exhibited with respect to a lateral coordinate defined as

$$\zeta = \frac{z - z_s}{z_{1/2} - z_s} \quad , \tag{5.6}$$

where $z_{1/2}$ corresponds to the lateral location when $\langle c \rangle_t$ drops to one half of its local maximum $\langle c \rangle_{t,max}$. The choice of this special lateral coordinate ζ is inspired by the well-known similarity theory for a plane slot jet [see, e.g. 55; 15]. From Fig. 5.1, it is understood that a line source emission problem is similar to a slot jet problem in terms of the geometrical setup of the domain. Of course, there is a significant difference between these two scenarios of emitted momentum of a slot jet flow and emitted passive concentration, which are governed by Eqs. (2.2) and (2.3), respectively. However, if the mean streamwise velocity of the flow emitted from a slot jet exhibits a self-similarity, there is a good possibility for the mean concentration field emitted from the line source to also exhibit a self-similarity if scaled properly.

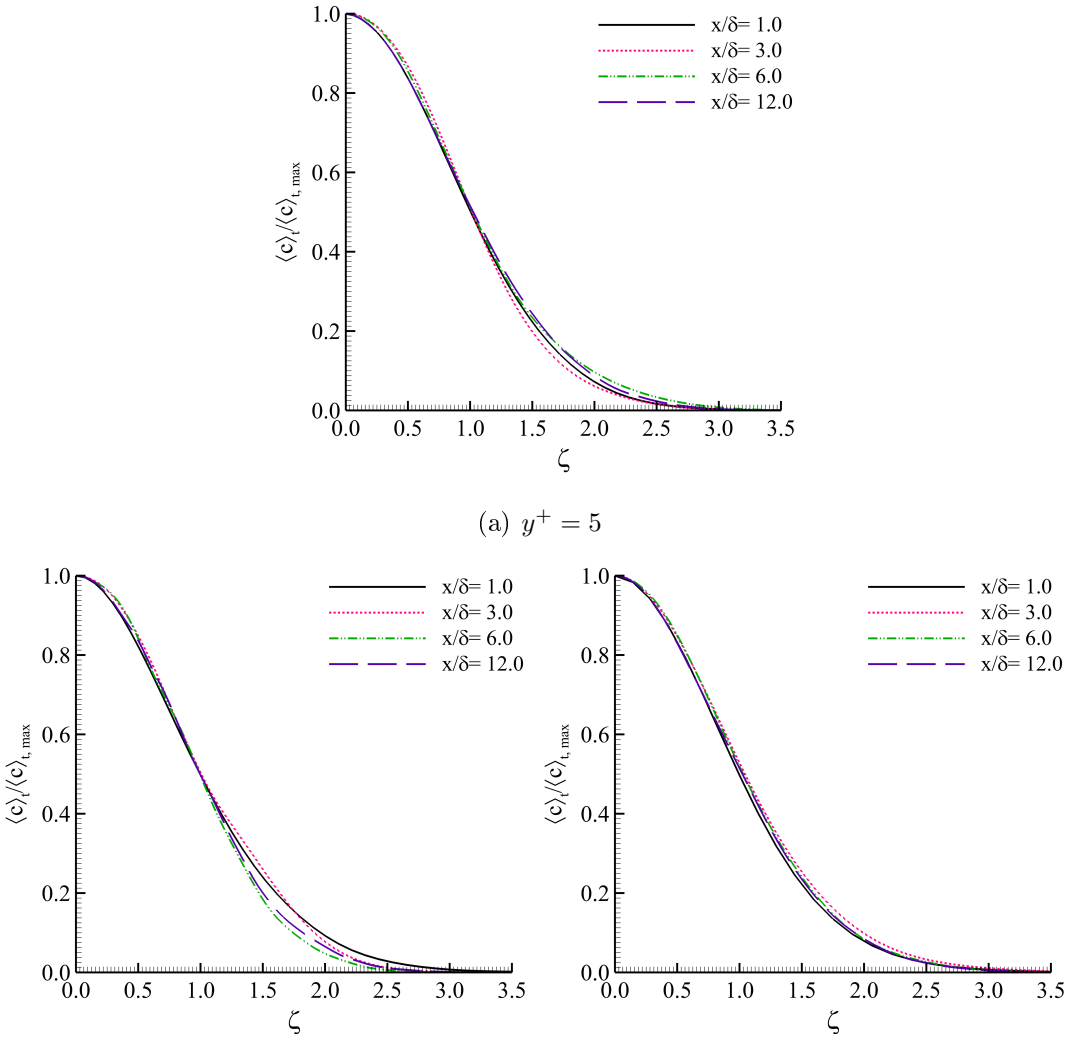

(a) $y^+ = 5$

(b) $y^+ = 30$

(c) $y^+ = 180$

Figure 5.12: The first moment of the concentration field in the self-similar manner.

This is an interesting conjecture, especially under the current testing condition of a vertically positioned line source between two parallel walls. From Fig. 5.12, it is exciting to observe that a general self-similarity of the non-dimensionalized mean concentration field is indeed present. It is clear that the profiles of $\langle c \rangle_t / \langle c \rangle_{t,max}$ at the four different streamwise positions well collapse in the viscous sublayer (for $y^+ = 5$)

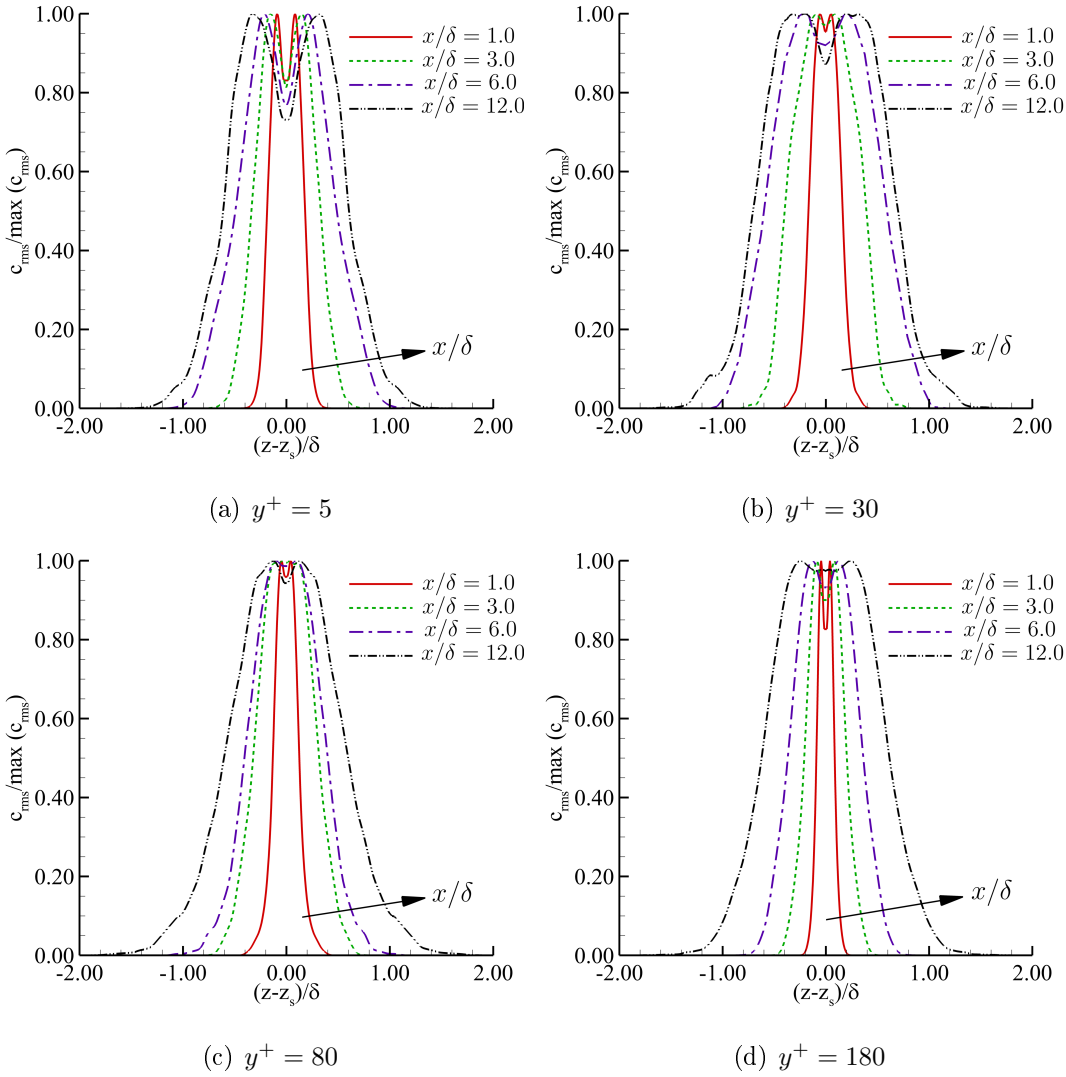

(a) $y^+ = 5$ (b) $y^+ = 30$

(c) $y^+ = 80$ (d) $y^+ = 180$

Figure 5.13: Comparison of the spanwise profiles of the RMS concentration at four different streamwise and four different wall-normal positions. The RMS concentration value c_{rms} has been non-dimensionalized using its local maximum value, $\max(c_{rms})$.

and in the overlap layer (at the channel center for $y^+ = 180$); while very small discrepancies are observed between the profiles in the buffer layer (for $y^+ = 30$).

Figure 5.13 compares the spanwise profiles of the root-mean-square (RMS) of the concentration field c_{rms} at four streamwise positions (for $x/\delta = 1.0$, 3.0, 6.0 and 12.0) at four different elevations (for $y^+ = 5$, 30, 80 and 180). The RMS concentration has

been non-dimensionalized by its maximum value such that the monotonic trend of the streamwise evolution of its profile can be clearly demonstrated. From Fig. 5.13, it is clear that the profile becomes wider as the downstream distance increases from $x/\delta = 1.0$ to 12.0. Furthermore, there is a consistent dual-peak pattern appearing in the profile of c_{rms}. The physical mechanism underlying these phenomena is simply that at a fixed elevation (for $y^+ = 5$, 30, 80, or 180), the lateral plume spread grows in the downstream direction (see also Figs. 5.3, 5.6 and 5.11). At both interfaces of the plume envelope, the mean concentration gradient ($\partial\langle c\rangle/\partial z$) is the largest, which contributes significantly to the production rate (defined as $-2\langle u_i' c'\rangle \cdot \partial\langle c\rangle/\partial x_i$) of the concentration variance $\langle c'^2\rangle$. This inevitably results in the dual peaks at both plume interfaces. This mechanism of the dual-peak pattern of c_{rms} of a line source is similar to that of a point source as detailed in the DNS studies of [32; 17].

5.3.4 Temporal Characteristics of the Plume

Thus far, our discussion of the transition from TCS to TDS has been strictly based on the spatial scales of the plume, and the criterion is given by Eq. (5.4), i.e. $6\sigma_r(x,y) = (6\sigma_z/\sqrt{1+M}) \geqslant \lambda_{z,m}(y)$. The transition from TCS to TDS is also profoundly reflected in the temporal characteristics of the turbulent velocity and passive scalar fields. Specifically, the transition process can be also investigated based on the characteristic time scales of the spanwise velocity fluctuations $T^+_{w',m}$, and concentration fluctuations $T^+_{c',m}$. Here, $T^+_m = u_\tau/(f_m\delta)$ is the time scale, subscript 'm' denotes 'temporal mode', and f_m denotes the characteristic frequency (corresponding to the mode). From Cassiani *et al.* [59; 60], the region associated with TDS features $T^+_{c',m} \geqslant T^+_{w',m}$. In other words, the spatial scales and temporal scales of turbulence are closely coupled. In the TDS region, the spatial characteristic length scale of large energetic eddies is smaller than that of the plume. Correspondingly, the temporal scale of concentration fluctuations is larger than that of turbulence eddies (as indicated by spanwise velocity fluctuations). These two characteristic temporal scales are

determined by the modes of the premultiplied spectra of the spanwise velocity fluctuations w' and concentration fluctuations c'. The spectrum of the fluctuations of a turbulence variable ψ can be calculated through the following fast Fourier transform (FFT) as

$$\tilde{E}_{\psi'\psi'}(f) = \frac{1}{\pi}\int_{-\infty}^{+\infty} e^{-i\pi 2f\tau}\tilde{R}_{\psi'\psi'}(\tau)d\tau \quad , \tag{5.7}$$

where f is the frequency, $\tilde{R}_{\psi'\psi'}(\tau)$ is the autocorrelation function of the fluctuations (ψ'), and tilde symbol $(\tilde{\cdot})$ denotes temporal FFT. The premultiplied spectrum $f\tilde{E}(f)$ becomes trivial at either very low or very high frequencies, i.e. $f\tilde{E}_{\psi'\psi'}(f) \to 0.0$ if $f \to 0.0$ or $f \to \infty$ [61; 62]. This is because the turbulence energy is primarily contributed and dominated by the most energetic eddies motions, which possess the characteristic (or modal) frequency f_m of the premultiplied spectrum $f\tilde{E}(f)$. Thus, the turbulence energy contained by either extremely small or extremely large frequencies at the two ends of the premultiplied spectrum is trivial. Given that the velocity field is statistically homogeneous in the x-z plane, the characteristic time scale associated with the large energetic eddy motions of the fluid flow depends on the wall-normal distance y^+ only, i.e., $T^+_{w',m} = f(y^+)$. However, because the plume develops in all three directions, the characteristic time scale $T^+_{c',m}$ of the concentration field varies in both the streamwise and wall-normal directions, such that $T^+_{c',m} = f(x^+, y^+)$. At a given wall-normal position y^+, if $T^+_{w',m} > T^+_{c',m}$, dispersion of the plume is dominated by the turbulent convection mechanism, and consequently, the plume development is in a TCS zone; however, if $T^+_{w',m} < T^+_{c',m}$, the dispersion process is dominated by the turbulent diffusion mechanism and the plume development is in a TDS region.

Figure 5.14 compares the premultiplied temporal spectra of the spanwise velocity and concentration fluctuations at two wall-normal positions (for $y^+ = 5$ and $y^+ = 180$). In Fig. 5.14, the frequency has been non-dimensionalized and is represented by the Strouhal number, defined as $f^* = f\delta/u_\tau$. In the calculation of the temporal scales associated with the premultiplied spectra, the turbulence signals were sampled where the strength of concentration fluctuations or the value of c_{rms} is the maximum

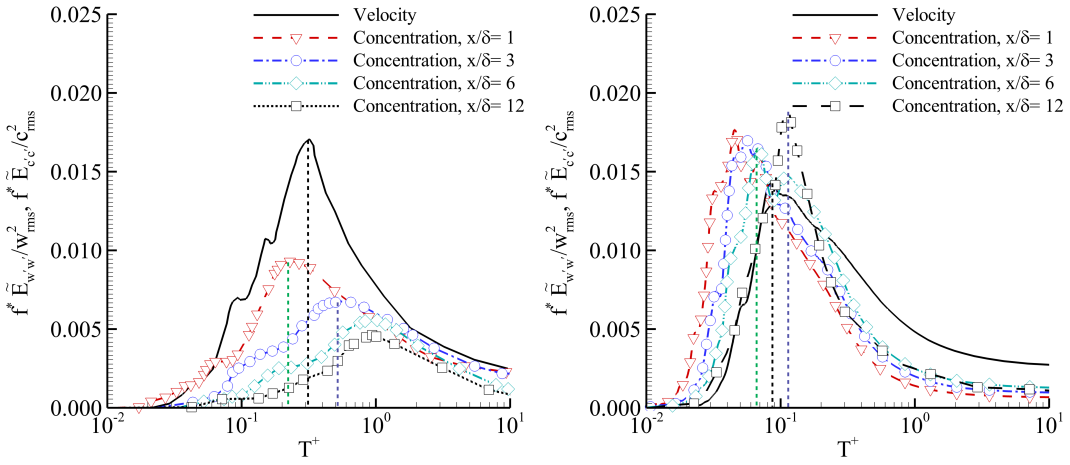

(a) $y^+ = 5$ (b) $y^+ = 180$

Figure 5.14: Comparison of premultiplied temporal spectra of the spanwise velocity and concentration fluctuations at different streamwise locations at two fixed elevations of $y^+ = 5$ and 180.

(see Fig. 5.13). From Figs. 5.14(a) and (b), it is evident that the modal value ($T^+_{c',m}$) of the premultiplied spectra of concentration fluctuations increases monotonically as the downstream distance increases from $x/\delta = 1.0$ to 12, at both elevations of $y^+ = 5$ and 180. Figure 5.14(a) compares the premultiplied spectra of the velocity and concentration fluctuations at $y^+ = 5$. From Fig. 5.14(a), it is seen that the mode of the premultiplied spectra of velocity fluctuations is located in between the modes of the premultiplied spectra of concentration fluctuations at $x/\delta = 1.0$ and 3.0, i.e. $T^+_{c',m}|_{x/\delta=1.0} < T^+_{w',m} < T^+_{c',m}|_{x/\delta=3.0}$. This indicates that the transition from TCS to TDS occurs within the streamwise range of $1.0 < x/\delta < 3.0$ at $y^+ = 5$. This conclusion is obtained based on an analysis of the temporal spectra of velocity and concentration fluctuations, which is fully consistent with the previous conclusion of $x/\delta = 1.4$ based on a direct analysis of spatial scales through Figs. 5.5 and 5.8. Similarly, at $y^+ = 180$ as shown in Fig. 5.14(b), it is observed that $T^+_{c',m}|_{x/\delta=6.0} < T^+_{w',m} < T^+_{c',m}|_{x/\delta=12.0}$. Therefore, based on the analysis of the premultiplied temporal spectra, it is understood that the transition from TCS to TDS occurs within the

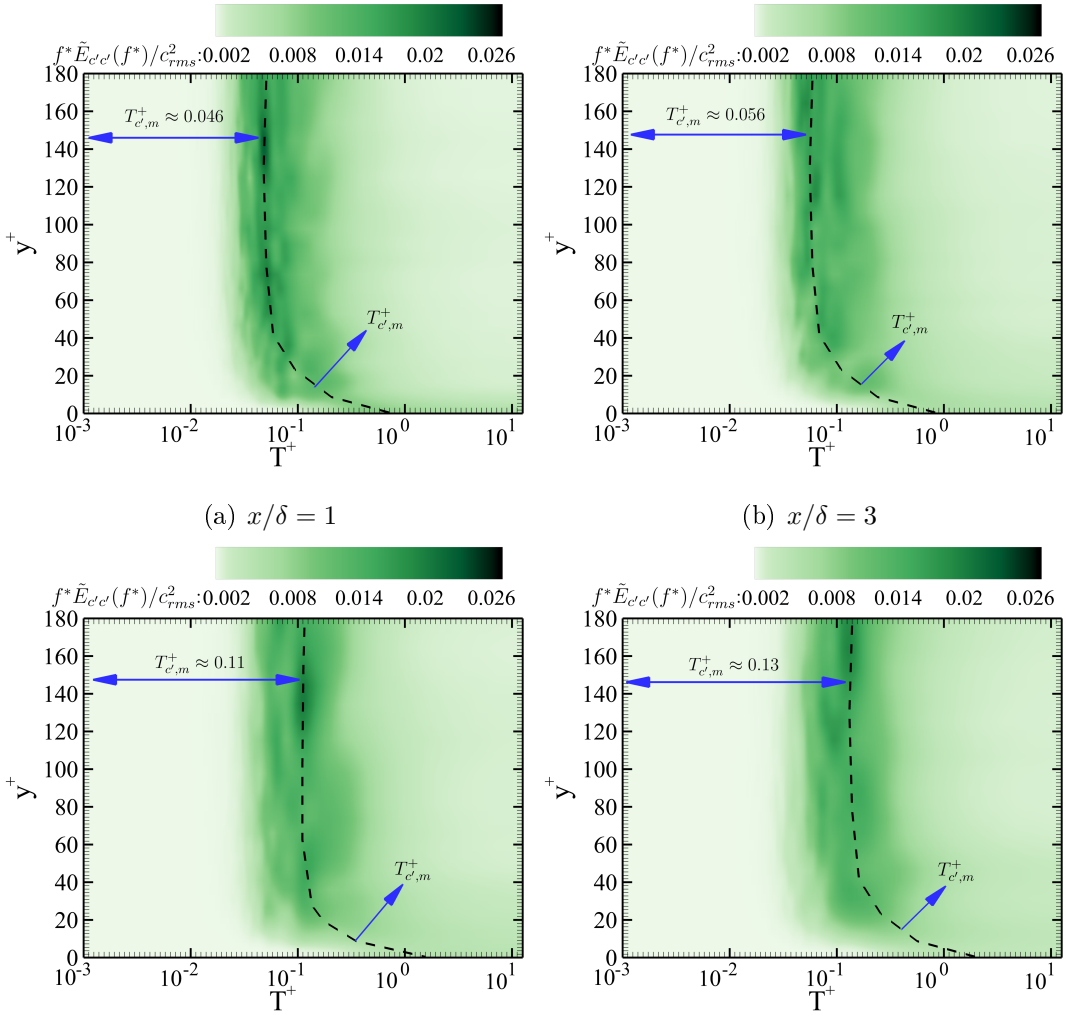

Figure 5.15: Contour plots of non-dimensionalized premultiplied temporal spectrum of concentration fluctuations at four streamwise locations for $x/\delta = 1$, 3, 6 and 12.

streamwise range of $6.0 < x/\delta < 12.0$ at $y^+ = 180$. In fact, from Figs. 5.5 and 5.8, it is known that the transition occurs at $x/\delta = 7.5$ exactly. Clearly, as the elevation increases from $y^+ = 5$ to 180, the transition point becomes postponed. The diagnosis of the transition point is fully consistent between the two approaches of spatial and temporal analyses, and the monotonic trend of the transition curve with y^+ was given

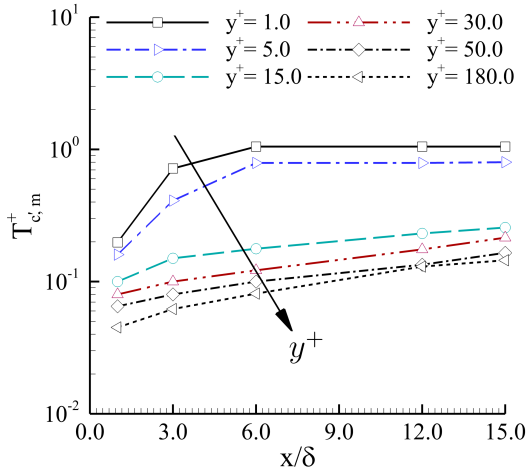

Figure 5.16: Profiles of $T^+_{c',m}$ as a function of the downstream distance from the line source (x/δ).

precisely in a continuous form in the physical space in Figs. 5.5 and 5.8.

In Fig. 5.14, the characteristic temporal scale ($T^+_{c',m}$) associated with the non-dimensionalized premultiplied spectrum of concentration fluctuations ($f^*\tilde{E}_{c'c'}/c^2_{rms}$) was studied at two particular wall-normal positions for $y^+ = 5$ and 180. In order to develop a general understanding of the variation of the characteristic temporal scale $T^+_{c',m}$ with respect to the wall coordinate y^+, the contours of $f^*\tilde{E}_{c'c'}/c^2_{rms}$ are displayed continuously in Fig. 5.15 at four streamwise locations. In Fig. 5.15, the black dashed curve corresponds to mode of $f^*\tilde{E}_{c'c'}/c^2_{rms}$ (i.e., $T^+_{c',m}$). Clearly, the temporal characteristic scale $T^+_{c',m}$ is the maximum at the wall and reduces to a stable value once the distance from the wall increases beyond $y^+ > 40$. By comparing Figs. 5.15(a)-(d), it is observed that as the downstream distance increases from $x/\delta = 1$ to 12, this stable value of $T^+_{c',m}$ increases monotonically from $T^+_{c',m} = 0.046$ to 0.13, a trend that is consistent with that shown in Fig. 5.14.

Because the characteristic temporal scale of concentration fluctuations varies with both x^+ and y^+ (i.e., $T^+_{c',m} = T^+_{c',m}(x^+, y^+)$), it is beneficial to further examine how this characteristic temporal scale evolves in the streamwise direction. Figure 5.16

shows how $T^+_{c',m}$ varies with x/δ at a given wall-normal distance. Clearly, there are two monotonic trends in the figure. Firstly, as the wall-normal distance increases, the characteristic temporal scale of concentration fluctuations as indicated by the value of $T^+_{c',m}$ reduces monotonically, a conclusion that is consistent with that based on the previous analysis of Figs. 5.14 and 5.15. Secondly, as the downstream distance x/δ increases, the characteristic temporal scale of concentration fluctuations increases. This is due to the fact that the plume grows in the streamwise direction, which facilitates the growth of the characteristic spatial and temporal scales of concentration fluctuations for turbulent mixing. It is interesting to observe that in the viscous sublayer (for $y^+ \leq 5$), the value of $T^+_{c',m}$ increases initially, and then flattens out as x/δ further increases. This physical feature is expected, because once the plume hits the wall, the turbulent dispersion of the scalar becomes stabilized in the near-wall region, exhibiting a self-similar pattern in the downstream region.

Chapter 6

Study of Turbulent Dispersion of Concentration Plume Emitting from a Line Source over a Rib-roughened Surface

6.1 Abstract

Turbulent dispersion of concentration plume emitting from a horizontal line source over a k-type roughness surface has been studied using direct numerical simulations (DNS). Four test cases have been compared to investigate the effects of the source elevation and location on plume dispersion in a turbulent boundary layer. The transport process of the concentration is investigated in both physical and spectral spaces which include analyses of statistical moments of the concentration field, decay rate, plume width, pre-multiplied spectra of the velocity and concentration fields, and the probability density function (PDF) of concentration fluctuations. It is observed that as the mean plume development enters the long-range dispersion stage, the decay

rates of mean concentration fields begin to feature a constant slope of $-3/2$, while the vertical spread of the mean plume features a constant slope of $1/3$ in all four line source release cases in a ribbed wall flow. By comparing the characteristic length scales of both the spanwise velocity and scalar fields, two distinct stages of the instantaneous plume development are observed, dominated by the turbulent convective and diffusive mechanisms. It is discovered that the transition from the turbulent convective stage to the turbulent diffusive stage occurs more rapidly for line sources placed near the wall and inside the cavities.

6.2 Test Cases

Figure 6.1 shows a schematic of the computational domain, coordinate system, mesh, and four line sources positions of the test cases. The flow is statistically stationary and fully-developed in both streamwise and spanwise directions, driven by a mean streamwise pressure gradient Π. The Reynolds number is fixed at $Re_\tau = u_\tau \delta/\nu = 1150$, where δ is the plane channel height, ν is the kinematic viscosity of the fluid, and u_τ is the wall friction velocity determined as

$$u_\tau^2 = -\frac{\delta}{\rho}\Pi \quad , \tag{6.1}$$

where ρ is the density of the fluid. The size of the computational domain is set to $L_x \times L_y \times L_z = 64h \times 15h \times 31h$, where h is the rib height. The rib element has a square cross section, such that its height and width are equal, i.e., $h = W$. In total, eight rib periods are considered in all four test cases. The pitch to height ratio is $P/h = 8$, and therefore, the rib elements are considered as k-type roughness. According to the classical rib-roughened TBL theory [63; 64; 65; 66; 67], square bars mounted on the wall can be considered as k-type roughness if $P/h > 4$.

As shown in Fig. 6.2, four test cases are considered with different line source positions in our comparative study. There are two ground-level source cases (GS1

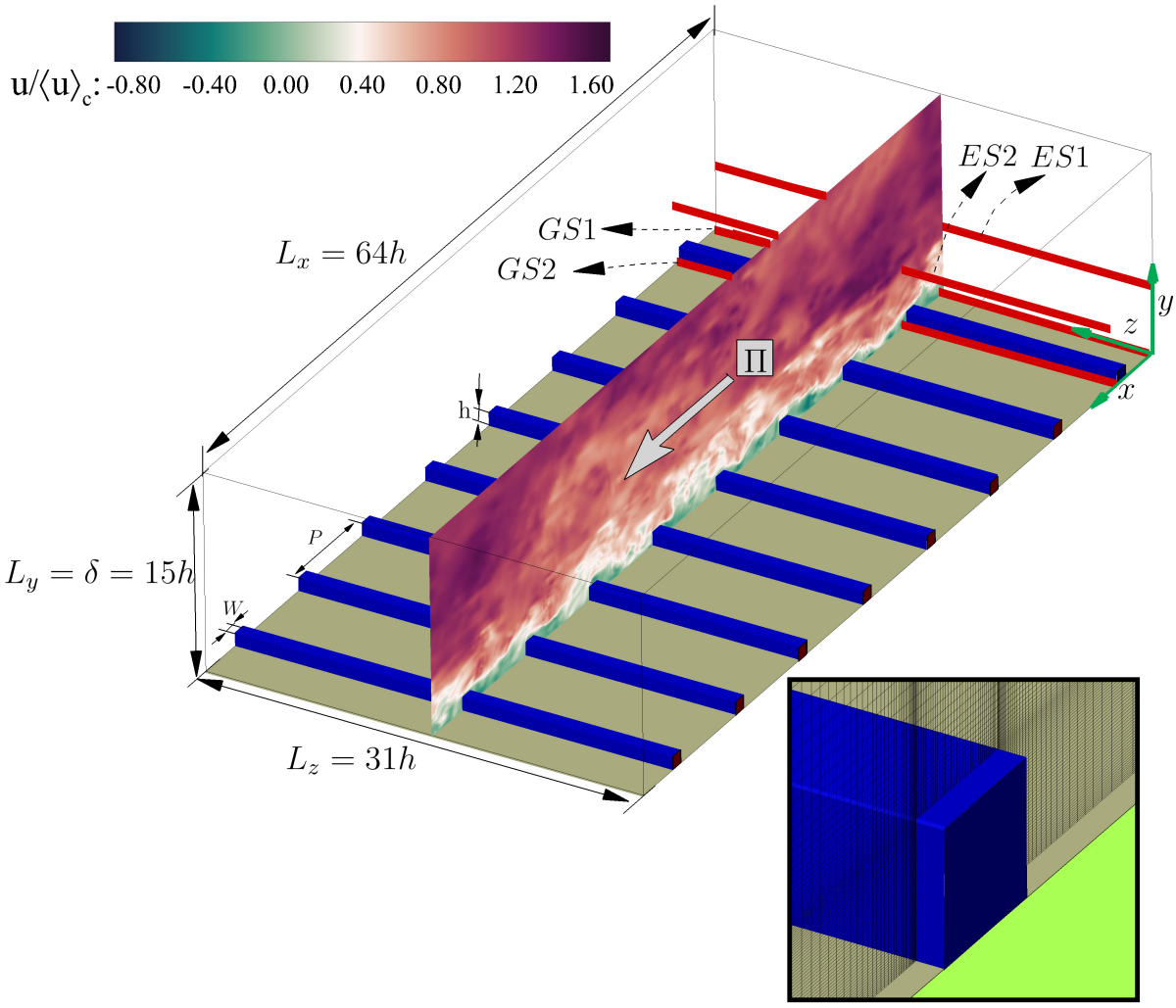

Figure 6.1: Schematic of the computational domain, mesh and coordinate system. Four test cases are considered, with a single line sourced positioned at the ground level (for GS1 and GS2), and at an elevation of $y_s/h = 2.0$ (for ES1 and ES2). The plane channel height is set to $\delta = 15h$. The instantaneous non-dimensionalized streamwise velocity $u/\langle u\rangle_c$ is shown in the middle vertical plane. The origin is located at the crossing of the inlet plane, the bottom wall and left vertical boundary plane. The mesh is refined near all solid surfaces as shown in the partially enlarged sub-panel.

and GS2), with the line source placed in the reattachment and recirculation zones of the ribbed wall flow, at $(x_s/h, y_s/h) = (0.0, 0.0)$ and $(5.0, 0.0)$, respectively. In addition, two elevated source cases (ES1 and ES2) are also considered, positioned

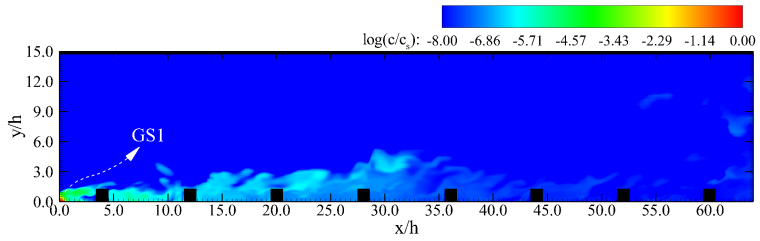

(a) Case GS1

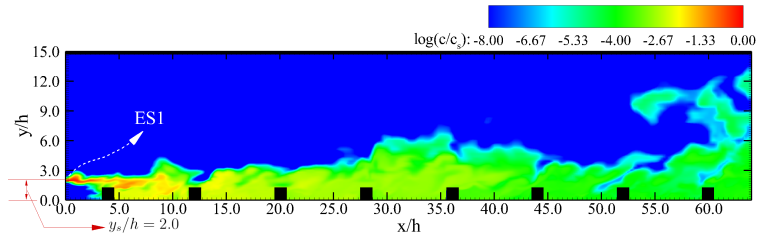

(b) Case ES1

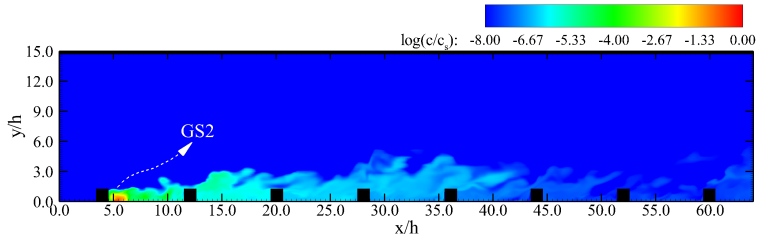

(c) Case GS2

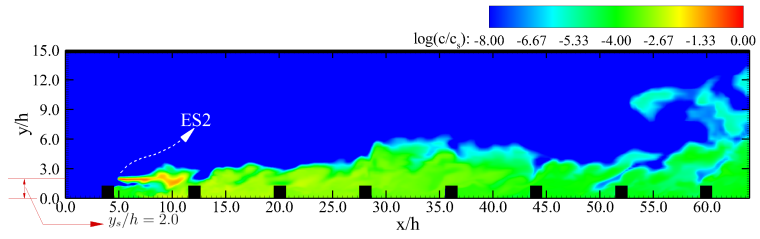

(d) Case ES2

Figure 6.2: The instantaneous concentration fields associated with four different line source positions. The line sources are equal in strength.

well above the ribs at $(x_s/h, y_s/h) = (0.0, 2.0)$ and $(5.0, 2.0)$, respectively. In case GS1, the source approaches the reattachment point, and the convection mechanism dominates the concentration mixing process. By contrast, in case GS2, the line source

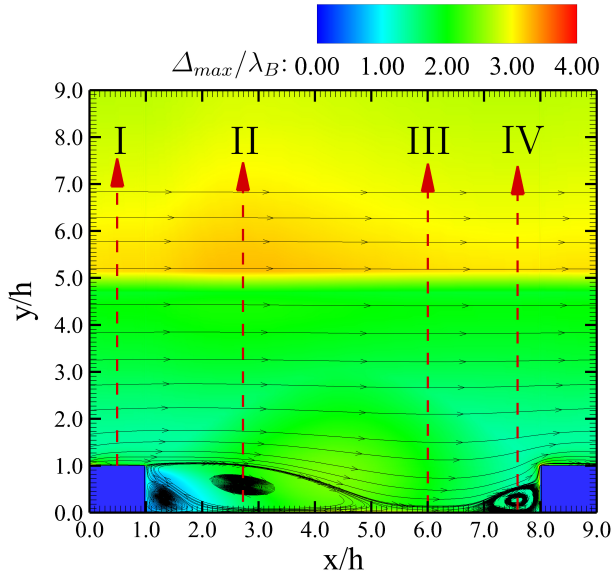

Figure 6.3: Ratio of the maximum grid size to the the Batchelor length scale (Δ_{max}/λ_B) in the central vertical (x-y) plane.

is located within the recirculation region, and the primary mixing mechanism of the short-range dispersion is the diffusion mechanism. The diameter of the line sources is $\sigma_0 = 0.008\delta$. From Fig. 6.2, it is clear that the instantaneous concentration plume are qualitatively different in these four test cases, especially in regions near the line source. Furthermore, by comparing Figs. 6.2(a) with Fig. 6.2(b), and Figs. 6.2(c) with Fig. 6.2(d), it is evident that the instantaneous concentration plume pattern is sensitive to the source elevation. The characteristics and statistical moments of the turbulent concentration field will be analyzed thoroughly later in section 6.4.

The simulations were executed until statistically stationary conditions were attained for both velocity and concentration fields, after which various statistical moments were computed over a time duration of 20 large eddy turn over times (LETOT). Here, one LETOT is defined as δ/u_τ.

Numerical simulations were performed and data were stored on local and WestGrid (Western Canada Research Grid) supercomputers. The DNS was executed until statistically stationary conditions were attained for both velocity and concentration

fields, after which various statistical moments were computed over a time duration of 20 large eddy turnover times (LETOT). The DNS was performed with a grid system of $1056 \times 140 \times 300$ nodes in the x-, y- and z-directions, respectively. As shown in Fig. 6.1, the mesh was refined close to the wall and near the ribs. The minimum grid resolution was kept at $\Delta x^+ = 2.49$ in the streamwise direction, and at $\Delta y^+ = 0.12$ in the vertical direction in order to capture the wall shear. A uniform grid spacing with resolution $\Delta z^+ = 7.91$ was applied in the z-direction. To conduct DNS of turbulent dispersion of concentration, the grid must be fine enough to capture the smallest turbulence scale at the so-called the Batchelor scale, defined as $\lambda_B = \eta/Sc^{0.5}$, where η is the Kolmogorov length scale defined as $\eta = (\nu^3/\epsilon)^{1/4}$, and ϵ is the local dissipation rate of turbulence kinetic energy (TKE) defined as $\epsilon = \nu \left\langle \frac{\partial u_i'}{\partial x_k} \frac{\partial u_i'}{\partial x_k} \right\rangle$. In this study, the Schmidt number $Sc = \nu/\alpha$ is equal to 1.0, such that the Kolmogorov scale is identical to the Batchelor scale, which represent the smallest length scales for turbulent transport of momentum and concentration, respectively. Figure 6.3 shows the ratio of the maximum grid size (i.e., $\Delta_{\max} = \max(\Delta x, \Delta y, \Delta z)$) to the Batchelor scale. Clearly, the grid resolution is sufficiently fine for conducting DNS of turbulent mixing of concentration, with $0.0 \leq \Delta_{\max}/\lambda_B \leq 4.0$.

6.3 Velocity Field

Turbulent dispersion of concentration in a rib-roughened wall flow is influenced by both small and large scale eddy motions. Therefore, prior to any analysis of the statistical moments of the concentration field, it is useful to briefly examine the characteristics of the velocity field. The instantaneous and mean flow patterns have been demonstrated in Fig. 6.1 and Fig. 6.3, respectively. Apparently, owing to the presence of the ribs, mean flow structures are induced around ribs. Specifically, we are interested in characteristics of the mean velocity field at the four positions shown in Fig. 6.3, corresponding to the center of the rib top (I), center of the recirculation

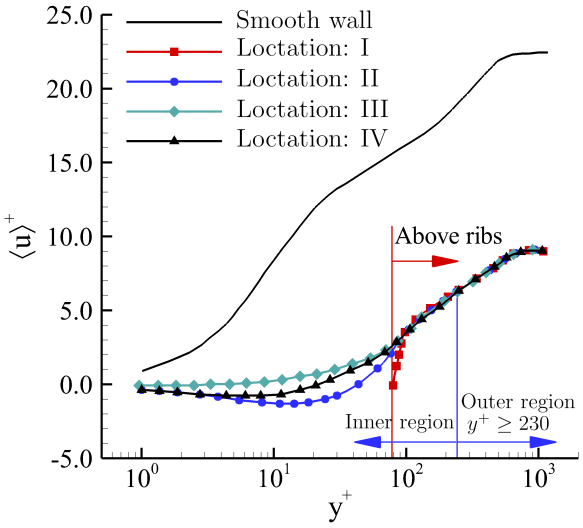

Figure 6.4: Wall-normal profiles of the mean stream velocity at positions I, II, III, and IV (see Fig.6.3), in comparison with the smooth wall result of Graaff *et al.* [2] (at $Re_\tau = 1100$). The vertical line delineates the inner and outer regions of the turbulent boundary layer over the ribbed bottom wall. The red line demarcates the vertical position of the rib crest..

bubble of the mean flow behind a rib (II), center of the attached boundary layer zone between ribs (III), and center of the vortex in the impinging zone immediately upstream of a rib (IV). Figure 6.4 compares the wall-normal profiles of the mean stream velocity $\langle u \rangle^+$ at four streamwise positions I, II, III, and IV (see Fig. 6.3). To demonstrate of rib effects, the experimental results of Graaff *et al.* [2] (for the smooth wall flow at $Re_\tau = 1100$) are also displayed for the purpose of comparison. In the figure, superscript "+" indicates a variable expressed with respect to the wall coordinate, non-dimensionalized using the wall friction velocity u_τ and kinematic viscosity ν. A pair of angular brackets $\langle \cdot \rangle^+$ denote averaging over time and homogeneous directions. From Fig. 6.4, it is seen that compared with the smooth channel flow profile, there is an apparent roughness downshift at all four streamwise positions I, II, III and IV. As is evident in Fig. 6.4, within the outer region of the TBL over the ribbed wall (for $y/h \geq 3.0$, or $y^+ \geq 230$, approximately), the obtained DNS results support

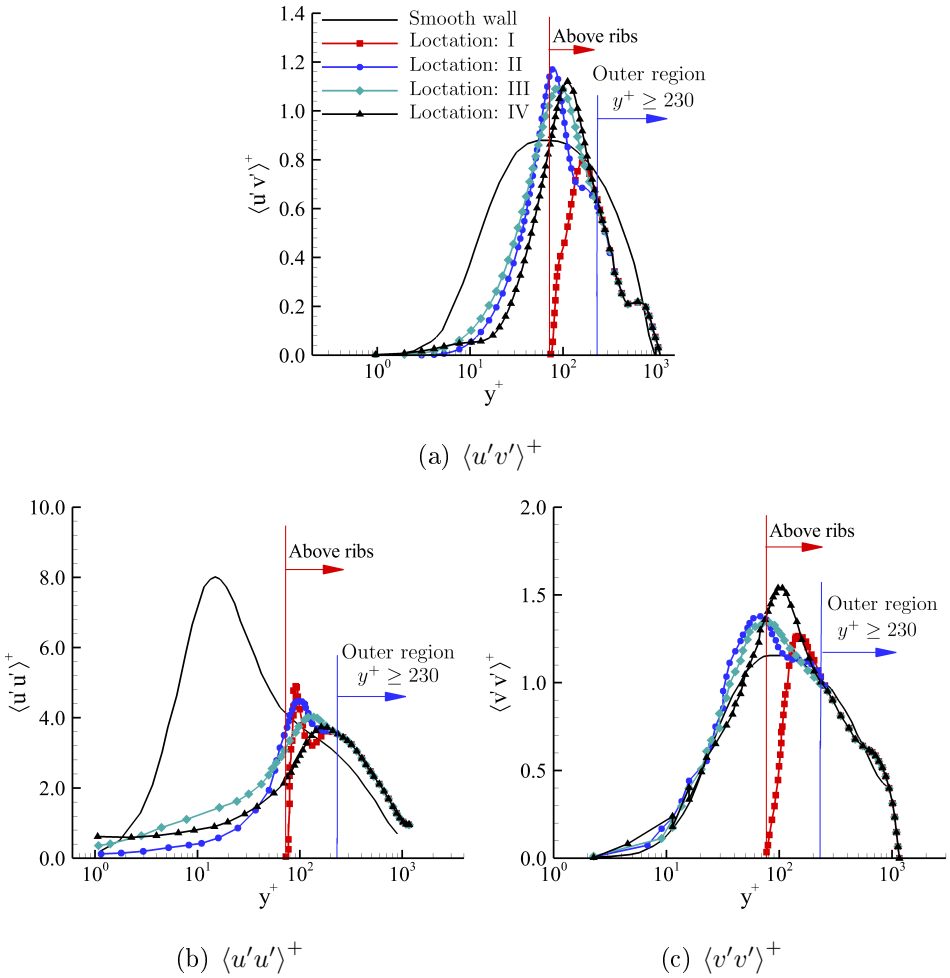

(a) $\langle u'v' \rangle^+$

(b) $\langle u'u' \rangle^+$

(c) $\langle v'v' \rangle^+$

Figure 6.5: Vertical profiles of Reynolds shear and normal stresses $\langle u'v' \rangle^+$, $\langle u'u' \rangle^+$ and $\langle v'v' \rangle^+$ at positions I, II, III, and IV (see Fig.6.3), in comparison with the smooth wall results of Graaff *et al.* [2] (at $Re_\tau = 1100$). The blue vertical line delineates the inner and outer regions of the turbulent boundary layer over the ribbed bottom wall. The red line demarcates the vertical position of the rib crest. .

the Reynolds number similarity hypothesis of Townsend and confirm the similarity between smooth- and rough-wall boundary layers.

Figure 6.5 shows the vertical profiles of the Reynolds shear stress $\langle u'v' \rangle^+$ and the two non-trivial normal stresses $\langle u'u' \rangle^+$ and $\langle v'v' \rangle^+$ at four streamwise positions I, II, III and IV. For the purpose of comparison, the experimental results of Graaff *et al.* [2] for a smooth wall flow at $Re_\tau = 1100$ is also displayed. As is evident from

Fig. 6.5, the profiles of the Reynolds shear stress and normal stresses all peak at an elevation slightly above the rib crest. This is not surprising, as strong shear layers are generated at the rib tops which promote turbulent production rate and enhances turbulent mixing. From Fig. 6.5(a), it is seen that the peak magnitude of Reynolds shear stress $\langle u'v' \rangle^+$ of the current ribbed-wall flow is larger than that of a smooth channel flow. By contrast, as shown in From Fig. 6.5(b), the peak magnitude of the streamwise Reynolds normal stress $\langle u'u' \rangle^+$ decreases significantly in the ribbed-wall flow case compared to that of the smooth-wall flow case. This is because the rib elements break up the streamwise vortices effectively, therefore preventing formation of overly-elongated energetic streamwise turbulence structures as in a smooth-wall flow. From Fig. 6.5(c), it is seen that the peak magnitude of the vertical Reynolds normal stress $\langle v'v' \rangle^+$ are comparable between the ribbed-wall and smooth wall channel flows. As is clear in Figs. 6.5(a) and 6.5(b), the profile patterns of $\langle u'v' \rangle^+$ and $\langle u'u' \rangle^+$ at different streamwise positions are considerably different from that of the smooth channel flow within the inner region of the rough-wall boundary layer. However, in the outer region of the rough-wall boundary layer well above the ribs, the profiles of $\langle u'v' \rangle^+$ and $\langle u'u' \rangle^+$ at different streamwise positions collapse, exhibiting a pattern similar to that of the smooth-wall channel flow. After an examination of the mean and turbulent characteristics of the velocity field, we can now focus on investigations into turbulent dispersion of the concentration plume through analysis of its statistical moments in both physical and spectral spaces in the following section.

6.4 Statistical Moments of the Concentration Field

6.4.1 Mean Concentration Field

Figure 6.6 compares the streamwise profiles of the decay rates and vertical mean plume widths of the four test cases. The decay rate of a mean plume is measured

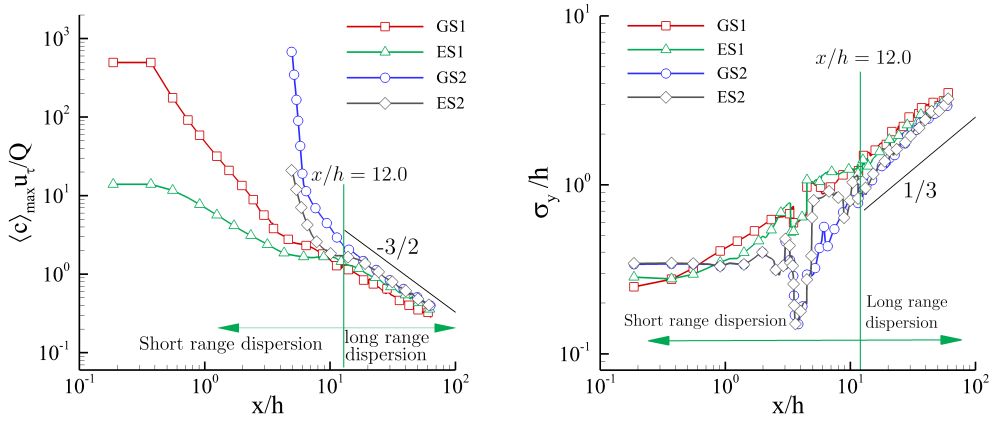

(a) Decay rate

(b) Vertical mean plume width

Figure 6.6: Mean decay rate and mean plume width of four test cases. The vertical line divides the short and long range dispersion regimes.

based on the maximum mean concentration value $\langle c \rangle_{max}$, while the vertical mean plume width is determined as

$$\sigma_y^2 = \frac{\int_{y_m}^{\delta} (y - y_m)^2 \langle c \rangle (x, y) dy}{\int_{y_m}^{\delta} \langle c \rangle (x, y) dy} \quad , \tag{6.2}$$

where y_m represents the vertical position corresponding to the maximum mean concentration. These two parameters represent overall measurements of a spatially-developing mean concentration field associated with a line source emission. In this figure, the maximum mean concentration value $\langle c \rangle_{max}$ and the mean vertical plume width σ_y have been non-dimensionalized by the friction velocity u_τ, rib height h, and mean scalar flux $Q = \int_0^{\delta} \langle u \rangle \langle c \rangle \, dy/\delta$. By comparing GS1 with GS2, and ES1 with ES2, it is seen that near the source, the maximum value of mean scalar field $\langle c \rangle_{max}$ is larger for the cases of near rib plume emission (GS2 and ES2). The area associated with a varying reduction rate of $\langle c \rangle_{max}$ is referred to as the short-range dispersion. Then, the development of the mean plume enters the long-range dispersion stage (at a downstream distance of approximately $x/h \geq 12.0$), which features a constant decay rate of $\langle c \rangle_{\max}$ of a slope of $-3/2$. The short- and long-range dispersions of the

mean plume are labeled in Fig. 6.6(a). As is clear in Fig. 6.6(b), the vertical mean plume width is significantly influenced by the recirculation bubble leeward of the rib at approximately $x/h = 3.0$, especially for cases GS2 and ES2. Specifically, the recirculation bubble of the mean flow initially "traps" the concentration, and therefore, causing a significant reduction in the local vertical spread of the mean concentration (at approximately $x/h = 3.5$). By comparing Figs. 6.6(a) and 6.6(b), it is understood that the short- and long-range dispersion mechanisms also have a significant impact on the vertical spread of the mean plume. From Fig. 6.6(b), it is seen that the vertical spread of the mean plume (σ_y) features a constant slope of 1/3 for all four test cases. A careful perusal of Fig. 6.6(b) indicates that cases GS1 and ES1 have slightly a larger vertical mean plume spread than do cases GS2 and ES2. This is not surprising, simply because line sources GS1 and ES1 are positioned upstream of GS2 and ES2.

For a concentration plume dispersing from a point source in homogeneous isotropic turbulence [14, 25], the mean plume exhibits a Gaussian pattern. However, in the current four test cases of line source dispersion in a rib-roughed wall flow, the spread of mean plume is expected to deviate from the well-known Gaussian pattern due to the influences of near-wall isotropy of the flow and the vortex motions induced by the ribs. The presence of wall-anistropy in the context of a smooth-wall flow is known to cause a drift of the mean plume towards the wall according to the experimental study of Lavertu and Mydlarski [29] and DNS study of Noormohammadi and Wang [23]. The additional presence of the rib elements further complicates the mean plume development, making it to further deviate from a Gaussian distribution in the vertical direction. This is well understood from the DNS study of scalar dispersion downstream of a wall-mounted cube conducted by Rossi *et al.* [68]. In the following, we compare the mean concentration fields of the four test cases, which are influenced by several factors, including the wall shear, rib-induced vortices, and elevation of the line source.

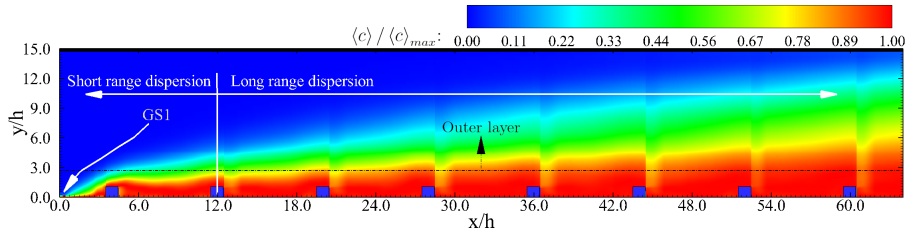

(a) Case GS1

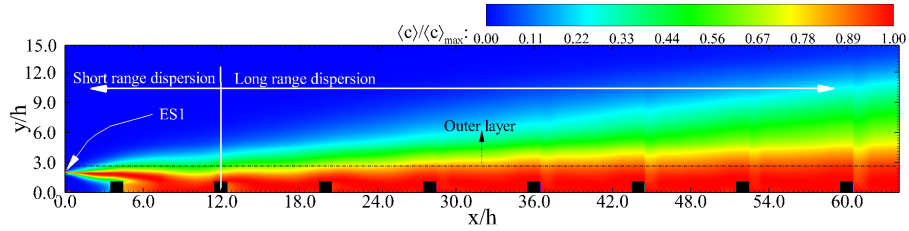

(b) Case ES1

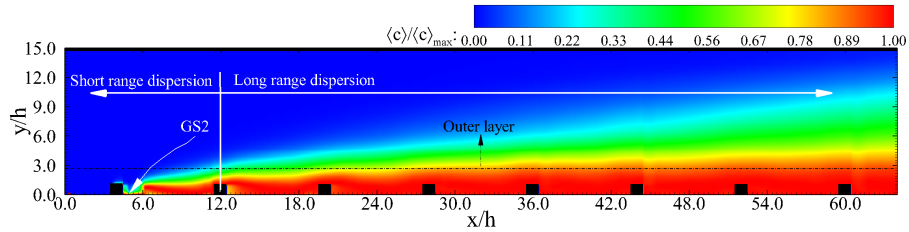

(c) Case GS2

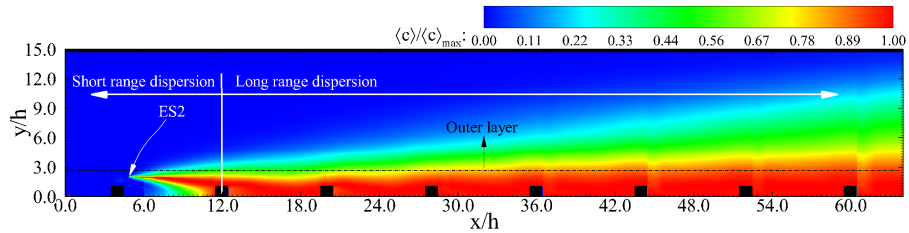

(d) Case ES2

Figure 6.7: Mean plume development in the streamwise and vertical directions for the four test cases.

Figure 6.7 compares the mean concentration patterns of the four test cases. In order to demonstrate effectively the vertical drift of the plume center, the local mean concentration field has been normalized by its local maximum, as $\langle c \rangle / \langle c \rangle_{\max}$. From

Figs. 6.7(a)-(d), it is clear that the difference in the mean concentration fields between these four test cases is the most distinct in the near-source region featuring the short-range dispersion. The mean concentration field exhibits a similar pattern in the long-range dispersion regions, which is consistent with the previous analysis of Fig. 6.6. The downdrift of the mean plume in the near-source region is evident in the two elevated line source release cases ES1 and ES2. As shown in Fig. 6.7(b), the concentration released from ES1 is sucked into the cavity between the first and second ribs. By contrast, as shown in Fig. 6.7(d), the concentration released from ES2 is mainly sucked into vortex IV (see Fig. 6.3) between the first and second ribs, and the cavity between the second and third ribs. These differences between cases ES1 and ES2 are resulted from their different streamwise source positions and show clearly the impact of rib-induced vortices (see Fig. 6.3) on the mean plume development in the near-source regions. To clearly demonstrate the rib effects on the two ground-level line source release cases GS1 and GS2, their mean plume pattern in the first rib period (between the first and second ribs) are partially enlarged and shown in Figs. 6.8(a) and 6.8(b), respectively. The difference in the mean plume patterns between the two ground-level sources GS1 and GS2 are evident by comparing Figs. 6.8(a) and 6.8(b). Because GS1 is located at the inlet (upstream of the first rib, see Fig. 6.1), the concentration is sucked into the recirculation regions and filled in the entire cavity between the first and second ribs in Fig. 6.8(a). However, it is very interesting to observe from Fig. 6.8(b) that because GS2 is located at the corner on lee side of the first rib, the dispersion of the mean concentration near the source is dominated by the corner vortex, which channels the concentration plume downstream along its streamlines near the wall, such that only half of the recirculation (vortex II, see Fig. 6.3) is occupied by the concentration plume.

Figure 6.9 shows the vertical profiles of mean scalar field $\langle c \rangle$ at different streamwise positions above a rib top (through line I labeled in Fig. 6.3) varying from the second to the eight rib periods. As is clear in Fig. 6.9, for all four line source release cases,

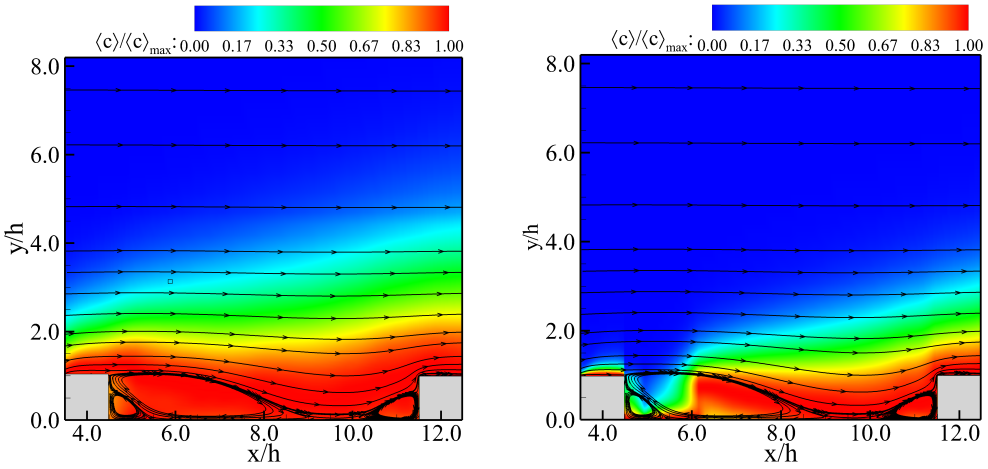

(a) Case GS1 (b) Case GS2

Figure 6.8: Comparison of the mean plume and flow patterns of GS1 and GS2 between the first and second ribs.

the vertical profile of the mean concentration exhibits a quasi Gaussian distribution with mean plume peaks occurring within the inner layer ($y/h \leqslant 3.0$) around the rib crest ($y/h = 1.0$). The dispersion of the plume in a wall-bounded flow is dominated by streamwise convention. In the vertical direction, however, the flow convection effect reduces due to the presence of the wall, and therefore, the development of the plume is also significantly influenced by the turbulent diffusion mechanism. As such, in all four test cases, the normalized mean concentration profiles $\langle c \rangle / \langle c \rangle_{max}$ exhibit a quasi Gaussian pattern. Furthermore, as the streamwise distance from the line source increases, the profiles of $\langle c \rangle / \langle c \rangle_{max}$ expands in the vertical direction monotonically as shown in Fig. 6.9. To refine the study, the profiles of $\langle c \rangle / \langle c \rangle_{max}$ at four characteristic positions (through lines I, II, III and IV shown in Fig. 6.3) within each rib period related to case GS2 are plotted in Fig. 6.10. Similar to Fig. 6.9, a quasi Gaussian pattern is observed at all positions in all three rib periods. By comparing Figs. 6.10(a) with 6.10(b) and 6.10(c), it is clear that the vertical mean plume spread increases monotonically in an apparent manner in the second rib period. However, as

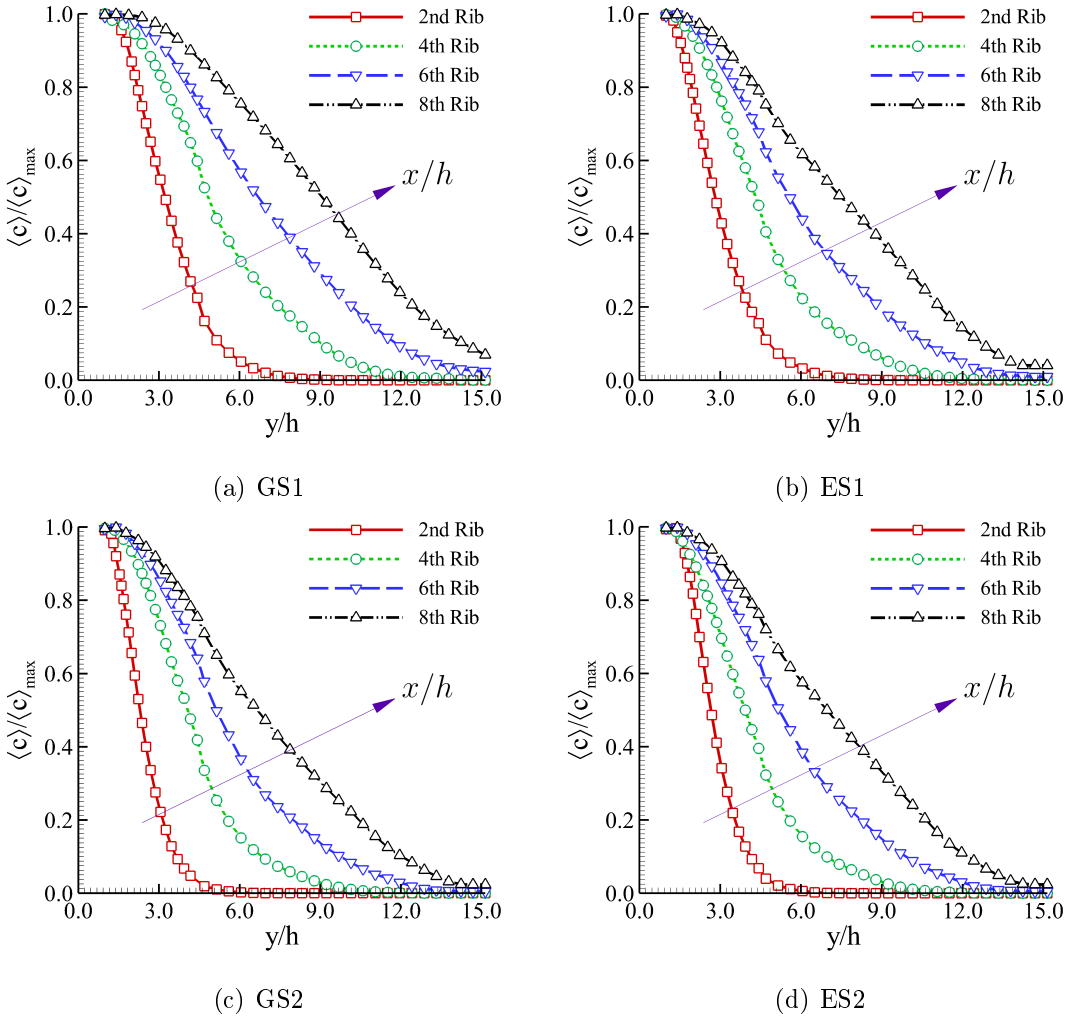

(a) GS1 (b) ES1

(c) GS2 (d) ES2

Figure 6.9: Streamwise evolution of the vertical mean scalar profile $\langle c \rangle / \langle c \rangle_{max}$ at the position on the rib top through line I of Fig. 6.3.

the streamwise distance from the line source increases to the fourth and sixth periods, the profiles at different streamwise positions converge, indicating a uniform mixing status of the mean plume field near the wall between two adjacent ribs.

In our recent study of turbulent dispersion of concentration emitting from dual line sources in a smooth plane-channel flow [23], we reported an interesting self-similarity property of the mean concentration field analogous to that of the mean velocity field of a wall jet [55; 15]. In our method [23], the mean concentration value

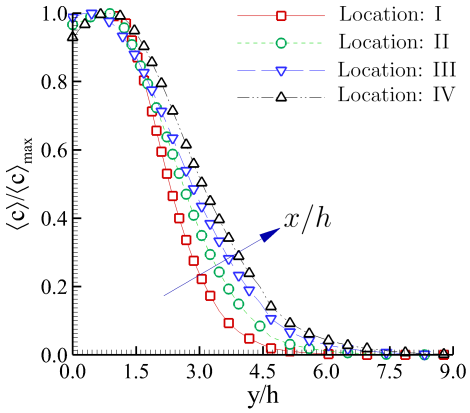

(a) Between the second and third ribs

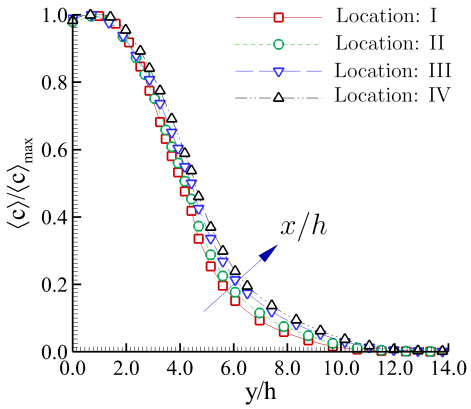

(b) Between the fourth and fifth ribs

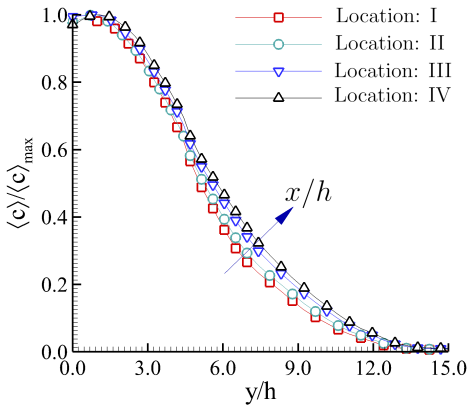

(c) Between the sixth and seventh ribs

Figure 6.10: Variation of the vertical profiles of $\langle c \rangle / \langle c \rangle_{max}$ at the four characteristic streamwise positions through lines I, II, III, and IV of Fig. 6.3 in the second, fourth and sixth rib periods. Data are extracted from case GS2.

is normalized by the local maximum mean concentration value as $\langle c \rangle / \langle c \rangle_{max}$, while the vertical coordinate is non-dimensionalized as $\xi = y/y_{1/2}$, where $y_{1/2}$ is the half concentration spread, defined as the vertical distance from the wall at which the mean concentration value drops to one half of its local maximum value $\langle c \rangle_{max}$. In the current study of turbulent dispersion of concentration released from a horizontal line source in a rib-roughened wall flow, it would be interesting to examine if the mean concentration may reserve the self-similarity property as in a smooth plane channel

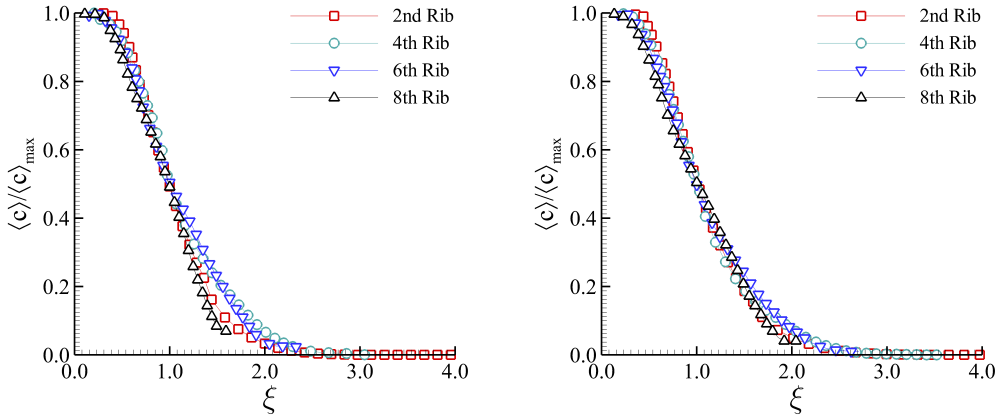

(a) Case GS1

(b) Case ES1

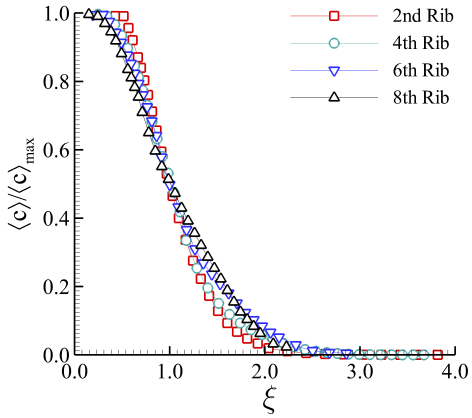

(c) Case GS2

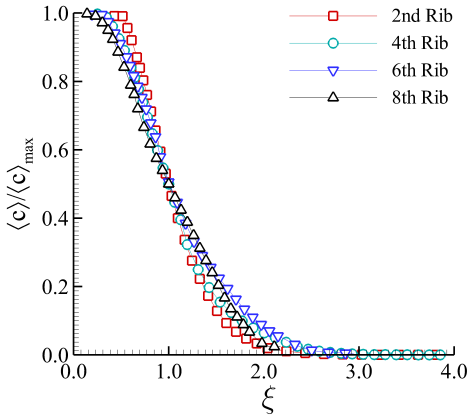

(d) Case ES2

Figure 6.11: Self-similarity of the non-dimensionalized mean concentration profile $\langle c \rangle / \langle c \rangle_{max}$ at position I (see Fig. 3) in different rib periods for the four test cases.

flow. Figure 6.11 plots the profiles of $\langle c \rangle / \langle c \rangle_{max}$ with respect to ξ at position I (see Fig. 6.3) in the 2nd, 4th, 6th and 8th rib periods along the streamwise direction for the four test cases. Indeed, it is seen that the profiles of $\langle c \rangle / \langle c \rangle_{max}$ of different rib periods collapse in general, indicating a quasi self-similarity in all four test cases. This is an interesting result which further leads to a more general conclusion that the self-similarity in the vertical profile of a mean concentration field resulted from a line release is a quite robust property either in a turbulent plane-channel flow [23] or in a

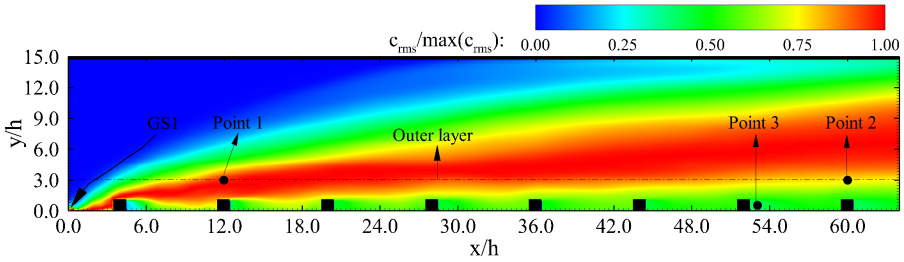

(a) Concentration fluctuations

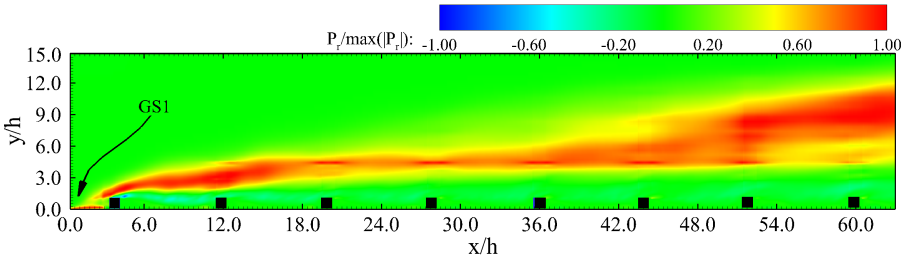

(b) Production of the concentration fluctuations

Figure 6.12: Contours of (a) root-mean-square (RMS) c_{rms} of the concentration fluctuations $c'$and (b) production rate of P_r concentration fluctuations. Both quantities have been non-dimensionlized with respect to the maximum values of P_r and c_{rms}. Data are extracted from case GS1. The coordinates for points 1, 2 and 3 in (a) are $(x/h, y/h) = (12.0, 3.0)$, $(60.0, 3.0)$ and $(53.0, 0.5)$, respectively.

turbulent rib-roughened wall flow.

6.4.2 Concentration Fluctuations and Statistics

Figure 6.12(a) shows contours of the root-mean-square (RMS) value of turbulent concentration field for case GS1. Clearly, due to the presence of the ribs, the turbulent fluctuations of the instantaneous concentration field are the most intense immediately above the ribs. Furthermore, as the downstream distance from the line source increase, the vertical spread of the RMS concentration contours increases, and the center of the contours (corresponding to the maximum RMS values) elevates slightly as a result of the plume development, mainly due to turbulent convection and diffusion mechanisms in the streamwise and vertical directions, respectively. In fact,

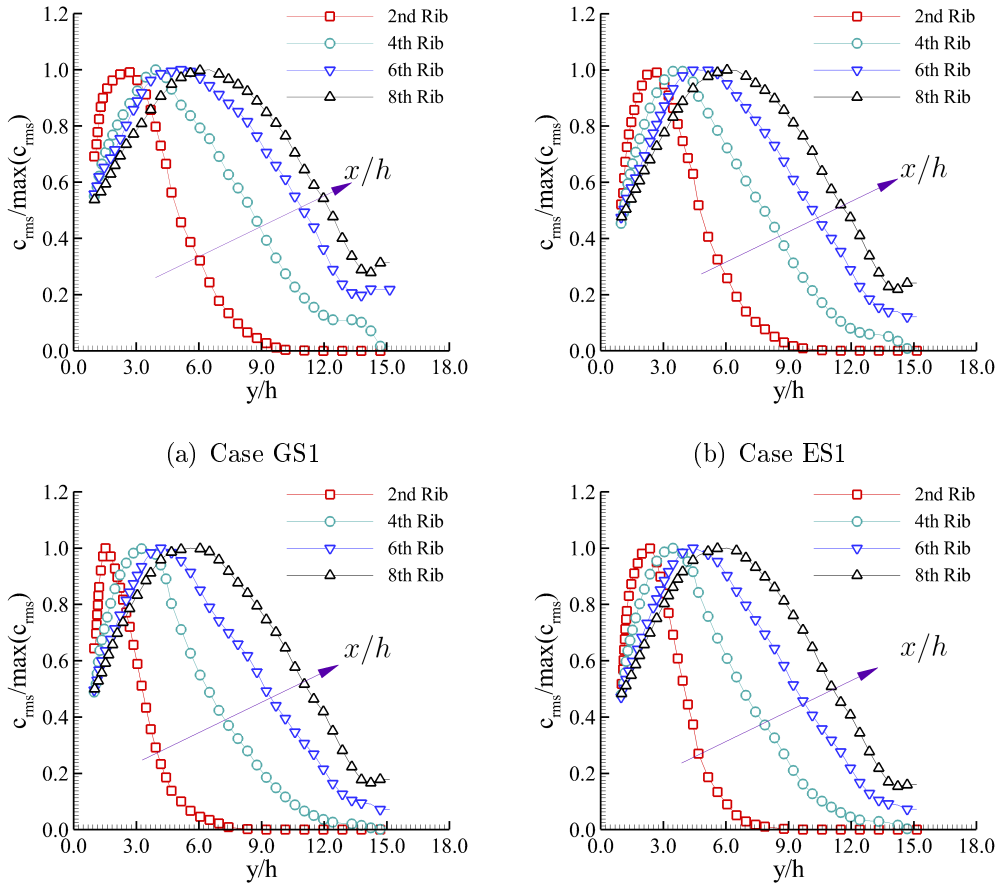

(a) Case GS1

(b) Case ES1

(c) Case GS2

(d) Case ES2

Figure 6.13: Vertical profile of the RMS concentration at four different streamwise locations for four test cases. The RMS concentration value c_{rms} has been non-dimensionalized using its local maximum value, $\max(c_{rms})$. Data are extracted from the position I (see Fig. 6.3).

the maximum values of c_{rms} occur in the outer layer of the boundary layer over the ribbed wall for $y/h \geq 3.0$. The physical mechanism underling the RMS values shown in Fig. 6.12(a) relates to the turbulent production rate of the concentration variance, which is defined in the current statistically 2D flow configuration as $P_r(x,y) = -2\left[\langle u'c'\rangle \partial\langle c\rangle/\partial x + \langle v'c'\rangle \partial\langle c\rangle/\partial y\right]$. By comparing Figs. 6.12(a) with 6.12(b), it is clear that the contour patterns of P_r is the similar to that of RMS. The RMS concentration contour patterns shown in Fig. 6.12 are intuitive, and in

the following context, we will refine our study by examining the characteristics of concentration fluctuations quantitatively in both physical and spectral spaces. In particular, we are interested in understanding the characteristics of concentrations fluctuations at points 1, 2 and 3 labeled in Fig. 6.12(a), which correspond to the streamwise positions I and II of the flow field shown in Fig. 6.3.

Figure 6.13 shows the vertical profile of concentration fluctuations at the center of the rib top (or, at position I shown in Fig. 6.3) in four different rib periods for all four test cases. As is evident in Fig. 6.13, in all four test cases, the vertical spread of c_{rms} increases monotonically while its vertical peak position drifts towards the channel center, as the downstream distance from the line source increases from the 2nd to the 8th rib. By comparing Fig. 6.13(a) with 6.13(b), and 6.13(c) with 6.13(d), it is clear that the difference between the ground- and elevated-source release scenarios is the most apparent at the 2nd rib, which is located near the line source. This difference reduces significantly as the downstream distance from the line source increases till the 4th rib and after. Furthermore, by comparing Fig. 6.13(a) with 6.13(c), and 6.13(b) with 6.13(d), it is seen that the difference in the vertical profiles of c_{rms} between different streamwise source positions is the most sensitive in the near-source position around the 2nd rib, and becomes insensitive in the far downstream region. Consistent with the qualitative results shown previously in Fig. 6.12(a), it is evident in Fig. 6.13 that the peak values of c_{rms}, in the 4th, 6th and 8th rib periods (for $x/h \geq 12$), appear mainly in the outer layer for $y/h \geq 3$.

6.4.3 Spectral Analysis of Concentration Fluctuations

Turbulent dispersion of a concentration plume is dominated by the convection and diffusion mechanisms, as dictated by governing equation (2.3). In general, the TCS and TDS phases of plume development are dominated by large-scale energy-containing eddy motions associated with convection and small-scale turbulent eddy motions associated with diffusion of the concentration within a spatially developed plume. The

discussion of the TCS and TDS phases of concentration plume development has been detailed in Taylor [7], Stapountzis *et al.* [8], and Warhaft [4]. Studies of TCS and TDS of passive scalar dispersion in homogeneous isotropic turbulence has been carried out using DNS by Ahlman *et al.* [15] and Oskouie *et al.* [17], and through wind-tunnel measurement by Karnik and Tavoularis [25]. Recently, Noormohammadi and Wang [22, 24] performed DNS to study turbulent dispersion of concentration emitting from a horizontal line source in a smooth turbulent plane-channel flow, which features spanwise homogeneity in both velocity and concentration fields. They showed that the transition of plume development from TCS to TDS is not only influenced by the relative length scales of the velocity and concentration fields but also significantly complicated by the anisotropic effects of the wall boundary layer. To study the transition from the TCS stage to the TDS stage of a passive plume released from a horizontal line source in a wall-bounded flow, Noormohammadi and Wang [22] suggested a new approach based on a comparison of the characteristic length scales of the velocity and concentration fields, based on a spectral analysis. In this section, we further extend the application of this method to the analysis of plume development from the previous context of a smooth wall-flow to the current environment of a rib-roughened turbulent boundary layer flow.

In the current test case of turbulent dispersion of a plume released from a horizontal line source, both the velocity and concentration fields are statistically homogeneous in the spanwise direction. As such, the characteristic spanwise scales of the flow and passive plume can be determined by analyzing the spanwise spectra of the velocity and scalar fields, i.e. $E_{w'w'}(k_z) = \frac{1}{\pi}\int_{-\infty}^{+\infty} e^{-ik_z r} R_{w'w'}(r)dr$ and $E_{c'c'}(k_z) = \frac{1}{\pi}\int_{-\infty}^{+\infty} e^{-ik_z r} R_{c'c'}(r)dr$, respectively. Here, $R_{w'w'}(r) = \langle w'(z)w'(z+r)\rangle / w_{rms}^2$ and $R_{c'c'}(r) = \langle c'(z)c'(z+r)\rangle / c_{rms}^2$ are the spanwise correlation functions of the turbulent velocity and concentration fluctuations, respectively. The modes ($\lambda_{z,w'}^m$ and $\lambda_{z,c'}^m$) of the pre-multiplied spectra ($k_z E_{w'w'}$ and $k_z E_{c'c'}$) of velocity and concentration fluctuations correspond to the characteristic length scales the most energetic eddy motions

responsible for turbulent mixing of the momentum and concentration, respectively. Here, superscript 'm' denotes 'mode', $\lambda_z^+ = \lambda_z u_\tau/\nu$, $\lambda_z = 2\pi/k_z$ is the spanwise wavelength, and k_z denotes the spanwise wavenumber. For a 2D plume released from a horizontal line source in a channel flow, if the characteristic length scale of the turbulent flow field is larger than that of the turbulent concentration field (i.e., $\lambda^m_{z,w'} > \lambda^m_{z,c'}$), then the plume development is in a TCS stage dominated by the meandering effect of large-scale eddy motions associated with flow convection. However, if $\lambda^m_{z,w'} < \lambda^m_{z,c'}$, then the plume development is in a TDS stage, which features in-plume turbulent mixing of concentration. In a TDS stage of plume development, the relatively small-sized turbulent eddy motions occur within a plume, which contribute to turbulent diffusion of the concentration.

Figure 6.14 compares the streamwise variations of the characteristic length scales of w' and c' for all four test cases at three vertical positions of $y/h = 0.1,\ 1.0,$ and 2.0 (corresponding to elevations that are below the rib height, at the exact rib height, and above the rib height at the elevated source position for ES1 and ES2, respectively). Figure 6.14(a) compares the characteristic spanwise length scales of the turbulent velocity and concentration fields (i.e., $\lambda^m_{z,w'}$ and $\lambda^m_{z,c'}$, respectively) of the four test cases at $y/h = 0.1$ near the wall. Given the streamwise periodicity of the ribs, a quasi periodic pattern is observed in the profiles of both $\lambda^m_{z,w'}$ and $\lambda^m_{z,c'}$. Because the turbulent velocity field is periodical in both streamwise and spanwise directions, the value range of $\lambda^m_{z,w'}$ is consistent in different rib periods with $0.2 \leqslant \lambda^m_{z,w'}/h \leqslant 0.75$. From Fig. 6.14(a), it is clear that at this low elevation, the differences between the four test cases are small, mostly within the first two rib periods. Because the plume is developing in the streamwise and vertical directions, the characteristic length scale of the turbulent concentration field $\lambda^m_{z,c'}$ increases in general in the streamwise direction. Clearly, at this low elevation, the plume development is mostly in the TDS stage, as $\lambda^m_{z,w'} < \lambda^m_{z,c'}$ holds. This result is consistent with our previous DNS study of turbulent concentration dispersion emitted from a horizontal line source is a

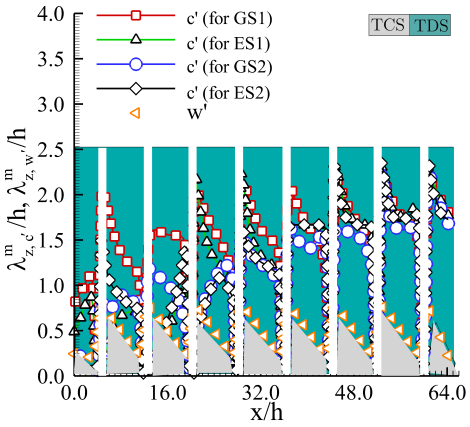

(a) $y/h = 0.1$

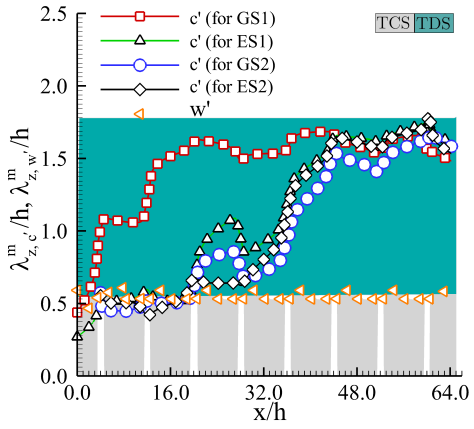

(b) $y/h = 1.0$

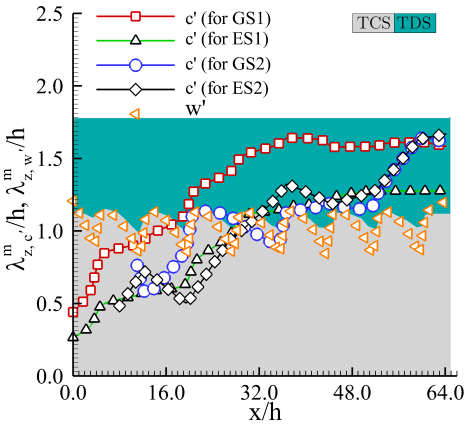

(c) $y/h = 2.0$

Figure 6.14: Spectral analysis of the transition from TCS to TDS in the plume development based on comparison of the characteristic length scales of turbulent velocity and concentration fields of four test cases at three characteristic elevations for (a) $y/h = 0.1$ below the rib height, (b) $y/h = 1.0$ at the rib height, and (c) $y/h = 2.0$ above the rib height (at the elevated sources position for ES1 and ES2).

smooth channel flow [22], which showed that the plume transitions from TCS to TDS rather rapidly near the wall. Because the profiles shown in Fig. 6.14(a) are extracted at a low elevation below the ribs, across the rib elements, $w \equiv 0.0$, $w' \equiv 0.0$ and $c \equiv 0.0$, $c' \equiv 0.0$. As such, $\lambda^m_{z,c'}$ and $\lambda^m_{z,c'}$ are undefined at the rib positions, shown as

empty (white) vertical stripes in Figs. 6.14(a) and 6.14(b).

By comparing Figs. 6.14(b) and 6.14(c) with Fig. 6.14(a), it is clear that the transition of the plume development from a TCS to a TDS stage becomes increasingly delayed as the elevation increases from $y/h = 0.1$ to $y/h = 1.0$ and further to 2.0. This is because the turbulent convection mechanism becomes increasingly dominant as the distance from the ribbed wall increases. From Fig. 6.14(b), it is seen that the characteristic length scale of the turbulence field is approximately $\lambda^m_{z,w'}/h = 0.65$ at the exact rib height ($y/h = 1.0$). Given that the transition from TCS to TDS is more rapid close to the wall, it occurs at $x/h = 2.15$ (upstream of the first rib) for the ground-level line source release case GS1. By contrast, for the other three test cases, ES1, GS2 and ES2, the transitions take place in the second rib period at approximately $x/h = 17.8$. From Fig. 6.14(c), it is seen that as the elevation increases well above the rib height at $y/h = 2.0$, turbulent convection becomes prominent, and the characteristic length scale of the turbulence field increases to approximately $\lambda^m_{z,w'}/h = 1.0$. The rib-induced quasi periodicity is apparent in the profile of $\lambda^m_{z,w'}/h$, which is a reflection of not only the streamwise convection above the ribs, but also the periodic vortex shedding and strong shear generated by the rib crests (see Figs. 6.1, 6.2 and 6.3). At a high elevation ($y/h = 2.0$) well above the ribs as shown in Fig. 6.14(c), the length scales of turbulent concentration field are all smaller than that of the turbulent velocity field, and therefore, the plume development of all four test cases is in a TCS stage near their line source locations. The transition from TCS to TDS occurs at approximately $x/h = 16.0$ for GS1, 28.0 for ES1, 21.0 for GS2 and 30.0 for ES2. Consistent with the previous analysis, plumes released from ground-level line sources transition from TCS to TDS more rapidly than do those released from elevated line sources in general.

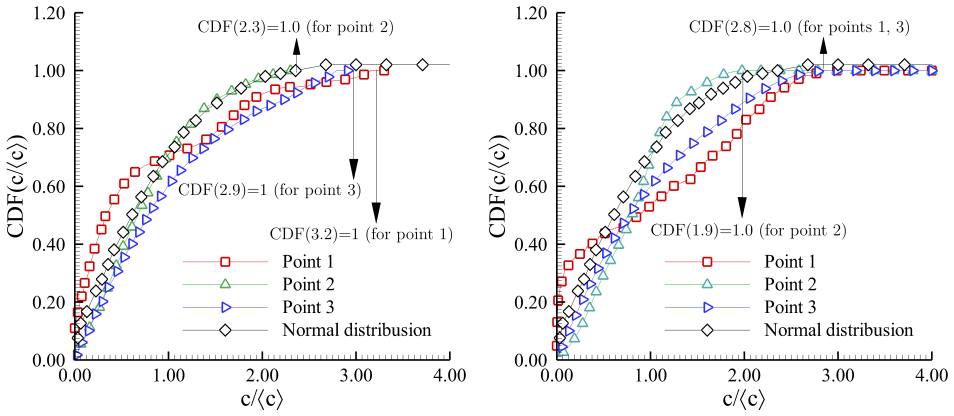

(a) Case GS1 (b) Case ES1

Figure 6.15: CDF of the instantaneous non-dimensionalized concentration field $c/\langle c\rangle$ for cases GS1 and ES1. The temporal values of c are extracted at points 1, 2, and 3 shown in Fig. 6.12.

6.4.4 Temporal Analysis of the Concentration Field

To provide a deeper insight into the instantaneous turbulent mixing of the concentration, it can be useful to further conduct a temporal analysis based on the cumulative distribution function (CDF) of the instantaneous scalar field c (with reference to the mean scalar field $\langle c\rangle$), and the probability density function (PDF) of the concentration fluctuations c' (with reference to c_{rms}).

Figure 6.15 plots the CDFs of the instantaneous non-dimensionalized concentration field $c/\langle c\rangle$ for cases GS1 and ES1. The temporal values of c are extracted at points 1, 2, and 3 shown in Fig. 6.12. For the purpose of comparison, the CDF of Gaussian distribution is also displayed. Clearly, the DNS data extracted at all three points lead to the upper limit CDF value of unity, which occurs at $c/\langle c\rangle = 3.2$, $c/\langle c\rangle = 2.3$, and $c/\langle c\rangle = 2.9$ for point 1, 2, and 3, respectively. These numbers are consistent with the plume development shown previously in Fig. 6.12 (also see Figs. 6.7(a) and 6.7(b)). For the probability of $c/\langle c\rangle$ to reach unity, the upper threshold value of the instantaneous concentration c is higher at point 1 than at points 2 and 3, because point 1 is

not only close to the line source but also located at the plume center. Point 2 has the same elevation as point 1, but it is located in the far downstream region, where the plume has spread significantly in the vertical direction which reduces the probability of possessing a high instantaneous concentration value. Compared to point 2, point 3 is located near the wall, and thus it has probability of a slightly higher value of c than at point 2, a result that is consistent with the pattern shown in Fig. 6.7(a). Clearly, the CDF profiles resemble the Gaussian distribution at points 2 and 3, revealing a TDS stage of plume development at these two selected points. By contrast, from our previous discussion of Fig. 6.14, it is understood that because point 1 is located in a TCS regime, the CDF profile deviates apparently from that of a Gaussian distribution. Figure 6.15(a) shows that for the plume development released from elevated line source ES1, the CDF value approaches unity at approximately $c/\langle d\rangle = 1.9$ at point 2, and 2.8 at points 1 and 3. Further by comparing Fig. 6.15(b)with 6.15(a), it is seen that the CDF profile patterns of points 2, and 3 are similar to that of the Gaussian distribution. This is because the fluctuating plume released from elevated line source ES1 is in a TDS stage at these two far downstream locations. By contrast, the CDF profile of point 1 apparently deviates from that of the Gaussian distribution, which is a reflection of the fact that the plume development is at a TCS stage at this near-source location.

The characteristics of the instantaneous concentration plume can be further investigated by examining the PDF of temporal concentration fluctuations. Figure 6.16 compares the PDFs of c'/c_{rms} at the same three positions 1, 2, 3 for both cases GS1 and ES1 as for the CDF plots shown previously in Fig. 6.15. As is evident from both Figs. 6.16(a) and 6.16(b), the PDF of c'/c_{rms} exhibits a quasi-Gaussian distribution at both points 2 and 3, indicating that the instantaneous plume development is in a TDS stage in the far downstream region in both cases of GS1 and ES1, a conclusion that is consistent with that based on our previous analysis of Fig. 6.15. By contrast, the PDF of c'/c_{rms} at point 1 deviates apparently from a Gaussian distribution, re-

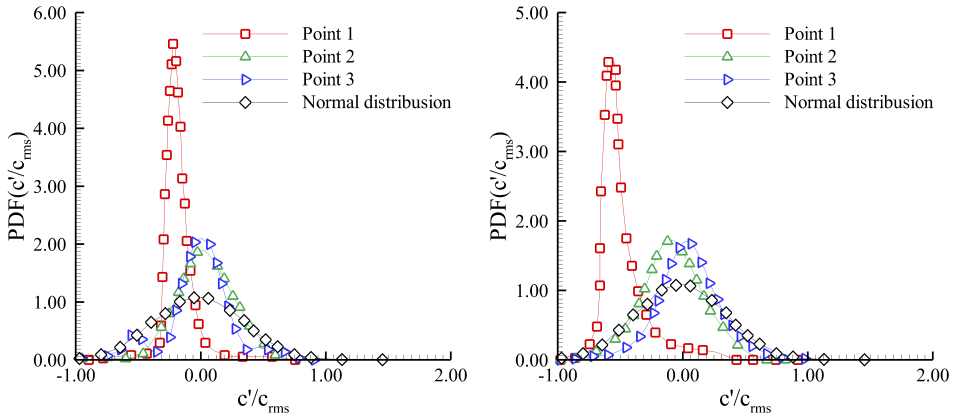

(a) Case GS1 (b) Case ES1

Figure 6.16: PDF of instantaneous non-dimensionalized concentration fluctuations $c'/\langle c_{rms}\rangle$ for cases GS1 and ES1. The temporal values of c are extracted at points 1, 2, and 3 shown in Fig. 6.12.

flecting the fact that the instantaneous plume development is in a TCS stage in the near-source position in both ground-level and elevated line source release cases.

Chapter 7

Conclusions and Future Work

7.1 Conclusions

In this thesis, DNS has been conducted to investigate turbulent dispersion of concentration plumes emitting from a single or dual line sources, positioned in horizontal or vertical direction. The plume dispersion occurs either in smooth-wall plane-channel flow or a rib-roughend open channel flow. This thesis includes four core chapters, i.e. Chapters 3-6, based on four independent sub-projects and journal publications or submissions. Major conclusions of these four sub-projects are summarized as follow:

7.1.1 DNS Study of Plume Emission from an Elevated Line Source in a Wall-Bounded Flow

In this sub-project, the dispersion of a passive scalar emitting from a near-wall line source and a central-domain line source is investigated using DNS. In the near-wall source release case, the mean concentration drifts towards the wall and peaks at the wall in the region far downstream of the line source, while in the central-domain release case, the mean concentration peaks at the source elevation throughout the entire domain. Results show that in the plume released from the central-domain line

source, a full Gaussian profile of the mean concentration induces two inflection points, which result in the maximum production rate for the concentration variance, further leading to a dual-peak pattern in the RMS concentration profile in the wall-normal direction. However, for the plume released from the near-wall source, the plume shows one half of the Gaussian profile in the far downstream region of the source, and correspondingly, the RMS concentration profile exhibits a single-peak pattern.

In order to pinpoint the location where a plume emitted from a line source transitions from the turbulent convective stage to the turbulent diffusive stage, the pre-multiplied spectra of the velocity and concentration fields are compared. Because the elevations of these two line sources are different, there is an apparent difference in their streamwise plume development patterns. For the line source positioned near the channel center, the bulk meandering effects dominate the plume development over the entire computational domain. In contrast, for the line source positioned in the near-wall region, the streamwise development of the plume exhibits a more complex pattern. Immediately downstream of the near-wall line source, the plume size is small, and the plume development is dominated by the meandering effects. However, the plume from near-wall line source hits the ground soon after its release, and the plume spread becomes larger than the fine length scales of flow structures close to the wall, further leading to a transition from the turbulent convective stage to the turbulent diffusive stage.

7.1.2 DNS Study of Passive Plume Interference Emitting from Two Parallel Line Sources in a Turbulent Channel Flow

In this sub-project, the interference of two passive plumes emitting simultaneously from a ground-level and elevated line sources of various source separations is investigated using DNS. In the ground-level source release case, the mean concentration peaks at the wall, while in the elevated source release, the mean concentration value

first peaks at the source elevation immediately downstream of the source, and then the plume hits the ground and behaves as if it was emitted from a ground-level source in the far downstream region of the source. Results show that at a location very close to the elevated line source, a full Gaussian profile of the mean concentration presents briefly, which has two inflection points associated with the maximum production rates for the concentration variance. This further results in a dual-peak pattern in the RMS concentration profile in the physical space and also in the contours of the spanwise pre-multiplied spectrum of the concentration field (for a plume released from an elevated source sufficiently far from the wall). However, for the single plume released from the ground-level source, the plume shows only one half the Gaussian profile, and as a result, there is only one single peak in the RMS concentration profile. Although the mean concentration fields from the two line sources are superposable, the second-order statistical moments of concentration are not due to their nonlinear relationship. It is observed that the value of the co-variance of the dual plumes is the largest in case A, which has the smallest source separation among all three test cases and features the most intense interactions between the two instantaneous plumes.

In contrast to the previous studies [14; 32; 17], which focused exclusively on the lateral plume development in the homogeneous direction of the flow, there are new challenges involved in the present study which investigates the 2-D plume development emitting from a line source with the presence of wall anisotropy. In order to pinpoint the location where a single plume dispersion transitions from the turbulent convective stage to the turbulent diffusive stage, a new alternative approach based on a spectral analysis is proposed. The modes of the spanwise pre-multiplied spectra of the velocity and concentration fields are compared. At a given wall-normal position y^+, if the characteristic length scale of energetic eddy motions (as indicated by the mode $\lambda_{z,w'}^{m+}$ of the pre-multiplied spectrum of the spanwise velocity field) is larger than that of the plume (as indicated by the mode $\lambda_{z,c'}^{m+}$ of the pre-multiplied spectrum of the concentration field), the dispersion is considered to be at a turbulent convective stage;

otherwise, and the plume dispersion is considered to be at a turbulent diffusive stage. Results show that the plume emitting from a ground-level source transitions to the turbulent diffusive stage more rapidly than that from an elevated source.

It is observed that the mixing of two plumes varies significantly with the streamwise location and the source separation distance. The quality of mixing of two instantaneous plumes is studied using the cross-correlation function in the physical space, and the pre-multiplied co-spectrum and coherency spectrum in the spectral space. The mode of $f^*Co_{c_1'c_2'}$ decreases as the downstream distance from the line sources increases from $x/\delta = 1$ to 6, indicating an increasing characteristic scale of the dual-plume mixing. However, as the downstream distance further increases from $x/\delta = 6$ to 12, the mode of the pre-multiplied co-spectrum $f^*Co_{c_1'c_2'}$ is stabilized at a Strouhal number of approximately $f^* = 2$. It is observed that at near-source locations, the maximum coherency spectrum is produced at lower frequencies. This indicates that dual-plume mixing is dominated by the external flapping effects of large-scale eddy motions in the downstream regions near the two sources where the size of the plume is smaller than that of turbulent eddies. However, as the downstream distance reaches $x/\delta = 6$, the coherency spectrum in the higher frequency range increases significantly. The value of the coherency spectrum approaches to its asymptotic value of unity across the entire frequency space, indicating that the plume is already in the complete mixing state. At this turbulent diffusive stage of plume mixing, the plume size is larger than all scales of turbulent eddies of all frequencies, such that they all contribute to the process of internal plume mixing.

7.1.3 Study of Vertical Line Source Dispersion in a Turbulent Channel Flow

In this sub-project, turbulent dispersion of a passive plume emitting from a vertical line source in a fully-developed channel flow is studied using DNS. The plume devel-

opment is inhomogeneous spatially and the statistical moments of the concentration field vary significantly in all three directions. The transition of plume development from TCS to TDS is sensitive to not only the downstream distance from the line source but also the wall-normal distance. The phenomenon of similarity in the mean velocity profile of a round or slot jet is widely known. By analogy, it is very interesting to also observe a self-similarity in the non-dimensionalized mean concentration profile $\langle c \rangle_t / \langle c \rangle_{t,max}$, when it is scaled with a lateral coordinate ζ defined based on the concept of "half plume width" (where the mean concentration $\langle c \rangle_t$ drops to one half of its local maximum $\langle c \rangle_{t,max}$).

In order to understand the wall-anisotropic effects on the transition of plume development from TCS to TDS, a comparative study of the spatial and temporal scales of the turbulent velocity and concentration fields has been conducted systematically in both physical and spectral spaces. It is observed that the transition from TCS to TDS is continuous with respect to the wall-normal distance, and furthermore, the transition process becomes more rapid as the wall is approached. Also, as the wall is approached, the mean plume width σ_z increases, however, the spanwise characteristic scale of the flow structures (as indicated by the mode of the spatial premultiplied spectrum of spanwise velocity fluctuations $\lambda^+_{z,m}$) decreases monotonically. Both these factors facilitate a fast transition from TCS to TDS in the near-wall region.

Immediately downstream of the source, the pattern of plume dispersion is predominantly TCS. This is because the plume spread is much smaller than that of the energetic eddies in the region near the line source, and consequently, the mixing process of the concentration is dominated by the large meandering eddy motions of the fluid flow. However, as the downstream distance from the line source increases, the plume size grows and eventually exceeds that of large energetic eddies. Consequently, the motion of energetic eddies acts as in-plume mixing, enhancing turbulent diffusion of the concentration and the pattern of plume dispersion transitions from TCS to TDS. In fact, in the far downstream region (in the TDS region), the value

of meandering ratio M decreases significantly, indicating an enhanced turbulent diffusion and in-plume mixing mechanism by large energetic eddies. It is observed that the streamwise position (x/δ) for the transition to occur from TCS to TDS becomes increasingly delayed as the wall-normal distance increases (as the value of y^+ increases). Furthermore, the value of the meandering ratio M at the transition point also increases monotonically as the value of y^+ increases. This is because as the wall-normal distance increases, the strength of turbulent convection enhances, and consequently, the dispersion of the plume centroid increases monotonically.

It is observed that the PDF distribution is asymmetrical in the TCS zone, and tends to become symmetrical in the TDS zone. The reason for the PDF to be nearly Gaussian in a TDS zone is that the length scale of large eddies is smaller than that of the plume, and therefore, the flapping motion of large eddies contribute to the in-plume mixing of concentration. The flapping motions of eddies around the plume centroid result in equal chances of positive and negative concentration fluctuations in a TDS zone, leading to a Gaussian distribution of concentration fluctuations c'.

Besides the spatial scales, the temporal scales of the turbulent concentration field have also been studied through a spectral analysis. It is observed that the characteristic temporal scale $T^+_{c',m}$ (corresponding to the mode of the temporal premultiplied spectrum) of concentration fluctuations c' varies significantly in both streamwise and wall-normal directions. It is also observed that as the downstream distance x/δ increases, the characteristic time scale of concentration fluctuations increases monotonically. It is discovered that in the viscous sublayer, the value of $T^+_{c',m}$ increases initially, and then flattens out as x/δ further increases. This is because once the plume hits the wall, the turbulent dispersion of the scalar becomes stabilized in the near-wall region, exhibiting a self-similar pattern in the downstream region. It is also discovered that the temporal scale $T^+_{c',m}$ is the maximum near the wall, and decreases continuously and monotonically as the distance from the wall increases, eventually approaching an asymptotic value in the central region of the channel.

Finally, it should be indicated that the current DNS study of turbulent dispersion of a passive scalar in a turbulent plane-channel flow has concentrated on investigating the wall-anisotropic effects on the plume transition from TCS to TDS at a relatively low Reynolds number and a fixed Prandtl number. As is well known, the Reynolds number has a significant impact on near-wall streaks, hairpin structures, and interaction of vortices between the inner and outer regions of a turbulent boundary layer. The effects of Reynolds number and Prandtl number on turbulent transport process of concentration emitting from a vertical line source in a channel flow can be further examined in future studies.

7.1.4 Study of Turbulent Dispersion of Concentration Plume Emitting from a Line Source over a Rib-roughened Surface

In this sub-project, the effects of surface-mounted rib elements on turbulent dispersion of a concentration plume emitting from a ground-level or elevated spanwise line source have been investigated using DNS. Four line source positions are compared, including two ground-level source cases (GS1 and GS2), and two elevated source cases (ES1 and ES2). Common to the four test cases, the plume development is laterally homogeneous, but inhomogeneous in streamwise and vertical directions. It is observed that the development of the mean plume enters the long-range dispersion stage at a downstream distance of approximately $x/h \geq 12.0$, where a featured decay rate of the maximum mean concentration value ($\langle c \rangle_{\max}$) of a constant slope of $-3/2$ is observed. The vertical mean plume width is significantly influenced by the recirculation bubble leeward of the rib near the line source, especially for cases GS2 and ES2. The short- and long-range dispersion mechanisms also have a significant impact on the vertical spread of the mean plume, and it is observed that the vertical spread of the mean plume (σ_y) features a constant slope of $1/3$ in the long-range dispersion region for all

four test cases.

As the wall is approached, the flow convection effect reduces while the development of the plume becomes increasingly influenced by the turbulent diffusion mechanism. In all four test cases, the normalized mean concentration profiles $\langle c \rangle / \langle c \rangle_{max}$ exhibit a quasi Gaussian pattern. Furthermore, it is interesting to observe that the vertical profiles of the non-dimensionalized mean concentration value $\langle c \rangle / \langle c \rangle_{max}$ of different streamwise positions collapse if they are displayed with respect to a vertical coordinate non-dimensionalized by the half concentration spread $y_{_{1/2}}$. Also based on our previous study of turbulent plume dispersion in a smooth plane-channel flow, it concluded that the self-similarity in the vertical profile of a mean concentration field resulted from a line release is a quite robust property in the context of either a turbulent smooth plane-channel flow or a turbulent rib-roughened wall flow under current investigation.

It is seen that the difference in the vertical profiles of concentration RMS c_{rms} between different streamwise source positions is the most sensitive in the near-source position, but becomes insensitive in the far downstream region. It is observed that the transition of plume development from TCS to TDS is sensitive to the downstream distance from the line source, source elevation, and the presence of the rib elements. In order to understand the rib effects on the transition of plume development from TCS to TDS, a comparative study of the characteristic length scales of the turbulent velocity and concentration fields ($\lambda^m_{z,w'}$ and $\lambda^m_{z,c'}$, respectively) has been conducted systematically through a spectral analysis. Given the streamwise periodicity of the ribs, a quasi periodic pattern is observed in the profiles of both $\lambda^m_{z,w'}$ and $\lambda^m_{z,c'}$, especially at a lower elevation under the rib height. It is observed that plumes released from ground-level line sources transition from TCS to TDS more rapidly than do those released from elevated line sources in general. Furthermore, at a higher elevation at or above the rib height, the transition of the plume development from a TCS to a TDS stage becomes increasingly delayed (as the elevation increases). This is because the turbulent convection mechanism becomes increasingly dominant as the distance

from the ribbed wall increases.

The temporal characteristics of the turbulent concentration field were analyzed through the CDF of the instantaneous concentration field and PDF of the concentration fluctuations for ground-level line source case GS1 and elevated line source case ES2. The analysis was conducted by comparing the CDF and PDF profiles extracted at three selected points below or above the rib height against the ideal Gaussian distribution. It is observed that the CDF and PDF profiles resemble the Gaussian distribution at a TDS stage of plume development in a region far downstream of the line source or near the wall. By contrast, the CDF and PDF profiles deviate apparently from that of the Gaussian distribution at a near-source position, where the instantaneous plume development features a TCS stage. This is because the plume spread is much smaller than that of the energetic eddies of turbulence near the line source, and consequently, the mixing process of the concentration is dominated by instantaneous large meandering eddy motions of the fluid flow.

7.2 Future work

In future studies, the following topics are suggested:

- The DNS of turbulent flow and dispersion has been carried out in domains featuring spanwise homogeneity, as periodic boundary conditions are applied to the spanwise direction for both the velocity and concentration fields. As a possible future study, DNS of turbulent flow and dispersion in a duct with a rectangular cross section can be conducted. Different from the current test cases, turbulent flow and dispersion in a duct are intrinsically 3-D, with four boundary layers developing over four sidewalls of the duct which interact with each other as the velocity and concentration fields develop streamwise.

- In this thesis, the study of wall roughness on turbulent dispersion of a concentration plume is based on a k-type square-shaped rib bars. The d-type roughness

can be alternatively considered, and furthermore, rib elements of other cross-sectional shapes (such as circular and triangular bars) can be also considered in future studies.

- This thesis focuses on pollution problems, and therefore, a passive scalar transport process is studied. As a possible future research direction, the study can be expanded by considering the transport of active scalars, which may have different engineering application backgrounds of, e.g. a buoyant heat exchanger problem.

- All the domains of the test cases of this thesis are stationary. In future studies, it is possible to extend current applications to DNS or LES of the internal cooling problem of a gas turbine. As such, the rotating effects of the domain needs to be considered. In response to a system rotation, Coriolis forces appear which alter the turbulent transport processes of both momentum and passive concentrations.

Appendix A

Numerical Algorithm

In this appendix, the finite-volume method (FVM) for discretizing the continuity, Navier-Stokes and concentration equations based on collocated grids are presented.

A.1 Momentum equation

The transport process of a given quantity ($\phi \equiv u,\ v,\ w,$ or c) is governed by the following equations in the context of an incompressible flow:

$$\frac{\partial(\rho\phi)}{\partial t} + \text{ div } (\rho u_i \phi) = \text{ div}(\Omega \text{ grad } \phi) + S_\phi \tag{A.1}$$

where u_i represents the velocity, S_ϕ is the source term, ρ is the density of the fluid, and Ω represents the molecular diffusivity of the given quantity ϕ. By applying the FVM to the above transport equation, we obtain:

$$\underbrace{\oint \left\{ \int_t^{t+\Delta t} \frac{\partial(\rho\phi)}{\partial t} dt \right\} dV}_{\text{Temporal term}} + \underbrace{\int_t^{t+\Delta t} \left\{ \iint_A n_i \ (\rho u_i \phi) dA \right\} dt}_{\text{Convection term}}$$

$$= \underbrace{\int_t^{t+\Delta t} \left\{ \iint_A n_i (\Omega \text{ grad } \phi) dA \right\} dt}_{\text{Diffusion term}} + \underbrace{\int_t^{t+\Delta t} \oint S_\phi \ dV \ dt}_{\text{Source term}} \quad . \tag{A.2}$$

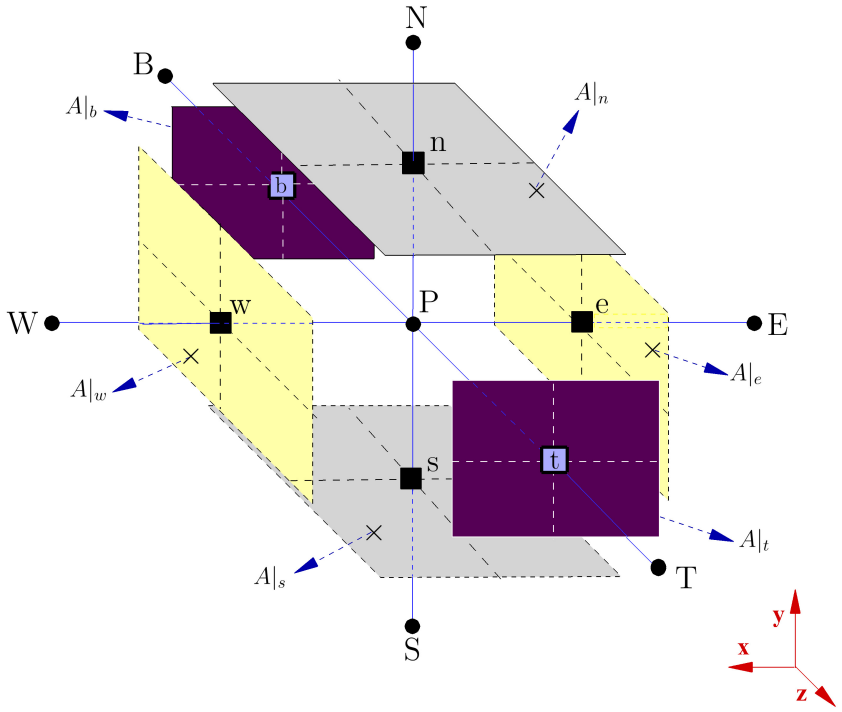

Figure A.1: A typical finite-volume cell with the central nodes (E, W, N, S, T, B, P) and face nodes (e, w, n, s, t, b). Faces of the cell are denoted as $A|_e$, $A|_w$, $A|_n$, $A|_s$, $A|_t$, and $A|_b$, respectively.

In the above equation, the temporal term, convection term, diffusion term, and the source term need to be discretized.

A.2 Central differencing scheme (CDS)

In this section, we apply the central differencing scheme (CDS) to the discretization of Eq. (A.2) The gradient of a given quantity (grad ϕ) can be computed by using the values of quantities on the neighbor's faces. For example, the face value corresponds to the east surface equals to the arithmetic average of the neighbor's nodes, such that $\phi|_e = \dfrac{\phi_E + \phi_P}{2}$. Here $\phi|_e$ is the face value of the surface $A|_e$, and ϕ_E, and ϕ_P are the values of a given quantity associated with the central nodes. Figure A.1 shows the cen-

tral nodes (E, W, N, S, T, B, P), and the nodes on the neighbor's faces (e, w, n, s, t, b). In addition, faces of the cell are denoted as $A|_e,\ A|_w,\ A|_n,\ A|_s,\ A|_t$, and $A|_b$, respectively.

Substitution of the above expressions into the convection- and diffusion- terms of Eq. (A.2) gives:

$$\begin{aligned}
\text{Convection terms}: \quad & \int_t^{t+\Delta t} \underbrace{\left\{ \oiint_A n_i\ (\rho u_i \phi) dA \right\}}_{\text{Spatial term}}\ dt \\
&= \int_t^{t+\Delta t} \underbrace{(\rho u A\phi)|_e - (\rho u A\phi)|_w}_{\text{Streamwise fluxes}}\ dt \\
&+ \int_t^{t+\Delta t} \underbrace{(\rho v A\phi)|_n - (\rho v A\phi)|_s}_{\text{Wall-normal fluxes}}\ dt \\
&+ \int_t^{t+\Delta t} \underbrace{(\rho w A\phi)|_t - (\rho w A\phi)|_b}_{\text{Lateral fluxes}}\ dt
\end{aligned}$$

$$\begin{aligned}
\text{Diffusion terms}: \quad & \int_t^{t+\Delta t} \underbrace{\left\{ \oiint_A n_i (\Omega \text{ grad } \phi) dA \right\}}_{\text{Spatial term}}\ dt \\
&= \int_t^{t+\Delta t} \underbrace{(\Omega A \frac{d\phi}{dx})|_e - (\Omega A \frac{d\phi}{dx})|_w}_{\text{Streamwise molecular diffusion}}\ dt \\
&+ \int_t^{t+\Delta t} \underbrace{(\Omega A \frac{d\phi}{dy})|_n - (\Omega A \frac{d\phi}{dy})|_s}_{\text{Wall-normal molecular diffusion}}\ dt \\
&+ \int_t^{t+\Delta t} \underbrace{(\Omega A \frac{d\phi}{dz})|_t - (\Omega A \frac{d\phi}{dz})|_b}_{\text{Lateral molecular diffusion}}\ dt
\end{aligned}$$

Here $(\cdot)|_.$ represents the value on the face. We denote $\rho u_i \phi|_.$ as the face value of convection and $\Omega A \frac{d\phi}{dx_i}|_.$ as the diffusion value on the face. Table A.1, summarizes

Table A.1: Diffusion and convection components.

The central differencing scheme (CDS)	
Convection terms	Diffusion terms
$\rho u A\phi\|_e \approx (\rho u A)\|_e(\frac{\phi_E+\phi_P}{2})$	$\Omega A\frac{d\phi}{dx}\|_e \approx \frac{(\Omega A)\|_e}{\delta x_{PE}}(\phi_E-\phi_P)$
$\rho u A\phi\|_w \approx (\rho u A)\|_w(\frac{\phi_W+\phi_P}{2})$	$\Omega A\frac{d\phi}{dx}\|_w \approx \frac{(\Omega A)\|_w}{\delta x_{PW}}(\phi_P-\phi_W)$
$\rho v A\phi\|_n \approx (\rho v A)\|_n(\frac{\phi_N+\phi_P}{2})$	$\Omega A\frac{d\phi}{dy}\|_n \approx \frac{(\Omega A)\|_n}{\delta y_{PN}}(\phi_N-\phi_p)$
$\rho v A\phi\|_s \approx (\rho v A)\|_s(\frac{\phi_S+\phi_P}{2})$	$\Omega A\frac{d\phi}{dy}\|_s \approx \frac{(\Omega A)\|_s}{\delta y_{PS}}(\phi_P-\phi_S)$
$\rho w A\phi\|_t \approx (\rho w A)\|_t(\frac{\phi_T+\phi_P}{2})$	$\Omega A\frac{d\phi}{dz}\|_t \approx \frac{(\Omega A)\|_t}{\delta z_{PT}}(\phi_T-\phi_P)$
$\rho w A\phi\|_b \approx (\rho w A)\|_b(\frac{\phi_B+\phi_P}{2})$	$\Omega A\frac{d\phi}{dz}\|_b \approx \frac{(\Omega A)\|_b}{\delta z_{PB}}(\phi_P-\phi_B)$

the convection and diffusion terms of the different faces shown in Fig. A.1. Substituting $(\rho u A)|. = F|.$ and $\frac{(\Omega A)|.}{\delta x_i} = D|.$ into the table A.1, we obtain both the convection and diffusion in terms of the surface fluxes, as is described in table A.2.

In the following, an algebraic equation will be derived, which contains the nodal value and gives ϕ_P^{New}. Such an equation can be written in form of $\frac{d\phi}{dt} = \varphi(x,y,z)$, where $\varphi(x,y,z)$ may be in a manner as follow:

$$\varphi(x,y,z) = \frac{1}{\rho\Delta V}\left[a_P\phi_P + \sum a_{nb}\phi_{nb} + S_\phi\right] \quad . \tag{A.3}$$

Here, ϕ_{nb} is a given quantity that corresponds to the neighbor nodes, and a_{nb} is the related coefficient. Such a description for these coefficients of LHS and RHS of Eq. A.2 are explained in table A.3, and table A.4. Note that the temporal- and source- terms are excluded. To obtain an algebraic equation in the form of Eq. A.3, the momentum equation can be rearranged as follow:

$$\frac{\partial(\rho\phi)}{\partial t} = \text{ div}(\Omega \text{ grad } \phi) - \text{ div } (\rho u_i\phi) + S_\phi \quad . \tag{A.4}$$

Table A.2: Diffusion and convection components.

The central differencing scheme (CDS)	
Convection terms $(\rho u A)\vert_. = F\vert_.$	Diffusion terms $(\frac{(\Omega A)\vert_.}{\delta x_.} = D\vert_.)$
$F\vert_e(\frac{\phi_E + \phi_P}{2})$	$D\vert_e(\phi_E - \phi_P)$
$F\vert_w(\frac{\phi_W + \phi_P}{2})$	$D\vert_w(\phi_P - \phi_W)$
$F\vert_n(\frac{\phi_N + \phi_P}{2})$	$D\vert_n(\phi_N - \phi_P)$
$F\vert_s(\frac{\phi_S + \phi_P}{2})$	$D\vert_s(\phi_P - \phi_S)$
$F\vert_t(\frac{\phi_T + \phi_P}{2})$	$D\vert_t(\phi_T - \phi_P)$
$F\vert_b(\frac{\phi_B + \phi_P}{2})$	$D\vert_b(\phi_P - \phi_B)$

Table A.3: LHS coefficient of Eq. (A.2), excluding the temporal terms.

The central differencing scheme (CDS)
Convection coefficients $(a \equiv F\vert_i)$
ϕ_P: $a_P \equiv (F\vert_e - F\vert_w + F\vert_n - F\vert_s + F\vert_t - F\vert_b)/2$
ϕ_E: $a_E \equiv F\vert_e/2$
ϕ_W: $a_W \equiv -F\vert_w/2$
ϕ_N: $a_N \equiv F\vert_n/2$
ϕ_S: $a_S \equiv -F\vert_s/2$
ϕ_T: $a_T \equiv F\vert_t/2$
ϕ_B: $a_B \equiv -F\vert_b/2$

Table A.5 provides an expression for the coefficients of a given quantity ϕ in Eq. A.4. Note that the source terms are excluded. The pressure gradient with the nodal values $p|_E$, $p|_W$, $p|_N$, $p|_S$, $p|_T$, and $p|_B$ are considered as the source terms here, and are configured under the rules associated with the pressure–velocity coupling, called collocated grid arrangement [69]. In CDS, the spatial discretizations of the pressure gradient are written in the table A.6. Finally, in regards to the face velocities,

Table A.4: RHS coefficient of Eq. (A.2), excluding the source term.

The central differencing scheme (CDS)
Diffusion coefficient ($a \equiv D\|_i$)
ϕ_P: $a_P \equiv -D\|_w - D\|_e - D\|_s - D\|_n - D\|_b - D\|_t$
ϕ_E: $a_E \equiv D\|_e$
ϕ_W: $a_W \equiv D\|_w$
ϕ_N: $a_N \equiv D\|_n$
ϕ_S: $a_S \equiv D\|_s$
ϕ_T: $a_T \equiv D\|_t$
ϕ_B: $a_B \equiv D\|_b$

Table A.5: RHS coefficient of Eq. (A.4), excluding the source term.

The central differencing scheme (CDS)
[Diffusion coefficient] - [Convection coefficient]: $a \equiv [D - F]\,\|_i$
ϕ_P: $a_P \equiv (\frac{-F}{2} - D)\|_e + (\frac{F}{2} - D)\|_w + (\frac{-F}{2} - D)\|_n + (\frac{F}{2} - D)\|_s + (\frac{-F}{2} - D)\|_t + (\frac{F}{2} - D)\|_b$
ϕ_E: $a_E \equiv (\frac{-F}{2} + D)\|_e$
ϕ_W: $a_W \equiv (\frac{F}{2} + D)\|_w$
ϕ_N: $a_N \equiv (\frac{-F}{2} + D)\|_n$
ϕ_S: $a_S \equiv (\frac{F}{2} + D)\|_s$
ϕ_T: $a_T \equiv (\frac{-F}{2} + D)\|_t$
ϕ_B: $a_B \equiv (\frac{F}{2} + D)\|_b$

consider the momentum interpolation. For example an approximation for $u|_e$ has been described in table A.7. The uniform grid is assumed.

Table A.6: Source terms in Eq. (A.4).

The central differencing scheme (CDS)
$\frac{-\partial p}{\partial x_i}$
Source term: $\int_t^{t+\Delta t} \oint S_\phi \, dV \, dt = V \int_t^{t+\Delta t} S_\phi \, dt$
Source term for x momentum: $\int_t^{t+\Delta t} (A\|_w \, \frac{p\|_W + p\|_P}{2}) - (A\|_e \, \frac{p\|_E + p\|_P}{2}) \, dt$
Source term for y momentum: $\int_t^{t+\Delta t} (A\|_s \, \frac{p\|_S + p\|_P}{2}) - (A\|_n \, \frac{p\|_N + p\|_P}{2}) \, dt$
Source term for z momentum: $\int_t^{t+\Delta t} (A\|_b \, \frac{p\|_B + p\|_P}{2}) - (A\|_t \, \frac{p\|_T + p\|_P}{2}) \, dt$

Table A.7: Illustration of the face velocity. UD stands for Upwind differencing, and CD stands for Central differencing.

The momentum interpolation for collocated grid arrangement
$u\|_e = f(u_P, u_E, \frac{\partial p}{\partial x}\|_P, \frac{\partial p}{\partial x}\|_E)$
$u\|_e = (\frac{u_P + u_E}{2}) - \left\{ d\|_e \times \frac{\partial p}{\partial x}\|_E^{UD} - 0.5 d\|_e \times (\frac{\partial p}{\partial x}\|_P^{CD} + \frac{\partial p}{\partial x}\|_E^{CD}) \right\} + \Upsilon$
$\frac{\partial p}{\partial x}\|_E^{UD} = \frac{p_E - p_P}{\delta x}$
$\frac{\partial p}{\partial x}\|_P^{CD} = \frac{p_E - p_W}{2\delta x}$
$\frac{\partial p}{\partial x}\|_E^{CD} = \frac{p_{EE} - p_P}{2\delta x}$
$\Upsilon = \frac{\rho d\|_e}{\Delta t} \times \{ u\|_e^{OLD} - 0.5(u_P + u_E) \}$
$d\|_e = \frac{K}{(1 + (\rho K/\Delta t))}, \quad K = 0.5(\frac{V}{a_{P_P}} + \frac{V}{a_{P_E}}),$

Gathering the calculated coefficients for pressure, diffusion, and convection terms from tables A.6,and A.5, and with the face value for the velocity (table A.7), the rearranged algebraic equation may be solved for ϕ_P by using the explicit- or implicit- temporal

scheme such as the Richtmyer/Lax-Wendroff multi-step method, the MacCormack method, the Euler method, the Runge-Kutta method, the Crank-Nicolson scheme, and the beam and warming implicit method.

A.3 Pressure correction

In this section, the Poisson equation for solving the pressure field is derived. Recall from Sec. A.1 that the partial differential equation for the velocity field in such an orthogonal coordinate is given by Eq. (A.1), repeated below:

$$\frac{\partial(\rho\phi)}{\partial t} + \text{ div } (\rho u_i \phi) = \text{ div}(\Omega \text{ grad } \phi) + S_\phi \quad . \tag{8.5}$$

If S_ϕ is the unknown pressure source function of $(x, y, z, \ t)$, then Eq. A.1 can be solved without this term to yield the candidate velocity field $\vec{u}^{New}$ as follow:

$$\frac{\partial(\rho\vec{u})}{\partial t} + \ \rho\vec{u}.\nabla\vec{u} = \mu\nabla^2\vec{u} \Rightarrow \vec{u}^{New} = \vec{u} + \Delta t \left\{\nu\nabla^2\vec{u} - \vec{u}.\nabla\vec{u}\right\} \quad . \tag{A.5}$$

Here $\vec{u}$ is the velocity vector at the time t_1, $\vec{u} = u\vec{i} + v\vec{j} + w\vec{k}$, $\vec{u}^{New}$ is the candidate velocity vector at the time t_2, ∇ is the gradient operator $\nabla = \frac{\partial}{\partial x}\vec{i} + \frac{\partial}{\partial y}\vec{j} + \frac{\partial}{\partial z}\vec{k}$, ∇^2 is the Laplace operator $\nabla\cdot\nabla(\cdot) = \frac{\partial^2}{\partial x^2}(\cdot) + \frac{\partial^2}{\partial y^2}(\cdot) + \frac{\partial^2}{\partial z^2}(\cdot)$, and ν is called the kinematic viscosity of the fluid. The candidate velocity $\vec{u}^{New}$ has been obtained by considering the viscous force term only. Hence it does not satisfy the mass conservation:

$$\nabla\cdot(\vec{u}^{New}) = \nabla\cdot(\vec{u} + \Delta t \left\{\nu\nabla^2\vec{u} - \vec{u}\cdot\nabla\vec{u}\right\}) \neq 0.0 \quad . \tag{A.6}$$

There should be a certain pressure field of the function $(x, \ y, \ z, \ t)$, in which we may get $\nabla\cdot(\vec{u}^{New}) = 0.0$. We call this terms the pressure correction field $p' = f(x, y, z, \ t)$. Let us define the characteristics of this scalar field. Adding $(-\frac{\Delta t}{\rho} \ \nabla p')$ into Eq. A.5, we obtain the original form of the Navier stokes equation:

$$\vec{u}^{New} - \frac{\Delta t}{\rho} \ \nabla p' = (\vec{u} + \Delta t \left\{\nu\nabla^2\vec{u} - \vec{u}\cdot\nabla\vec{u}\right\}) - \frac{\Delta t}{\rho} \ \nabla p' \quad . \tag{A.7}$$

Since the above definition considers all required forces in Newton's second law of motion, it yields the correct velocity field such that:

$$\nabla \cdot (\vec{u}^{New}) - \frac{\Delta t}{\rho} \nabla \cdot (\nabla p') = 0.0 \quad , \tag{A.8}$$

rearranging this we obtain:

$$\nabla^2 \, p' = \frac{\rho}{\Delta t} \nabla \cdot (\vec{u}^{New}) \quad . \tag{A.9}$$

Then, for an incomprehensible flow, the pressure field's characteristics are defined by the Poisson equation, where the source term is the divergence of the velocity field. By applying Gauss's divergence theorem to Eq. (A.9) we obtain:

$$\underbrace{\oiint_A n_i \text{ grad } p' dA}_{\nabla^2 \, p'} = \frac{\rho}{\Delta t} \underbrace{\oiint_A n_i \, (\vec{u}^{New}) \, dA}_{\nabla \cdot (\vec{u}^{New})} \quad , \tag{A.10}$$

where $\nabla^2 \, p'$ is the scalar field of function $x, \; y, \; z$ and includes streamwise, wall-normal, and lateral pressure gradient as follow:

$$\begin{aligned} \nabla^2 \, p' &= \oiint_A n_i \text{ grad } p^{'} dA \\ &= \underbrace{A\frac{dp'}{dx}|_e - A\frac{dp'}{dx}|_w}_{\text{Streamwise pressure gradient}} \\ &+ \underbrace{A\frac{dp'}{dy}|_n - A\frac{dp'}{dy}|_s}_{\text{Wall-normal pressure gradient}} \\ &+ \underbrace{A\frac{dp'}{dz}|_t - A\frac{dp'}{dz}|_b}_{\text{Lateral pressure gradient}} \end{aligned}$$

Here $(\cdot)|_.$ represents the value on the face. We denote $\frac{dp'}{d\cdot}|_.$ as the face value of the pressure gradient, and can be discretized by applying CDS scheme. Table A.8, summarizes the pressure gradient of the surrounded faces.

Table A.8: LHS terms in Poisson equation Eq. (A.10).

Use of CDS for pressure correction terms
$$A\frac{dp'}{dx}\|_e \approx \frac{A\|_e}{\delta x_{PE}}(p'_E - p'_P)$$
$$A\frac{dp'}{dx}\|_w \approx \frac{A\|_w}{\delta x_{PW}}(p'_P - p'_W)$$
$$A\frac{dp'}{dy}\|_n \approx \frac{A\|_n}{\delta y_{PN}}(p'_N - p'_p)$$
$$A\frac{dp'}{dy}\|_s \approx \frac{A\|_s}{\delta y_{PS}}(p'_P - p'_S)$$
$$A\frac{dp'}{dz}\|_t \approx \frac{A\|_t}{\delta z_{PT}}(p'_T - p'_P)$$
$$A\frac{dp'}{dz}\|_b \approx \frac{A\|_b}{\delta z_{PB}}(p'_P - p'_B)$$

Table A.9: Algebraic pressure equation.

$$\nabla^2\ p' = \frac{\rho}{\Delta t}\ \nabla\cdot(\vec{u}^{New})$$
$$a_P p'_P = \sum a_{nb} p'_{nb} + S_{p'}$$
$$a_E = \frac{A\|_e}{\delta x_{PE}},\quad a_W = \frac{A\|_w}{\delta x_{PW}},\quad a_N = \frac{A\|_n}{\delta y_{PN}},\quad a_S = \frac{A\|_s}{\delta y_{PS}},\quad a_T = \frac{A\|_t}{\delta z_{PT}},\quad a_B = \frac{A\|_b}{\delta z_{PB}}$$
$$a_P = \sum a_{nb}$$
$$S_{p'} = \frac{1}{\Delta t}\left\{(\rho uA\|_w - \rho uA\|_e) + (\rho uA\|_s - \rho uA\|_n) + (\rho uA\|_b - \rho uA\|_t)\right\}$$

Accumulating the calculated coefficients for p'_E,, p'_W, p'_N, p'_S, p'_T, p'_B, and divergence terms from tables A.9, and with the face value for the velocity (table A.7), the rearranged algebraic equation can be solved for p'_P by using the explicit- or implicit-spatial scheme such as the Jacobi iteration method, the point Gauss-Seidel iteration method, the line Gauss-Seidel iteration method, point successive over-relaxation method (PSOR), line successive over-relaxation method (LSOR), and the alternating direction implicit method (ADI) .

A.4 Updating the velocity and pressure fields

Solving the pressure correction equation (Eq. A.10) provides an accurate and updated pressure field :

$$p^{\text{updated}}(x,y,z) = p(x,y,z) + p'(x,y,z) \quad . \tag{A.11}$$

As correcting the pressure field, the velocity field must be updated. To do so, we consider the below equation, where $u^{\text{Navier–Stokes}}$ is the velocity field obtained from Eq. A.4, and p denotes the updated pressure field defined by Eq. A.11 :

$$\rho\frac{\partial u}{\partial t} = -\frac{dp}{dx} \rightarrow u^{\text{updated}} - u^{\text{Navier–Stokes}} = \frac{-\Delta t}{\rho}\frac{\Delta p}{\Delta x} \quad . \tag{A.12}$$

If this equation is written for $u|_e$, the updated face velocity will be:

$$u|_e^{\text{updated}} = u|_e^{\text{Navier–Stokes}} + \frac{\Delta t}{\rho}\frac{p_P^{\text{updated}} - p_E^{\text{updated}}}{\delta x_{PE}} \quad ,$$

where $\dfrac{\Delta t}{\rho}\dfrac{p_P^{\text{updated}} - p_E^{\text{updated}}}{\delta x_{PE}}$ is called $u|_e^*$ in the literature.

A.5 Transport equation for the scalar

A.5.1 Central differencing scheme (CDS)

The transport equation for the instantaneous concentration field c can be written as:

$$\frac{\partial(c)}{\partial t} = \text{ div}(\alpha \text{ grad } c) - \text{ div } (u_i c) + S_c \quad . \tag{A.13}$$

Table A.10: Algebraic coefficient for the scalar field.

CDS for one-dimensional passive scalar field, $F =$ constant and positive, $D =$ constant
$c_P = 0.0; \quad a_P \equiv (\frac{-F}{2} - D)\|_e + (\frac{F}{2} - D)\|_w = -2D$ $c_E = 1.0; \quad a_E \equiv (\frac{-F}{2} + D)\|_e = \frac{-F}{2} + D$ $c_W = 0.0; \quad a_W \equiv (\frac{F}{2} + D)\|_w = \frac{F}{2} + D$

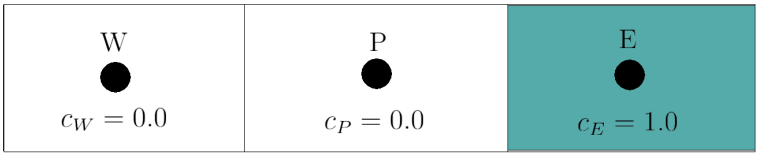

Figure A.2: An example of a control volume when one single adjacent node is of interest.

Consider the diffusion and convection coefficients for a one-dimensional problem, as defined in Table A.10. The values of the concentration c are imposed as $c_W = 0.0$, $c_P = 0.0$, and $c_E = 1.0$ for the nodes W, P, and E, respectively. This is shown in Fig. A.2. Gathering the calculated coefficients for the diffusion, and convection terms from table A.10, and with the pre-defined values for $\Delta t = 0.001s, \rho = 1.0\ Kg/m^3$, $\Delta V = 0.05\ m^3$, $F = 1.0\ Kg/s$, $D = 0.004\ Kg/s$, $a_E = -0.496$, $a_W = 0.504$, and $a_P = -0.008$ the rearranged algebraic equation can be solved for c_P^{New}:

$$c_P^{New} - c_P = \frac{\Delta t}{\rho \Delta V}[a_P c_P + a_E c_E + a_W c_W]$$

$$c_P^{New} - 0.0 = \frac{\Delta t}{\rho \Delta V}[(a_P \times 0.0) + (a_E \times 1.0) + (a_W \times 0.0)]$$

$$c_P^{New} = \frac{\Delta t}{\rho \Delta V}[(a_E \times 1.0)] = \frac{\Delta t}{\rho \Delta V}(\frac{-F}{2} + D) = -0.00992 \text{ (or Negative mass)} < 0.0$$

The use of CDS results in the negative unrealistic mass, immediately after one

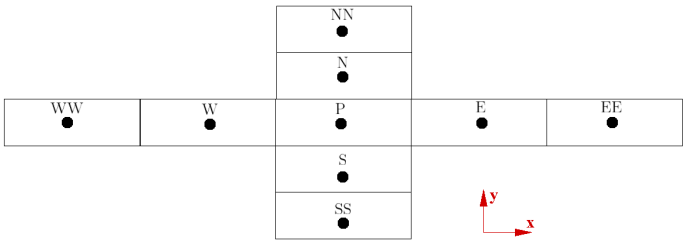

Figure A.3: An example of a control volume when two adjacent nodes are of interest.

time step ☹. Recalculate the algebraic equation with the new nodal values $c_W = 0.5,\ c_P = 0.0$, and $c_E = 1.0$, we obtain:

$$c_P^{New} - 0.0 = \frac{\Delta t}{\rho \Delta V}[(a_P \times 0.0) + (a_E \times 1.0) + (a_W \times 0.5)] \quad .$$

$$c_P^{New} = \frac{\Delta t}{\rho \Delta V}[(a_E \times 1.0) + (a_W \times 0.5)] = \frac{\Delta t}{\rho \Delta V}(\frac{-F}{4} + \frac{3D}{2}) = -0.244 < 0.0$$

The above calculation denotes that as the point P is surrounded by the positive concentration field, it will experience the high negative value of mass $c_P^{New} \ll 0.0$, if and only if $c_P = 0.0$. Again, recalculate the algebraic equation with the new nodal values $c_W = 1.0,\ c_P = 0.9$, and $c_E = 0.5$, we obtain:

$$c_P^{New} = \frac{\Delta t}{\rho \Delta V}[(a_P \times 0.9) + (a_E \times 0.5) + (a_W \times 1.0)] = \ 0.2488 \text{ (Realistic mass)} > 0.0$$

The results show that the use of CDS to solve the instantaneous concentration field when dealing with a sharp gradient will cause a negative unrealistic mass. As such, from the above three examples, $r = \dfrac{c_P - c_W}{c_E - c_P}$ is clearly a parameter that can cause the negative mass.

A.5.2 Limiter function of Van Albada

In this study, the total variation diminishing scheme (TVD) scheme (or, the limiter function) of Van Albada [50], $\Psi(r) = \dfrac{r + r^2}{1 + r^2}$, has been used for discretizing the convection term. This is to facilitate the capture of the plume edge, which typically has a sharp concentration gradient. Here r denotes the ratio of upwind-side gradient

Table A.11: Algebraic coefficient for the second order TVD scheme.

[Diffusion coefficient] - [Convection coefficient]: $a \equiv [D-F]\,\vert_i$
c_P: $a_P \equiv -1.0 \times [a_W + a_E + a_N + a_S + a_T + a_B + (F\vert_e - F\vert_w) + (F\vert_n - F\vert_s) + (F\vert_t - F\vert_b)]$
c_E: $a_E \equiv max(-F\vert_e, 0) + D\vert_e$
c_W: $a_W \equiv max(F\vert_w, 0) + D\vert_w$
c_N: $a_N \equiv max(-F\vert_n, 0) + D\vert_n$
c_S: $a_S \equiv max(F\vert_s, 0) + D\vert_s$
c_T: $a_T \equiv max(-F\vert_t, 0) + D\vert_t$
c_B: $a_B \equiv max(F\vert_b, 0) + D\vert_b$

to downwind-side gradient $r = \dfrac{c_P - c_W}{c_E - c_P}$. Consider the rearranged transport equation for the passive scalar field $c(x, y, z, t)$:

$$\frac{\partial(c)}{\partial t} = \text{ div}(\alpha \text{ grad } c) - \text{ div } (u_i c) + S_c \quad . \tag{A.14}$$

Rearranging the above equation into $\dfrac{\partial c}{\partial t} = \dfrac{1}{\Delta V}\left[a_P c_P + \sum a_{nb} c_{nb} + S_c\right]$, the related convection and diffusion coefficients can be obtained from table A.11. Note that in defining the convection coefficient, the UD scheme is used. For the source term, we see below the concentration gradient that they involve the limiter function of TVD. From this, we see that, unlike CDS, a knowledge of neighbor nodes (E, W, N, S, T, B) are not sufficient to obtain the limiter function; we also need the information of two nearby nodes (EE, WW, NN, SS, TT, BB). Figure A.3 shows the configuration of two nearby nodes in x and y directions.

In final, summing of calculated coefficients with the limiter TVD function of Val Albada, the rearranged algebraic equation $\dfrac{\partial c}{\partial t} = \dfrac{1}{\Delta V}\left[a_P c_P + \sum a_{nb} c_{nb} + S_c\right]$ may be solved for c_P by using the explicit- or implicit- temporal scheme such as the Richtmyer/Lax-Wendroff multi-step method, the MacCormack method, the Euler method, the Runge-Kutta method, the Crank-Nicolson scheme, and the beam and warming implicit method.

$$\text{Source term for the scalar field: } S_c = \frac{F|_e}{2}[(1-\gamma|_e)\Psi(r|_e^-) - \gamma|_e.\Psi(r|_e^+)](c_E - c_P)$$
$$+ \frac{F|_w}{2}[-(1-\gamma|_w)\Psi(r|_w^-) + \gamma|_w.\Psi(r|_e^+)](c_P - c_W)$$
$$+ \frac{F|_n}{2}[(1-\gamma|_n)\Psi(r|_n^-) - \gamma|_n.\Psi(r|_n^+)](c_N - c_P)$$
$$+ \frac{F|_s}{2}[-(1-\gamma|_s)\Psi(r|_s^-) + \gamma|_s.\Psi(r|_n^+)](c_P - c_S)$$
$$+ \frac{F|_t}{2}[(1-\gamma|_t)\Psi(r|_t^-) - \gamma|_t.\Psi(r|_t^+)](c_T - c_P)$$
$$+ \frac{F|_b}{2}[-(1-\gamma|_b)\Psi(r|_b^-) + \gamma|_b.\Psi(r|_t^+)](c_P - c_B)$$

$$r|_e^- = \frac{c_{EE} - c_E}{c_E - c_P} \qquad r|_e^+ = \frac{c_P - c_W}{c_E - c_P} \qquad r|_w^- = \frac{c_E - c_P}{c_P - c_W} \qquad r|_w^+ = \frac{c_W - c_{WW}}{c_P - c_W}$$
$$r|_n^- = \frac{c_{NN} - c_N}{c_N - c_P} \qquad r|_n^+ = \frac{c_P - c_S}{c_N - c_P} \qquad r|_s^- = \frac{c_N - c_P}{c_P - c_S} \qquad r|_s^+ = \frac{c_S - c_{SS}}{c_P - c_S}$$
$$r|_t^- = \frac{c_{TT} - c_T}{c_T - c_P} \qquad r|_t^+ = \frac{c_P - c_B}{c_T - c_P} \qquad r|_b^- = \frac{c_T - c_P}{c_P - c_B} \qquad r|_b^+ = \frac{c_B - c_{BB}}{c_P - c_B}$$

$$\gamma|_w = 1.0 \; For \; F|_w > 0.0 \; and \; \gamma|_e = 1.0 \; For \; F|_e > 0.0$$
$$\gamma|_w = 0.0 \; For \; F|_w < 0.0 \; and \; \gamma|_e = 0.0 \; For \; F|_e < 0.0$$
$$\gamma|_s = 1.0 \; For \; F|_s > 0.0 \; and \; \gamma|_n = 1.0 \; For \; F|_n > 0.0$$
$$\gamma|_s = 0.0 \; For \; F|_s < 0.0 \; and \; \gamma|_n = 0.0 \; For \; F|_n < 0.0$$
$$\gamma|_b = 1.0 \; For \; F|_b > 0.0 \; and \; \gamma|_t = 1.0 \; For \; F|_t > 0.0$$
$$\gamma|_b = 0.0 \; For \; F|_b < 0.0 \; and \; \gamma|_t = 0.0 \; For \; F|_t < 0.0$$

Bibliography

[1] J. Kim, P. Moin, and R. Moser, "Turbulence statistics in fully developed channel flow at low Reynolds number," *J. Fluid Mech.*, vol. 177, pp. 133–166, 1987.

[2] D. B. De Graaff and J. K. Eaton, "Reynolds-number scaling of the flat-plate turbulent boundary layer," *J. Fluid Mech.*, vol. 422, pp. 319–346, 2000.

[3] B. L. Sawford and H. Stapountzis, "Concentration fluctuations according to fluctuating plume models in one and two dimensions," *Boundary-Layer Meteorol.*, vol. 37, no. 1-2, pp. 89–105, 1986.

[4] Z. Warhaft, "The interference of thermal fields from line sources in grid turbulence," *J. Fluid Mech.*, vol. 144, pp. 363–387, 1984.

[5] A. S. Monin and A. M. Yaglom, "Statistical fluid mechanics: Mechanics of turbulence.," 1975.

[6] A. L. Kistler, "Measurement of joint probability in turbulent dispersion of heat from two line sources," tech. rep., Johns Hopkins Univ. Baltimore M. D., 1956.

[7] G. I. Taylor, "I. Eddy motion in the atmosphere," *Philos. Trans. R. Soc. Lond. A*, vol. 215, no. 523-537, pp. 1–26, 1915.

[8] H. Stapountzis, B. L. Sawford, J. C. R. Hunt, and R. E. Britter, "Structure of the temperature field downwind of a line source in grid turbulence," *J. Fluid Mech.*, vol. 165, pp. 401–424, 1986.

[9] G. I. Taylor, "Diffusion by continuous movements," *Proc. Lond. Math. Soc.*, vol. 2, no. 1, pp. 196–212, 1921.

[10] L. F. Richardson, "I. Some measurements of atmospheric turbulence," *Philos. Trans. R. Soc. Lond. A*, vol. 221, no. 582-593, pp. 1–28, 1921.

[11] M. S. Uberoi and S. Corrsin, "Diffusion from a line source in isotropic turbulence," *Proc. R. Soc. Lond. A*, vol. 151, pp. 465–478, 1935.

[12] U. Karnik and S. Tavoularis, "Measurements of heat diffusion from a continuous line source in a uniformly sheared turbulent flow," *J. Fluid Mech.*, vol. 202, pp. 233–261, 1989.

[13] B. I. Shraiman and E. D. Siggia, "Scalar turbulence," *Nature*, vol. 405, no. 6787, pp. 639–646, 2000.

[14] M. S. Anand and S. B. Pope, "Diffusion behind a line source in grid turbulence," *Turbulent Shear Flows 4. Eds. Bradbury, L. J. S., Durst, F., Launder, B. E., Schmidt, F.W. and Whitelaw J. H.*, pp. 46–52, 1985.

[15] D. Ahlman, G. Brethouwer, and A. V. Johansson, "Direct numerical simulation of a plane turbulent wall-jet including scalar mixing," *Phys. Fluids*, vol. 19, no. 6, pp. 65–102, 2007.

[16] P. K. Yeung, "Lagrangian characteristics of turbulence and scalar transport in direct numerical simulations," *J. Fluid Mech.*, vol. 427, pp. 241–274, 2001.

[17] S. N. Oskouie, Z. Yang, and B.-C. Wang, "Study of passive plume mixing due to two line source emission in isotropic turbulence," *Phys. Fluids*, vol. 30, no. 7, p. 075105, 2018.

[18] B. J. Daly and F. H. Harlow, "Transport equations in turbulence," *Phys. Fluids*, vol. 13, no. 11, pp. 2634–2649, 1970.

[19] C. Vanderwel and S. Tavoularis, "Measurements of turbulent diffusion in uniformly sheared flow," *J. Fluid Mech.*, vol. 754, pp. 488–514, 2014.

[20] H. Abe, R. A. Antonia, and H. Kawamura, "Correlation between small-scale velocity and scalar fluctuations in a turbulent channel flow," *J. Fluid Mech.*, vol. 627, pp. 1–32, 2009.

[21] R. A. Antonia, H. Abe, and H. Kawamura, "Analogy between velocity and scalar fields in a turbulent channel flow," *J. Fluid Mech.*, vol. 628, pp. 241–268, 2009.

[22] A. Noormohammadi and B.-C. Wang, "Numerical study of plume emission from a line source in a wall-bounded flow," *Int. J. Num. Meth. Heat Fluid Flow*, vol. 30, no. 7, pp. 2971–2987, 2019.

[23] A. Noormohammadi and B.-C. Wang, "DNS study of passive plume interference emitted from two parallel line sources in a turbulent channel flow," *Int. J. Heat Fluid Flow*, vol. 30, no. 7, pp. 202–216, 2019.

[24] A. Noormohammadi and B.-C. Wang, "Study of vertical line source dispersion in a turbulent channel flow," *Int. J. Heat Mass Transf.*, vol. 177, p. 121439, 2021.

[25] U. Karnik and S. Tavoularis, "Measurements of heat diffusion from a continuous line source in a uniformly sheared turbulent flow," *J. Fluid Mech.*, vol. 202, pp. 233–261, 1989.

[26] D. Ahlman, G. Brethouwer, and A. V. Johansson, "Direct numerical simulation of a plane turbulent wall-jet including scalar mixing," *Phys. Fluids*, vol. 19, no. 6, pp. 65–102, 2007.

[27] V. Eswaran and S. Pope, "Direct numerical simulations of the turbulent mixing of a passive scalar," *Phys. Fluids*, vol. 31, no. 3, pp. 506–520, 1988.

[28] A. Juneja and S. B. Pope, "A DNS study of turbulent mixing of two passive scalars," *Phys. Fluids*, vol. 8, no. 8, pp. 2161–2184, 1996.

[29] R. A. Lavertu and L. Mydlarski, "Scalar mixing from a concentrated source in turbulent channel flow," *J. Fluid Mech.*, vol. 528, pp. 135–172, 2005.

[30] E. Costa-Patry and L. Mydlarski, "Mixing of two thermal fields emitted from line sources in turbulent channel flow," *J. Fluid Mech.*, vol. 609, pp. 349–375, 2008.

[31] A. J. Vrieling and F. T. M. Nieuwstadt, "Turbulent dispersion from nearby point sources-interference of the concentration statistics," *Atmos. Environ.*, vol. 37, no. 32, pp. 4493–4506, 2003.

[32] S. N. Oskouie, B.-C. Wang, and E. Yee, "Study of the interference of plumes released from two near-ground point sources in an open channel," *Int. J. Heat Fluid Flow*, vol. 55, pp. 9–25, 2015.

[33] S. N. Oskouie, B.-C. Wang, and E. Yee, "Numerical study of dual-plume interference in a turbulent boundary layer," *Boundary-Layer Meteorol.*, vol. 164, no. 3, pp. 419–447, 2017.

[34] V. B. L. Boppana, Z.-T. Xie, and I. P. Castro, "Large-eddy simulation of dispersion from line sources in a turbulent channel flow," *Flow, Turb. Combust.*, vol. 88, no. 3, pp. 311–342, 2012.

[35] M. Davidson, K. Mylne, C. Jones, J. Phillips, R. Perkins, J. C. H. Fung, and J. Hunt, "Plume dispersion through large groups of obstacles—a field investigation," *Atmos. Environ.*, vol. 29, no. 22, pp. 3245–3256, 1995.

[36] R. Macdonald, R. Griffiths, and S. Cheah, "Field experiments of dispersion through regular arrays of cubic structures," *Atmos. Environ.*, vol. 31, no. 6, pp. 783–795, 1997.

[37] E. Yee and C. A. Biltoft, "Concentration fluctuation measurements in a plume

dispersing through a regular array of obstacles," *Boundary-Layer Meteorol.*, vol. 111, no. 3, pp. 363–415, 2004.

[38] G. T. Johnson and L. J. Hunter, "A numerical study of dispersion of passive scalars in city canyons," *Boundary-Layer Meteorol.*, vol. 75, no. 3, pp. 235–262, 1995.

[39] D. A. Paterson and C. J. Apelt, "Computation of wind flows over three-dimensional buildings," vol. 24, no. 3, pp. 193–213, 1986.

[40] D. Paterson and C. Apelt, "Simulation of wind flow around three-dimensional buildings," *Build Environ.*, vol. 24, no. 1, pp. 39–50, 1989.

[41] J.-F. Sini, S. Anquetin, and P. G. Mestayer, "Pollutant dispersion and thermal effects in urban street canyons," *Atmos. Environ.*, vol. 30, no. 15, pp. 2659–2677, 1996.

[42] J.-J. Kim and J.-J. Baik, "A numerical study of thermal effects on flow and pollutant dispersion in urban street canyons," *J. Appl. Meteorol.*, vol. 38, no. 9, pp. 1249–1261, 1999.

[43] B.-C. Wang, E. Yee, and F.-S. Lien, "Numerical study of dispersing pollutant clouds in a built-up environment," *Int. J. Heat Fluid Flow*, vol. 30, no. 1, pp. 3–19, 2009.

[44] C. G. Speziale, "On nonlinear k-l and k-ε models of turbulence," *J. Fluid Mech.*, vol. 178, pp. 459–475, 1987.

[45] A. Walton, A. Cheng, and W. Yeung, "Large-eddy simulation of pollution dispersion in an urban street canyon—part i: comparison with field data," *Atmos. Environ.*, vol. 36, no. 22, pp. 3601–3613, 2002.

[46] A. Walton and A. Cheng, "Large-eddy simulation of pollution dispersion in an urban street canyon—part ii: idealised canyon simulation," *Atmos. Environ.*, vol. 36, no. 22, pp. 3615–3627, 2002.

[47] M. Saeedi and B.-C. Wang, "Large-eddy simulation of turbulent flow and dispersion over a matrix of wall-mounted cubes," *Phys. Fluids*, vol. 27, no. 11, p. 115104, 2015.

[48] E. Yee, R. M. Gailis, A. Hill, T. Hilderman, and D. Kiel, "Comparison of wind-tunnel and water-channel simulations of plume dispersion through a large array of obstacles with a scaled field experiment," *Boundary-Layer Meteorol.*, vol. 121, no. 3, pp. 389–432, 2006.

[49] A. Noormohammadi and B.-C. Wang, "Study of turbulent dispersion of concentration plume emitting from a line source over a rib-roughened surface," *Int. J. Heat Mass Transf.*, vol. 195, p. 123132, 2022.

[50] G. D. van Albada, B. van Leer, and W. W. Roberts Jr., "A comparative study of computational methods in cosmic gas dynamics," *Proc. London Math. Soc.*, vol. 108, pp. 76–84, 1982.

[51] X. Fang, Z. Yang, B.-C. Wang, M. F. Tachie, and D. J. Bergstrom, "Large-eddy simulation of turbulent flow and structures in a square duct roughened with perpendicular and v-shaped ribs," *Phys. Fluids*, vol. 29, no. 6, p. 065110, 2017.

[52] S. Mahmoodi-Jezeh and B.-C. Wang, "Direct numerical simulation of turbulent flow through a ribbed square duct," *J. Fluid Mech.*, vol. 900, A18, 2020.

[53] S. Mahmoodi-Jezeh and B.-C. Wang, "Direct numerical simulation of turbulent duct flow with inclined or v-shaped ribs mounted on one wall," *J. Fluid Mech.*, vol. 932, A48, 2022.

[54] S. Mahmoodi-Jezeh and B.-C. Wang, "Direct numerical simulation of turbulent heat transfer in a square duct with transverse ribs mounted on one wall," *Int. J. Heat Fluid Flow*, vol. 89, p. 108782, 2021.

[55] W. K. George, H. Abrahamsson, J. Eriksson, R. Karlsson, L. Lofdahl, and M. Wosnik, "A similarity theory for the turbulent plane wall jet without external stream," *J. Fluid Mech.*, vol. 425, pp. 367–411, 2000.

[56] S. Subramaniam and S. Pope, "A mixing model for turbulent reactive flows based on euclidean minimum spanning trees," *Comput. Fluids*, vol. 115, no. 4, pp. 487–514, 1998.

[57] D. Thomson, "A stochastic model for the motion of particle pairs in isotropic high-Reynolds-number turbulence, and its application to the problem of concentration variance," *J. Fluid Mech.*, vol. 210, pp. 113–153, 1990.

[58] R. J. Adrian, "Hairpin vortex organization in wall turbulence," *Phys. Fluids*, vol. 19, no. 4, p. 041301, 2007.

[59] M. Cassiani, P. Franzese, and U. Giostra, "A PDF micromixing model of dispersion for atmospheric flow. part i: development of the model, application to homogeneous turbulence and to neutral boundary layer," *Atmos. Environ.*, vol. 39, no. 8, pp. 1457–1469, 2005.

[60] M. Cassiani, P. Franzese, and J. D. Albertson, "A coupled Eulerian and Lagrangian mixing model for intermittent concentration time series," *Phys. Fluids*, vol. 21, no. 8, p. 085105, 2009.

[61] S. R. Hanna, "Lagrangian and Eulerian time-scale relations in the daytime boundary layer," *J. Appl. Meteorol.*, vol. 20, no. 3, pp. 242–249, 1981.

[62] D. Moreira and M. Vilhena, *Air pollution and turbulence: modeling and applications*. CRC Press, 2009.

[63] A. E. Perry, W. H. Schofield, and P. N. Joubert, "Rough wall turbulent boundary layers," *J. Fluid Mech.*, vol. 37, no. 2, pp. 383–413, 1969.

[64] P. R. Bandyopadhyay, "Rough-wall turbulent boundary layers in the transition regime," *J. Fluid Mech.*, vol. 180, pp. 231–266, 1987.

[65] P.-Å. Krogstad and R. Antonia, "Structure of turbulent boundary layers on smooth and rough walls," *J. Fluid Mech.*, vol. 277, pp. 1–21, 1994.

[66] L. Djenidi, R. Elavarasan, and R. Antonia, "The turbulent boundary layer over transverse square cavities," *J. Fluid Mech.*, vol. 395, pp. 271–294, 1999.

[67] S. Leonardi, P. Orlandi, R. Smalley, L. Djenidi, and R. Antonia, "Direct numerical simulations of turbulent channel flow with transverse square bars on one wall," *J. Fluid Mech.*, vol. 491, pp. 229–238, 2003.

[68] R. Rossi, D. Philips, and G. Iaccarino, "A numerical study of scalar dispersion downstream of a wall-mounted cube using direct simulations and algebraic flux models," *Int. J. Heat Fluid Flow*, vol. 31, no. 5, pp. 805–819, 2010.

[69] C. Rhie and W. L. Chow, "Numerical study of the turbulent flow past an airfoil with trailing edge separation," *AIAA J.*, vol. 21, no. 11, pp. 1525–1532, 1983.